

Aging of Lithium-Ion Batteries under Complex Thermal Conditions

Zur Erlangung des akademischen Grades einer
DOKTORIN DER INGENIEURWISSENSCHAFTEN

von der KIT-Fakultät für Chemieingenieurwesen und Verfahrenstechnik des
Karlsruher Instituts für Technologie (KIT)
genehmigte

DISSERTATION

von

M.Sc. Lisa Cloos

Tag der mündlichen Prüfung: 09.10.2025

Erstgutachter: Prof. Dr.-Ing. Thomas Wetzel

Zweitgutachter: Prof. Gregory Offer



This document is licensed under a Creative Commons
Attribution 4.0 International License (CC BY 4.0):
<https://creativecommons.org/licenses/by/4.0/deed.en>

Kurzfassung

Lithium-Ionen Batterien sind der Maßstab für die Batterietechnologie in mobilen Endgeräten und Elektrofahrzeugen. Essentiell für die Zufriedenheit der Nutzer von Elektrofahrzeugen ist die Erhaltung von Energie und Performanz der Batterie. Diese globalen Zustandsgrößen können durch Alterungsmechanismen, die während der Nutzung auftreten, negativ beeinflusst werden. Die Größe des Einflusses hängt dabei von vielen Faktoren ab. Einer dieser so genannten Stress-Faktoren ist die Temperatur. Außerhalb des optimalen Temperaturbereiches von circa 25 °C altern Lithium-Ionen-Batterien schneller. Bei inhomogenen oder transienten Temperaturfeldern in der Lithium-Ionen Batterie konnten verschiedene Auswirkungen auf das globale Alterungsverhalten simuliert und gemessen werden. Da inhomogene und transiente Temperaturverteilungen in der realen Anwendung durchaus vorkommen können, sind weitere experimentelle und simulative Analysen notwendig. Diese können das Verständnis der relevanten Mechanismen unter diesen Temperaturbedingungen erhöhen.

Um den Einfluss der komplexen Temperaturfelder während der zyklischen Alterung experimentell zu untersuchen, wurden in dieser Arbeit präzise Temperaturrandbedingungen mittels Temperierplatten auf Zellen aufgebracht. Der Effekt auf das Alterungsverhalten wurde mit Referenzbedingungen bei einer zeitlich und örtlich gemittelten Alterungstemperatur verglichen. Ein Temperaturgradient zwischen 10 °C und 40 °C verursachte eine Beschleunigung des Kapazitätsverlusts von $25 \pm 4 \%$ im Vergleich zu der Referenzbedingung einer homogen stationären Alterungstemperatur von 25 °C bei der untersuchten 20 Ah Pouch Zelle. Im Vergleich zu der Beschleunigung des Kapazitätsverlustes von $153 \pm 8 \%$ bei einer Erhöhung einer homogenen stationären Alterungstemperatur von 25 °C auf 40 °C ist diese Beschleunigung durch den Gradienten von 10 °C zu 40 °C gering.

Die globale Alterungsbeschleunigung durch Temperaturgradienten konnte auf lokale Alterungserscheinungen bei der entsprechenden Alterungstemperatur in der Post-mortem Analyse zurückgeführt werden. Eine lokal erhöhte Alterungstemperatur führte zu einem verstärkten SEI Wachstum für die untersuchte Zelle. Um die lokalen Zustandsvariablen der Batterie und deren Beziehungen zum Alterungsverhalten vorherzusagen, wurde die Modellierung als leistungsfähiges Instrument eingesetzt. Das neu entwickelte und validierte physikalisch basierte Alterungsmodell konnte bestätigen, dass sich der globale Kapazitätsverlust aus der Summe der lokalen Kapazitätsverluste zusammensetzt. Dennoch wurden zusätzliche Alterungsmechanismen wie Schichtbildung auf der negativen Elektrode in der Post-Mortem Analyse festgestellt. Diese zusätzlichen Alterungsmechanismen, insbesondere bei orthogonal zu den Elektrodenschichten gerichteten thermischen Gradienten im Vergleich zu Gradienten in Richtung der Elektrodenschichten, wurden in Zusammenhang mit einer erhöhten Beschleunigung des Kapazitätsverlusts bei Temperaturen von 30 °C und 50 °C gestellt. Bei großformatigen Zellen könnten weitere Inhomogenitäten in der Zelle wie zum Beispiel eine inhomogene Leitsalzverteilung mit den Temperaturgradienten wechselwirken. Inhomogenitäten spielen möglicherweise auch bei kleineren Formaten eine Rolle.

Experimentelle Studien an verschiedenen Zellen haben gezeigt, dass Temperaturwechsel deutlich schädlicher für das Alterungsverhalten sein können als Temperaturgradienten. Bestimmte Kombinationen aus Temperaturwechseln haben zu einem starken Kapazitätsverlust unabhängig des untersuchten Zelltyps geführt. Fortlaufende Wechsel zu höheren Temperaturen können die Reaktion von abgeschiedenem Lithium oder lithium-reicher SEI mit dem Elektrolyten beschleunigen. Abhängig von der untersuchten Zellgeometrie können Temperaturwechsel auch Schichtbildung auf der negativen Elektrode verursachen. Ein Zusammenhang mit inhomogenen Temperaturfeldern während des Temperaturwechsels im Ladevorgang wurde postuliert. Entscheidend scheint dabei die zeitliche Änderung der Temperaturfelder zu sein. Die Zellgeometrie und mechanische Effekte könnten für siliziumhaltige

Zellen stärker in den Fokus rücken. Erste Ergebnisse zeigten einen Zusammenhang zwischen mechanischen Alterungseffekten und Alterungseffekten durch Temperaturwechsel.

Zusätzlich zu diesen Zusammenhängen wurde das Zusammenspiel aus verschiedenen Stress-Faktoren mit dem Stress-Faktor der Temperatur als kritisch identifiziert. Eine Reduktion der Entladetiefe von 100 % auf 70 % führte zu einer starken Beschleunigung des Kapazitätsverlustes für einen Temperaturgradienten zwischen 10 °C und 40 °C im Vergleich zur Referenz. Das Alterungsmodell prognostizierte in einer vorläufigen Studie das Auftreten von Lithium Abscheidung in der Region der niedrigeren Alterungstemperatur. Ein direkter Zusammenhang mit unterschiedlichem Stromverteilungsverhalten für unterschiedliche Entladetiefen wurde vorhergesagt.

Diese Arbeit ermöglicht einen wertvollen Einblick in das Alterungsverhalten von kommerziellen Lithium-Ionen Zellen unter komplexen thermischen Randbedingungen und ergänzt die wenigen bisherigen Untersuchungen in der Literatur. Durch das Zusammenspiel aus experimentellen und simulativen Ansätzen konnten kritische Mechanismen, die auch relevant für zukünftige Untersuchungen sind, identifiziert werden.

Diese Arbeit wurde als Monographie verfasst und enthält folgende Publikationen. Teile der Publikationen wurden in dieser Arbeit zitiert. Direkte Zitationen wurden durch eine Einrückung und kursive Schrift hervorgehoben.

- i. Cloos, L.; Wetzel, T. In-Plane versus through-Plane Thermal Gradients during Cyclic Aging of Lithium-Ion Batteries – An Experimental Study. *Energy Technology* **2025**, 2402409.[1]
- ii. Cloos, L.; Langer, J.; Schiffler, M.; Weber, A.; Wetzel, Th. Challenges of Predicting Temperature Dependent Capacity Loss Using the Example of NMC-LMO Lithium-Ion Battery Cells. *J. Electrochem. Soc.* **2024**, 171 (4), 040538.[2]
- iii. Cloos, L.; Queisser, O.; Chahbaz, A.; Paarmann, S.; Sauer, D. U.; Wetzel, T. Thermal Transients to Accelerate Cyclic Aging of Lithium-Ion Batteries. *Batteries & Supercaps* **2024**, 7 (3), e202300445.[3]

Abstract

Lithium-ion batteries are a benchmark battery technology applied in mobile electronics and electric vehicles. Integral to the consumer acceptance of electric vehicles is a high energy and performance retention. These global states can be negatively impacted by aging mechanisms occurring during application. The magnitude of the impact depends on multiple factors. One of the so-called stress factors is temperature. Outside the optimal temperature range of around 25 °C, lithium-ion batteries age faster. When the temperature field inside a lithium-ion battery is inhomogeneous or transient during the cycling, different impacts on the global aging behavior were measured and simulated. Since inhomogeneous and transient temperature profiles may well occur in real life applications, further experimental and simulative analyses were crucial to increase the understanding of relevant mechanisms.

To experimentally investigate the influence of complex temperature fields during cyclic aging in this work, precise temperature boundary conditions were applied to lithium-ion cells with thermal plates. The effect of complex temperature boundary conditions on the aging behavior was compared to a reference condition at a temporal and spatial average aging temperature. A thermal gradient from 10 °C to 40 °C caused a capacity loss acceleration of $25 \pm 4 \%$ compared to the reference condition at a homogeneous steady-state aging temperature of 25 °C on a 20 Ah pouch cell. In comparison to a capacity loss acceleration of $153 \pm 8 \%$ for increasing a homogeneous steady-state aging temperature from 25 °C to 40 °C for the investigated cell, this acceleration caused by the thermal gradient from 10 °C to 40 °C was low.

The global aging acceleration due to thermal gradients could be related to local aging phenomena according to the local aging phenomena in post-

mortem analysis. A locally increased aging temperature increased the SEI growth for the investigated cell. Modeling was used as a powerful tool to predict the in-situ local battery states and their relation to the aging behavior. A newly developed and validated physics-informed aging model confirmed that the global capacity loss can be modeled as the sum of the local capacity losses. Still, additional aging mechanisms such as cover layer formation on the negative electrode were observed in post-mortem analysis. These additional aging mechanisms especially for through-plane thermal gradients were suggested to have caused a larger capacity loss at higher average temperature from 30 °C to 50 °C than the in-plane thermal gradient. For larger format cells, additional inhomogeneities such as a salt inhomogeneity were proposed to superimpose with thermal gradients. However, inhomogeneities could also be relevant for smaller size cells.

Experimental studies on multiple different cells have proven that thermal transients can be more harmful to the aging behavior than thermal gradients. Certain combinations of temperature changes caused a large capacity fade independent of the investigated cell. Ongoing changes to higher aging temperatures during cycling were predicted to accelerate the reaction of lithium rich cover layer with electrolyte. Depending on the investigated cell geometry, thermal transients have also caused cover layer formation on the negative electrode. These were suggested to originate from inhomogeneous temperature fields during the temperature change during charging. Thereby, the temporal change of the inhomogeneous temperature field seemed decisive. The cell geometry and mechanical effects could become increasingly important for silicon containing cells. Preliminary results showed a connection of mechanical aging phenomena and those arising from thermal transients.

On top of these relations, the interaction of the stress-factor temperature with other stress factors was identified to be critical. A reduction of depth of discharge from 100 % to 70 % caused a larger capacity loss acceleration for the in-plane thermal gradient from 10 °C to 40 °C in comparison to the

reference. The aging model predicted lithium plating in the region of lower aging temperature due to different current swapping behavior for different depth of discharges.

This work adds valuable new insights into the aging behavior of lithium-ion commercial cells under complex thermal boundary conditions to the so far limited investigations in literature. This skilfull interplay of the experimental and modeling approach identified critical mechanisms relevant for future research.

The work was written monographically and contains the following publications. Sections of the publications were cited in this work. Direct citations were highlighted with indentation and italic font.

- i. Cloos, L.; Wetzel, T. In-Plane versus through-Plane Thermal Gradients during Cyclic Aging of Lithium-Ion Batteries – An Experimental Study. *Energy Technology* **2025**, 2402409.[1]
- ii. Cloos, L.; Langer, J.; Schiffler, M.; Weber, A.; Wetzel, Th. Challenges of Predicting Temperature Dependent Capacity Loss Using the Example of NMC-LMO Lithium-Ion Battery Cells. *J. Electrochem. Soc.* **2024**, 171 (4), 040538.[2]
- iii. Cloos, L.; Queisser, O.; Chahbaz, A.; Paarmann, S.; Sauer, D. U.; Wetzel, T. Thermal Transients to Accelerate Cyclic Aging of Lithium-Ion Batteries. *Batteries & Supercaps* **2024**, 7 (3), e202300445.[3]

Table of Content

Kurzfassung	i
Abstract.....	v
Table of Content.....	ix
Symbols.....	xi
Acknowledgement	xvii
1 Introduction.....	1
2 State of the Art – Cyclic Aging of Lithium-Ion Batteries	5
2.1 Lithium-Ion Batteries	5
2.2 Aging Mechanisms and Degradation Modes	6
2.2.1 Aging Mechanisms.....	7
2.2.2 Analysis Techniques.....	12
2.3 Aging Stress Factors	17
2.3.1 Cell Design	17
2.3.2 Charge Throughput.....	20
2.3.3 Temperature Level	22
2.3.4 Inhomogeneous Temperature.....	23
2.3.5 Temperature Changes	26
2.4 Interim Conclusion.....	27
3 Methods – Locally Resolved Aging Experiments and Model.....	31
3.1 Electrochemical and Aging Experiments.....	32
3.1.1 Experimental Setups.....	34
3.1.2 Non-Invasive Aging Analysis	43
3.1.3 Post-Mortem Analysis	44
3.2 Segmented Thermal and Electrical Aging Model.....	46
3.2.1 Electrical Network Model	49

3.2.2	Thermal Model	56
3.2.3	Aging of Thermal and Electrical Properties	59
3.2.4	Semi-Empirical Aging Model.....	62
3.2.5	Validation	79
4	Discussion – Local and Global Aging Behavior	83
4.1	Experiments on In-Plane Versus Through-Plane Inhomogeneous Steady-State Temperature Effects.....	83
4.2	Model Supported Insights into Inhomogeneous Steady- State Aging.....	99
4.3	Effects of Homogeneous Transient Temperatures.....	107
4.4	Severity of Inhomogeneous Steady-State versus Homogeneous Transient Temperatures.....	113
5	Conclusion	123
	References	129
	Appendix	clxvii
	Cyclic Aging Studies	clxvii
	Semi-Empirical Aging Model Parameters	clxxi
	Preliminary Validation of Thermal-Electrical Model.....	clxxii
	List of Figures.....	clxxv
	List of Tables	clxxxvii

Symbols

Symbols

A, B, C, D, E, F	-	Coefficients
C	F	Capacitor
c_p	$\text{J kg}^{-1} \text{K}^{-1}$	Specific heat capacity
E_A	J mol^{-1}	Activation energy
f	Hz	Frequency
I	A	Current
k_B	$\text{m}^2 \text{kg s}^{-2} \text{K}^{-1}$	Boltzmann constant
L_{SEI}	-	Theoretical SEI thickness
L	F	Inductance
Q	Ah	Charge throughput
\dot{Q}	W	Heat source
R	Ω	Resistance
r	-	Slope
t	s	Time
T	K	Temperature
T_{EAT}	$^{\circ}\text{C}$	Equivalent aging temperature
U	V	Voltage
α, β	-	Alignment factors OCV
α_{pow}	-	Exponent
η	Ω	Overpotential
ϑ	$^{\circ}\text{C}$	Temperature
λ	$\text{W m}^{-1} \text{K}^{-1}$	Thermal conductivity
ρ	kg m^{-3}	Density
ϕ	V	Potential
τ	s	Time constant

Indices

a, b, c	Elemental compositions
act	Actual
ch	Charge
contact	Contact
dch	Discharge
Diff	Diffusion
error	Error
exp.	Experimental
i	Segment
I, II	First, second,
irr	Irreversible
k	Timestep
lin	Linear
lit	Lithiated
max	Maximum
mean	Average
mig	Migration
min	Minimum
pow	Power
R18	Resistance evaluated at 18 s of pulse
rev	Reversible
sim.	Simulated
src	Source
tot	Total
x	Orthogonal to the tabs
y	In direction of the tabs
z	Perpendicular to the electrode sheets
Ω	Ohm

Abbreviations

A	Acceleration
BoL	Begin of life
C	Carbon
CC	Constant current
CCCV	Constant current, constant voltage
CDA	Capacity difference analysis
CEI	Cathodic electrolyte interface
Char	Characterization
CI	Confidence interval
CPE	Constant phase element
C-rate	Current rate
CT	Charge transfer
CV	Constant voltage
d	Days
Diff	Diffusion
DMC	Dimethyl carbonate
DoD	Depth of discharge
DVA	Differential voltage analysis
EC	Ethylene carbonate
ECM	Equivalent circuit model
ECN	Equivalent circuit network
EDX	Energy-dispersive x-ray spectroscopy
EFC	Equivalent full cycle
EIS	Electrochemical impedance spectroscopy
FLW	Finite length warburg element
freq	Frequency
GITT	Galvanostatic intermittent titration technique
ICA	Incremental capacity analysis
ICP-OES	Inductively coupled plasma optical emission spectroscopy

	copy
Im	Imaginary
I_y	Inhomogeneous steady-state in-plane
I_z	Inhomogeneous steady-state through-plane
LAM	Loss of active material
LCO	Lithium cobalt oxide
Li	Lithium
LIB	Lithium-ion battery
LiPF_6	Lithium hexafluorophosphate
LLI	Loss of lithium inventory
NCA	Nickel cobalt aluminum oxide
NE	Negative electrode
NMC	Nickel manganese cobalt oxide
NMP	N-methyl pyrrolidone
Ntab	Negative electrode tab
OCV	Open circuit potential
PE	Positive electrode
PMA	Post-mortem analysis
POM	Polyoxymethylene
Ptab	Positive electrode tab
qOCV	Quasi open circuit voltage
R^2	Coefficient of determination
RC	Resistor and Capacitor
Re	Real
resnorm	Squared norm of residuals
RQ	Constant phase element
RTP/RPT	Reference performance test / Reference Parameters Test
s	seconds
SEI	Solid electrolyte interface
SEM	Scanning electron microscopy

SoC	State of charge
SoH	State of health
T	Homogeneous transient
XRD	X-ray diffraction

Acknowledgement

The work for this thesis has been carried out during my time as research associate at the Institute of Thermal Process Engineering (TVT) at the Karlsruhe Institute of Technology (KIT) from May 2020 until April 2025. I would like to thank my supervisor Prof. Dr.-Ing. Wetzel for his trust, guidance and support of the work. I thank Prof. Gregory Offer for contributing his view on this thesis.

Thanks goes to my predecessors Dr.-Ing. Sabine Paarmann, Oliver Queisser and Daniel Werner. Without their groundwork and support, the scope of this thesis would not have been possible. I thank my discussion partners with regards to aging phenomena – Sabine Paarmann, Philipp Dechent, Daniel Werner, Markus Schreiber, Marcel Rogge, Lukas Köbbing, Meinert Lewerenz and Ahmed Chahbaz – as well as other battery topics – Oliver Queisser, Marc Schiffler, Dr.-Ing. André Weber, Raphael Schoof and Julia Gandert.

Furthermore, I thank Prof. Gregory Offer at Imperial College London for the invitation for a research visit. His input greatly advanced the work on semi-empirical aging modeling. Thanks to the group members of ESE at Imperial College London for the great time. Many thanks also to Dr. Dhammika Widanalage at Warwick University for the collaboration on measurement of entropy coefficients.

I gratefully acknowledge the funding and support by the German Research Foundation (DFG) within the research training group SiMET (Simulation mechanisch-elektrischer-thermischer Vorgänge in Lithium-Ionen Batterien, 281041241/GRK2218) and the Federal Ministry of Education and Research (BMBF 03XP0320D).

I really enjoyed being part of the research training group SiMET and the project BALd (Beschleunigte Alterungstests und Lebensdauerprognosen). I am thankful for the fun time at the TVT with my current and former colleagues as well as my colleagues from the Thin Film Technology (TFT).

I would like to thank the many helping hands at the TVT and also other institutes. I thank Sabrina Herberger at TVT at KIT for support in test setup, cell disassembly and thermal material property measurements. Thanks go to Leonie Pfeifer at TVT at KIT as well as Marc Schiffler at IAM-ET at KIT for support in cell disassembly. Furthermore, I thank Annette Schucker at IAM-ET at KIT for conducting Energy-Dispersive X-ray spectroscopy (EDX) and X-ray diffraction (XRD) measurements, Elisabeth Eiche at AGW at KIT for conducting Inductively Coupled Plasma Optical Emission Spectroscopy (ICP-OES) measurements and Volker Zibat at LEM at KIT for conducting Scanning Electron Microscopy (SEM) and EDX measurements. Thanks go to Jonas Bender at TVT for his support in uncertainty calculations. I thank the TVT-workshop-team Max Renaud, Stefan Böttle, Stephan Fink and Michael Wachter for manufacturing parts of the experimental setup. I also thank Nicole Feger who always makes sure that the background work runs smoothly, Dr.-Ing. Philipp Seegert for the team lead and Dr.-Ing. Benjamin Dietrich for the administrative support.

I thank all students who I have supervised during my time at the institute for their great work supporting the research topic. Thanks goes to Tobias Biegi, Jakob Reichert, Simon Pelzer, Sarah Bischof, Nikolai Erhardt, Felix Pitzal, Jan-Nikas Gerdes, Sebastian Schorstädt, Julian Schnitzius, Donghee Son, Frederik Heberle and Jennifer Langer for their work. The resulting bachelor and master thesis are listed:

- "Entwicklung funktionaler Zusammenhänge für Alterungsfaktoren von Li-Ionen Batteriezellen" (12/2022)
- "Weiterentwicklung eines Fittingtools für Elektrochemische Impedanzspektren zur automatisierten Analyse während der Alterung von Li-Ionen Batteriezellen" (10/2022)

- „Parametrierung und Validierung eines elektrischen Simulationsmodells für Lithium-Ionen Batterien“ (10/2022)
- „Validierung thermisch-elektrischer Simulationsmodelle für Li-Ionen Batteriezellen“ (06/2022)
- „Inbetriebnahme eines Versuchsstandes zur Untersuchung des thermisch induzierten Alterungsverhaltens großformatiger Li-Ionen Batteriezellen“ (03/2022)
- „Kopplung und Optimierung von Modellen zur thermisch-elektrischen Simulation des Alterungsverhaltens“ (08/2021)
- „Weiterentwicklung eines 3D-Batteriemodells zur Simulation des thermisch induzierten Alterungsverhaltens“ (05/2021)
- „Entwicklung und Validierung eines elektrischen Modells zur elektrisch-thermischen Simulation von Li-Ionen Batteriezellen“, (12/2020)

Last but not least I am very thankful for the support of my family and friends.

Karlsruhe, April 2025

Lisa Cloos

1 Introduction

The climate action plan of the German government “Klimaschutzplan 2050” determines the goal of mostly greenhouse gas neutrality in the mobility sector by 2050[4]. Many possible technologies have been presented to achieve this goal. Lithium-ion battery (LIB) technology is one technology in which the German government invests. LIBs are already widely applied in portable devices and in the automotive sector[5]. Due to the high specific energy, long cycle and calendar life and high safety of LIB, they are the benchmark for emerging new battery technologies[6]. However, many critical requirements to gain social acceptance of the battery technology are not met[7]. People are especially concerned by the driving range, cost and charging infrastructure[7]. The driving range can be compromised by ongoing aging of LIB[8]. Therefore, the mechanisms leading to aging need to be understood to elongate and predict the lifetime[9]. A correct estimation is essential for the manufacturer to ensure the car warranty lifetime of 8 to 10 years and 160 to 250 thousand kilometers[10]. The difficulty lies in the varying operating conditions which strongly affect the state of health (SoH)[9].

One of these influential operating conditions is the ambient temperature. It is common knowledge that both lower and higher temperature than the optimum aging temperature around 25 °C accelerate cyclic aging[11]. However, the extent varies depending on the current[12–14], electrode thickness or energy density[12–14], and the cell chemistry[15]. Therefore, the dependency needs to be evaluated for each cell[14,16,17]. Furthermore, the temperature field inside a battery cell is rarely homogeneous[18,19] and steady-state[20,21] during application. Especially in extreme conditions, large thermal gradients can arise. For example, in-plane (in direction of the electrodes) and through-plane (perpendicular to the electrodes) thermal gradients can be around 18-20 K[18]. The temperature field

is affected by heat generation and heat flux[22] and the thermal boundary condition[23,24]. The temperature inhomogeneity during cycling is suspected to be more critical in larger cells[25].

Already at Begin of Life (BoL), those complex thermal boundary conditions affect the global battery behavior. Temperature changes during cycling cause changes in the voltage response[26] and an inhomogeneous temperature distribution has shown to change the resistive behavior[27–29]. Locally, the strong effect of temperature on current was found to follow an Arrhenius relation[30]. On the example of discharging direction, the impact of increasing resistance[31] due to decreasing SoC[32] in combination with the open circuit potential (OCV)[33] counteracts this effect and leads to current swapping which is a known phenomenon in parallel connected cells[31,32,34,35]. Current swapping and locally different voltages were already confirmed in a single cell with multitab approach[36–39]. However, the effect of aging on that interplay was predicted to either be mitigating or aggravating[40–43].

Generally, few experimental investigations have focused on aging with precise thermal transients or thermal gradients in comparison to a reference case. Temperature changes have shown to accelerate the aging behavior[26,44] but the reason is not entirely clear. Increased lithium plating has been found in post-mortem analysis[26,45]. On top, a change from lower to higher temperature can cause a reaction of lithium rich solid electrolyte interface (SEI) with electrolyte which leads to gassing and cell failure[46]. For in-plane thermal gradients on the other hand, no drastic aging acceleration has been found in comparison to a cell aged at the equivalent average homogeneous temperature[44]. Still, locally different aging mechanisms were found in post-mortem analysis[17,47]. Contrarily, through-plane thermal gradients caused a strong aging acceleration[23,48]. The directionality of the thermal gradient depending on the position of positive and negative electrode also influenced local aging mechanisms[48]. Simulative investigations on these thermal gradients have found strong acceleration

due to a positive feedback mechanism of temperature, current, resistance and aging[42], but also mitigating effects[40,41].

Still, all of the discussed thermal boundary conditions are very relevant in application. For example, in automotive application, a thermal management system is applied to keep the cells in an optimal operating window. More effective cooling strategies for reducing the average temperature such as surface cooling cause even higher temperature differences inside the battery. Also, fast preheating might be applied to increase the fast charging capability of battery packs. [49]

All in all, few studies on the effect of thermal transients and gradients on cyclic aging showed partly consistent and partly contradictory results that give rise to the following research questions addressed in this work:

- I. Storch et al.[47] suggested a suppression of gradients to be critical for a long lifetime of large format LIB. In their study, they found local lithium plating caused by a relation of temperature, current density and lithium concentration gradient.
Can this conclusion be confirmed and substantiated?
- II. Are through-plane thermal gradients worse than in-plane thermal gradients?
- III. Why do thermal transients increase capacity loss during cyclic aging?

So far, experimental investigations are limited when it comes to cyclic aging with superimposed complex thermal boundary conditions. Hence, model assumptions cannot be responsibly made. It is not yet clear what the underlying mechanisms are and how they are transferable to different cells. Therefore, additional cyclic aging studies with precise thermal boundary conditions are imperative. The experimental studies in this work include the previously identified critical thermal boundary conditions – homogeneous transient (T), inhomogeneous steady-state through-plane (I_z) and inhomogeneous steady-state in-plane (I_y) applied to different cells.

To understand these experimental findings, a simulative investigation is used to predict the local aging states in the cell. The interaction of the temperature, current and aging distribution in the cell was previously identified to be detrimental to the global aging behavior with inhomogeneous temperature distribution. Therefore, a semi-empirical aging model will be included in a thermal-electrical network model.

With a multi-level and multi-method approach, this work aims to increase the understanding of the aging mechanisms arising from complex thermal boundary conditions. In a first step, however, relevant existing knowledge on aging needs to be revisited and put in relation to the aims of the present work. In a second step, other stress factors causing inhomogeneities are discussed. In a third step, the focus is put on the impact of temperature on aging and previous findings on the impact of inhomogeneous steady-state and homogeneous transient thermal boundary conditions. These steps are performed on the basis of a literature review in the following chapter.

2 State of the Art – Cyclic Aging of Lithium-Ion Batteries

Aging of LIB is noticeable to the user in two ways. Firstly, it shows in form of less utilizable energy storage from capacity loss and/or lowered voltage due to resistance increase. Secondly, resistance growth causes a power capability loss. Aging itself occurs both during storage and during use. The first is called calendar aging and the latter cyclic aging. Simplified, thermodynamic instabilities of the materials in LIB cause calendar aging and kinetic effects additionally occur during cyclic aging. Even though, calendar and cyclic aging are mostly treated as a superposition, interactions exist. [50]

2.1 Lithium-Ion Batteries

Aging concerns different parts of LIB. They consist of a positive and a negative **electrode**. Conventionally, the negative electrode (NE) can be referred to as anode and the positive electrode (PE) as cathode. Lithium ions can deintercalate from one electrode, migrate through an electrolyte with dissociated lithium salt and a porous separator and intercalate into the other electrode. The electrons move from current collector to current collector which are electrically connected. Intercalation and deintercalation only takes place in case of standard negative and positive electrode chemistries. The positive electrodes usually consist of lithium transition metal compounds on an aluminum current collector. These lithium transition metal compounds are categorized in layered oxides, spinels and phosphates. The negative electrode is commonly graphite. Silicon can be added to increase the specific capacity. [51]

To ensure functionality, also **inactive materials** are needed. For instance, the electrode material is coated onto the current collector with binder which is traditionally a blend of polyvinylidene difluoride, carbon black and solvent. The latter is removed in the drying process. The binder optimizes cohesion and adhesion, and the carbon black the electrical conduction. For the ion conduction, lithium salt (commonly hexafluorophosphate LiPF_6) is in solution with organic solvents to form the electrolyte. These can be ethylene carbonate (EC), dimethyl carbonate (DMC), ethyl carbonate and diethyl carbonates. Manufacturers also add further additives to increase longevity and security. The electrolyte as well as lithiated graphite is vulnerable to water. Therefore, hermetic casings mainly containing lightweight aluminum are used. Common formats are pouch, cylindrical and prismatic. While cylindrical and prismatic cells have a rigid casing, the pouch foil consists of thin aluminum foil with polymer coating. [51]

2.2 Aging Mechanisms and Degradation Modes

Simply speaking, different changes of these active and inactive LIB materials over time lead to aging. Stress-factors, such as ambient conditions and current load, affect the aging. Relations between the causes and the effects of aging which are capacity loss and power capability loss can be drawn. [52]

In other words, stress-factors accelerate aging mechanisms on particle and electrode level which cause the capacity loss and resistance increase as shown in Figure 2.1. There are also analysis methods on cell level which can give an estimate of the occurring degradation. For example, the aging mechanisms influence the OCV on cell level. This can be exploited for analysis. However, different aging mechanisms may cause the same changes in the OCV. These changes of the OCV are categorized in degradation modes. Each degradation mode can represent multiple aging mechanisms. [52]

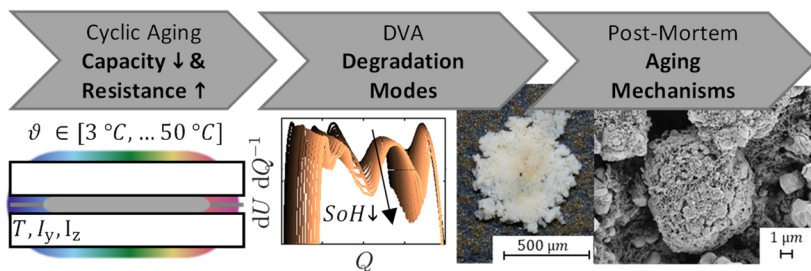


Figure 2.1: Impact of cyclic aging on different levels – Capacity loss and resistance increase, degradation modes and aging mechanisms. (Adapted with permission under the terms of Creative Commons Attribution 4.0 License CC BY.[2] Copyright 2024, The Authors. Published on behalf of The Electrochemical Society by IOP Publishing Limited.).

2.2.1 Aging Mechanisms

Aging mechanisms can be categorized in three groups. Electrochemical processes mostly couple negative and positive reactions and are enhanced at higher and lower voltages. Chemical processes are reactions between different components such as oxidation. Mechanical processes can be induced from the outside or result from volume changes of the crystals upon cycling. [53]

Apart from positive and negative electrode particles, inactive species such as binder and conductive particles can also decompose, oxidise or loose contact[54]. The aging mechanisms of layered and spinel oxide **positive electrodes** can be summarized in three interacting principles. These are structural disordering and transitions, chemical decomposition and dissolution, and surface film modification as summarized by Birkel et al.[52] in Figure 2.2. [54,55]

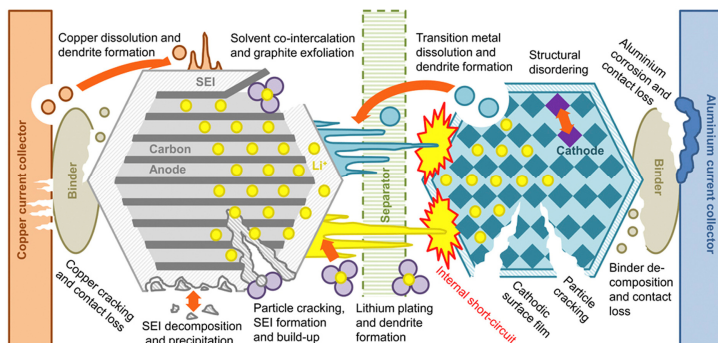


Figure 2.2: Aging mechanisms of positive and negative electrode as well as inactive materials in LIB (Reproduced with permission under the terms of Creative Commons Attribution 4.0 License CC BY.[52] Copyright 2016, The Authors. Published by Elsevier B.V.).

Structural reconstruction of the positive electrode can appear in the following way. Oxygen from the layered oxide positive electrode active material themselves, here LCO[56,57], can act as a source of oxygen for changes of a sub-surface layer resulting in rock-salt structure. This structure drastically increases the positive electrode impedance[58]. Structural reconstruction into rock salt, cubic and spinel phases were also observed for $\text{LiNi}_a\text{Mn}_b\text{Co}_c\text{O}_2$ (NMC)[59,60]. This can be enhanced by cation mixing of Ni^{2+} and Li^{+} ions[61,62], which are similar in ionic radius[63]. In an LiMn_2O_4 (LMO)-NMC blend, the structural changes were mainly observed for the NMC component[64]. The spinel LMO shows structural changes at both low and high SoCs. In the discharged state and elevated temperatures the Jahn-Teller distortion[65,66] and in the charged state the formation of an oxygen-rich spinel phase[67] are known. High SoCs may trigger cation mixing of Li^{+} and Mn^{2+} in LMO[68] and electrolyte oxidation[69,70].

Another mechanism that alters the surface of the positive electrode particles is a surface film[71]. It mainly consists of LiPOF , LiF and polymers or polycarbonates and is called **cathode-electrolyte interface (CEI)**[72]. It does

not passivate completely[72] but can increase the impedance[71]. So far, no detailed understanding of CEI formation exists, consensus only exists in that it is related to decomposition of electrolyte[73].

Higher voltages can enhance positive electrode particle **cracking** and pulverization which accelerates other side reactions such as electrolyte oxidation and transition metal dissolution. Particle cracking can be induced from mechanical tension for example due to lithium intercalation deforming the lattice[51]. Generally, layered positive electrodes have an anisotropic and spinels an isotropic lattice change. Therefore, secondary particles of layered positive electrodes are more prone to cracking[74]. Large lattice alterations during high voltage operation can cause electrochemically induced intragranular cracks[75]. Other authors, however, suggest that particle cracking is more of a symptom of surface reactivity rather than a cause[76].

In comparison to the positive electrode, changes in the bulk of the **negative electrode** particles are only minor. Volume changes of graphite during intercalation are in the order of 10 %[54]. This is different for silicon which is used in modern battery anodes to increase the capacity[77]. Theoretically, the volume expansion of silicon is 320 % at full lithiation and high temperatures[78]. This can cause cracking of silicon particles[79]. When it comes to graphite, exfoliation[80], particle cracking due to solvent co-intercalation[81,82] and gas evolution during SEI formation[83] are more relevant for the capacity fade[54]. A threshold local current density was correlated to graphite exfoliation[80].

Another positive electrode aging mechanism which can be enhanced by cracking is **transition metal dissolution**[84]. Standard LiCoO_2 (LCO), which is one of the earliest applied technologies and consists of a layered oxide structure[51], does not show any dissolution unless in overcharge[85]. Transition metal dissolution is a known phenomenon for LMO which has a spinel structure. LMO becomes unstable upon complete lithium extraction[65]. The manganese can also be dissolved in the presence of HF[86]. The HF is mainly from hydrolysis of the LiPF_6 induced by impurities[54]. Still,

Darma et al.[87] observed better cycling stability of the spinel LMO in comparison to the layered oxide NMC and $\text{LiNi}_{0.8}\text{Co}_{0.15}\text{Al}_{0.05}\text{O}_2$ (NCA) in their blend. Only at 40 °C, the LMO also dissolved manganese species[88]. Multiple studies prove that also NMC, with varying Ni Mn and Co ratios, are prone to transition metal dissolution at higher voltages[84,89,90]. Kasnatscheew et al.[91] compared different NMC compositions. They found that Li^+ extraction ratio is a better measure than the charge cut-off potential. Transition metal dissolution is oftentimes observed because the positive electrode can reach higher voltages during cyclic aging[87,89,92].

Transition metals are also problematic because they can increase **SEI** layer growth on the negative electrode[93]. The transition metals are said to change the SEI[94,95] and increase the charge-transfer impedance[96]. Principally, the SEI exists because standard electrolytes are unstable in the operating voltage of the negative electrode and form low soluble precipitates on the negative electrode[51]. These precipitates originating from reduced salt anions are inorganic compounds such as LiF , LiCl and Li_2O and the reduced solvent causes Li_2CO_3 , semicarbonates and polymers[97]. The SEI formation is accompanied by gaseous electrolyte decomposition products[83]. An effort was made to increase the stability of the SEI while maintaining minimum electronic and maximum Li^+ conductivity[98]. One way is to use film forming electrolyte solvents or additives to suppress side reactions[99].

Different theories exist of the SEI growth. The diffusion of neutral lithium atoms through the SEI is one of them[100]. Even though, the SEI is mainly formed in the first cycles, SEI growth is an ongoing process and leads to capacity loss and electrolyte decomposition throughout the cell life[54]. Electrolyte decomposition influences many properties, for example the NE porosity, lithium-ion concentration, electrolyte potential and electrolyte transport properties[101]. In the worst case, the electrolyte loss can lead to a dry-out[102] which causes inhomogeneous electrode usage[103]. Apart from capacity loss, SEI also increases the impedance and therefore leads to a

power loss[104,105]. Increased temperature negatively impacts the SEI. A SEI forming temperature beyond 45 °C can increase the capacity fade[106]. Furthermore, these higher temperatures may cause repeated film formation leading to both lithium loss and an increase in negative electrode resistance[107]. Another negatively impacting stress-factor on the SEI thickness is a high current rate (C-rate), more so during charging than during discharging[108].

Whereas SEI growth is accelerated at higher temperatures, another aging mechanism namely **lithium plating** occurs mostly at lower temperatures[109], higher SoC[110] and higher C-rates[111]. Thermodynamically, lithium plating occurs at a negative electrode voltage below 0 V[109,112]. However, batteries are rarely in equilibrium. For example, lithium plating does not occur when kinetic limitations such as limited ion transport due to depleted lithium ion concentration exist[110]. Kinetics can also influence the lithium plating morphology. Electrolyte diffusion limitations for lithium metal negative electrodes[113] and solid diffusion limitations for intercalation negative electrodes[114,115] were proposed as a main driver. It was suggested that the local current density changes the lithium growth mode – root-growing whiskers over surface growing clusters to tip-growing dendrites[116].

It is also possible that reversibly plated lithium intercalates during CV-phases[117]. During discharging, lithium can be stripped resulting in a voltage plateau. However, plated lithium can also oxidize and isolate during the stripping process[118]. This oxidation and insulation process was first called “**dead lithium**” by Yoshimatsu et al.[119]. Peled[120] suggested this insulation to be an SEI structure. Later, this structure was found to contain mostly lithium alkyl, lithium carbonate, LiF, LiOH, Li₂O etc.[121].

2.2.2 Analysis Techniques

Different analysis techniques exist to prove the presence of certain aging mechanisms. In **Post-mortem analysis** (PMA) many aging mechanisms can be detected. However, this is an invasive technique because it includes a cell opening. Waldmann et al.[122] provided a comprehensive overview over different PMA techniques. The following references are only exemplary. Microscopy techniques are used very often. Optical microscopy such as light and laser microscopy are low effort, show depositions on the electrode surface and colors in the μm range[2,123,124]. For higher resolution, to observe surface films and cracking, scanning electron microscopy (SEM) is used[45,88]. Both, surface and cross-sections can be analyzed[44,123]. For example the SEI can be seen with SEM as a very thin layer on the negative electrode particles[98]. A supplementary method to determine the chemical composition of the surface is energy-dispersive X-ray spectroscopy (EDX)[125]. However, in conventional EDX, lithium is not detectable[122]. To detect lithium, other chemical analysis methods for the electrode bulk are used. One such method is inductively coupled plasma optical emission spectroscopy (ICP-OES)[2,45,126]. ICP-OES does not measure all elements and is therefore only quantitative of the detectable elements[122]. The analytical method to analyze SEI is X-ray photoelectron spectroscopy (XPS)[56,127]. Another important technique to determine structural changes in the crystalline structure is X-ray diffraction (XRD)[128].

PMA is time and material costly. A common non-invasive analysis tool is the **differential voltage analysis** (DVA) or incremental capacity analysis (ICA) to analyze the degradation modes. Both methods visualize phase transitions of the electrodes in the OCV. Therefore, this method only shows thermodynamic changes[52]. The ICA is the derivation of the charge throughput with respect to voltage and plotted over voltage[129] while DVA is the derivation of the voltage with respect to charge throughput plotted over charge throughput[130] (Figure 2.3).

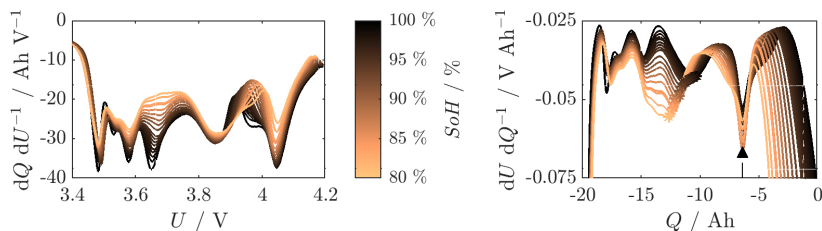


Figure 2.3: Exemplary ICA (left) and DVA (right) of a LIB aged at 45 °C for decreasing SoH (dark to light). (DVA adapted with permission under the terms of Creative Commons Attribution 4.0 License CC BY.[2] Copyright 2024, The Authors. Published on behalf of The Electrochemical Society by IOP Publishing Limited.

In DVA, it possible to attribute individual peaks to phase changes of individual electrodes[130]. Therefore, further focus is placed on the DVA. An exemplary electrode balancing of the negative and positive electrode peaks in DVA is shown in Figure 2.4.

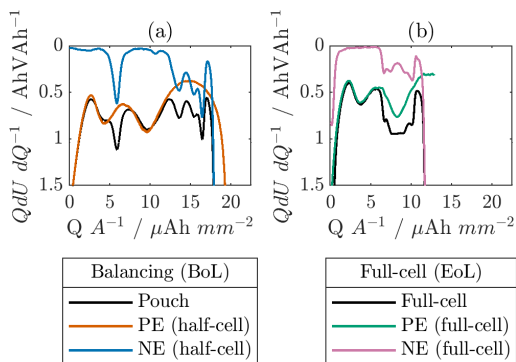


Figure 2.4: DVA of positive (PE) and negative (NE) electrodes matched to pouch cell and full-cell DVA at (a) BoL and (b) EoL (Adapted with permission under the terms of Creative Commons Attribution 4.0 License CC BY.[2] Copyright 2024, The Authors. Published on behalf of The Electrochemical Society by IOP Publishing Limited.)

Many methods for this electrode balancing exist in literature[131]. Aging alters the offset and loading ratio of the negative and positive electrode voltage curves (Figure 2.4 (b)). A shift of the negative and positive electrode voltage curves towards each other is a consequence of a loss of lithium inventory (LLI)[132]. At the same time, the half-cell voltage curves can contract due to the loss of active material (LAM)[133]. In practice, DVA is mostly calculated from a quasi-OCV measurement which is a discharge and charge cycle with low C-rates for example C/25[130]. Therefore, some kinetic impact is measurable. Kinetics will add ohmic and faradic resistances[134]. Another technique to acquire the OCV at certain SoC is the galvanostatic intermittent titration technique (GITT) in which (dis-)charging and relaxation are intermittent[135].

The **degradation modes** LLI and LAM are caused by different aging mechanisms which cannot be differentiated with this analysis technique. LLI is mainly caused from SEI, electrolyte decomposition and lithium plating. LAM can originate from aging of the inactive materials, for example, from corrosion of current collectors and decomposition of the binder. Also, active materials can lose electric contact or crack. Specifically, the positive electrode suffers from structural disordering and transition metal dissolution while the negative electrode can lose active material due to covering with lithium or by graphite exfoliation. [52]

Electrochemical impedance spectroscopy (EIS) can be used to obtain information about the kinetics during aging. EIS measures the impedance by applying an alternating current or voltage and measuring the phase shift. The impedance can be visualized in a Nyquist plot with imaginary (Im) over real (Re) part (Figure 2.5). [136]

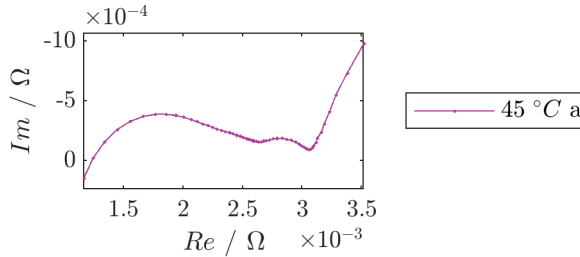


Figure 2.5: Exemplary Nyquist plot of EIS during checkup of aged cell at an aging temperature of 45 °C from “Enertech” aging study by Cloos et al.[2].

Thereby, irreversible electrode processes act as serial resistors and reversible electrode processes as capacitive reactive part of the impedance. Processes such as ion and electron transport as well as charge transfer from the electrolyte through the electric double layer can be detected. [136]

Equivalent circuit models are used to represent impedance spectra. The models consist of different elements. For example, RC elements representing charge transfer (CT) kinetics can be fitted to the measured impedance spectra by optimizing algorithms such as *Levenberg-Marquardt*[136]. In a Nyquist plot, such RC elements visualize as a semi-circle[136]. The simplest model to approximate an impedance spectrum of a battery was proposed to be the Randles[137] equivalent circuit[138]. The Randles equivalent circuit consists of an ohmic resistance, a charge transfer resistance and the diffusional resistance or Warburg impedance[138]. The ohmic resistance is due to ionic conductivity of the electrolyte and electronic conductivity of the electrode material, the carbon black phase and metallic current collectors[139]. Traditionally, the first semi-circle is attributed to surface films on the graphite electrode (SEI) and the second semicircle is attributed to charge transfer. This was first introduced by Aurbach et al.[140] and Levi et al.[141]. The processes at low frequencies are diffusive[142]. This can be both diffusion of the ions in the electrolyte and solid-state diffusion. To model the diffusive part, a combination of Warburg element and capacitance was

proposed by Jacobsen and West[143]. Pre-processing with a capacitance is necessary for impedance spectra of LIB because they do not converge towards the real axis at low frequencies[144]. Also at high frequencies, an inductance can be used to account for the cabling and measurement setup[139]. Instead of RC-elements, RQ-elements can be fitted. These are represented by compressed half-circles in a Nyquist plot[145,146]. Both RQ and Warburg elements are in the frequency domain and can be transformed to the time domain by methods presented by Buller[145] and Handschuh[146] for time domain modeling.

A differentiation of the processes at positive and negative electrode is possible with EIS measurement on half-cells. In such a case, the electrode is assembled against a reference electrode in an experimental cell setup. The frequency dependency of the individual processes can then be analyzed by the **distribution of relaxation times (DRT)**[144]. For an LFP graphite cell, Illig et al.[144] identified the first semi-circle as contact resistance of the positive electrode, the second as SEI diffusion and charge transfer of the negative electrode, the third as charge transfer of the positive electrode and then solid-state diffusion. This assignment differed slightly for an LMO-NMC / graphite cell. Stiaszny et al.[147] identified the charge transfer shares with decreasing frequency to SEI resistance, negative electrode charge transfer resistance and positive electrode charge transfer resistance. More specifically, processes at 0.1 to 9 Hz were related to NMC charge transfer[148]. Interestingly, in a cyclic aging study on the LMO-NMC / graphite cell, the largest increase in impedance was due to the charge transfer resistance of the positive electrode. Furthermore, a large increase of the ohmic resistance resulted from a cover layer on the negative electrode[149]. Another possible phenomenon during aging is the separation of the semi-circles in the Nyquist plot related to increasing time constants of the SEI processes[150].

2.3 Aging Stress Factors

A difficulty of the aging and SoH prediction lies in the multitude of interacting stress-factors. Not only temperature[11] and mechanical effects[151] but also many electrical conditions such as the mean state of charge (SoC)[152,153] and depth of discharge (DoD)[154,155] are known to alter the cyclic aging behavior. Also, an increase in current rate (C-rate) is commonly used to accelerate the cyclic aging behavior[156,157]. However, these trends are not necessarily universally true. For example, Barcellona and Piegari[158] found the aging to be independent of the C-rate in their setup with exact temperature control via Peltier-elements. Still, in a ranking of stress-factors by Su et al.[159], the charging current was found to be the most important stress-factor followed by the upper cut-off voltage, temperature, lower cut-off voltage and discharge current. Gewald et al.[160] also considered the DoD and average SoC and found them to have the greatest influence. Furthermore, the presence of a constant voltage (CV) phase was identified to increase aging[161]. Specifically, overcharge is a known safety risk due to increased electrolyte decomposition and lithium plating[162].

2.3.1 Cell Design

The stress-factors have different impact on different cells[160]. LIB do not only differ in cell chemistry but also cell design which can also have an effect on aging mechanisms. On the example of lithium plating, Vetter et al.[54] have summarized that poor electrode balancing, geometric misfits and mixed potential effect enhances lithium plating.

The **balancing** of electrodes is determined by the loading ratio of negative and positive electrode and an off-set[134]. The loading ratio is usually chosen in a way that the negative electrode is not limiting. Negative electrode limitation would mean an excess positive electrode capacity. This excess lithium would then plate during charging[163]. In practice, the loading ratio is around 1.1 to 1.2[164]. The offset is small for graphite

layered oxide cells (2-5 %) because of the SEI growth and the positive electrode capacity loss in the first few cycles[165]. The balancing and the cut-off voltages are also chosen in such a way that the positive electrode is not overcharged[166]. However, during aging, the alignments shift due to LLI. This is also called “anode slippage”[133]. It was shown that this anode slippage can cause increasing positive electrode potential at the end of charging for high Nickel NMCs[89,167]. This accelerates aging due to transition metal dissolution, thickening of CEI and SEI[89].

Another design factor causing lithium plating are geometric misfits. Originally, the inclusion of an **anode overhang** reaching beyond the size of the positive electrode was proposed to reduce lithium plating at the edges of an electrode[168]. However, in commercial LIB with anode overhang, edge plating is a common issue[169,170]. Now, it was shown that the anode overhang should be minimized because the overhang area creates an imbalance in lithium distribution causing lithium plating[169]. The anode overhang has further effects on cycling. It was first noticed by Gyenes et al.[171] that the coulombic efficiency increased after some cycling due to the anode overhang. It serves as a source and sink for lithium ions. The anode overhang does not only increase the coulombic efficiency but can also increase the capacity during calendaric aging[172]. This implies a reversibility of calendar aging[173]. For cyclic aging, it has further consequences. Including a CV-phase during cyclic aging enables lithium transport into the anode overhang. Resting at lower SoC turns the process around. This resulted in large differences in aging behavior and large recoverys after cycling[174]. Therefore, the effect was proposed to be essential in modeling[175].

Not only the anode overhang, also the rest of the graphite negative electrode has shown **inhomogeneous lithium distribution** during cycling. This means that different $\text{Li}_{1-x}\text{C}_6$ phases can coexist at the same time. This inhomogeneity is more severe at higher discharging rates and lower temperatures. During relaxation, this heterogeneity disappears. At room tempera-

ture it can take up to 20 to 40 minutes[176]. Inhomogeneous compression has shown to cause lithium plating[177–179]. Subsequently, pressure gradients can impede a redistribution of lithium heterogeneity[180]. The heterogeneity can be increased by shallow cycling in a SoC range with high volume expansion[181]. Kobayashi et al.[182] explained the effect of shallow cycling on the planar inhomogenization by different conductivities of Li^+ in the electrolyte. To judge the level of inhomogeneity, two methods were presented by Lewerenz et al.[181]. Firstly, a flattening of differential voltage analysis (DVA) curves was observed which relates to unsimultaneous discharging and therefore presence of different lithiation stages[183]. Secondly, an increase in capacity difference analysis (CDA) indicates an inhomogeneity[181]. CDA is the difference between a capacity measured at a lower and a higher C-rate. An increase in capacity difference can also originate from the presence of a covering layer. A cover layer leads to faster discharging of uncovered and slower discharging of the covered parts[184].

Another influencing factor on the **in-plane inhomogeneous lithium distribution** is the tab configuration[185]. A combination of thermal and electrical in-plane inhomogeneity due to one-sided tab location was reported in battery modeling studies[186]. Under some conditions, plating also occurs preferentially close to the tabs due to locally high current densities[187]. To reduce thermal inhomogeneity, optimized tab designs have been proposed especially in fast-charging scenarios. In cylindrical cells, an increase in the number of tabs was suggested[24,188]. For pouch cells, counter-tab configuration result in a more uniform temperature field[189]. Especially long thin tabs were shown to reduce the internal temperature gradient[190].

Apart from a planar inhomogeneity, also **lithium inhomogeneities over the thickness** of the electrode coating exist. The electrodes are charged and discharged layer-by-layer. This means that graphite particles farthest away from the positive electrode have a less defined potential profile similar to inhomogeneities in-plane[191]. This through-plane inhomogeneity also translates to the aging behavior. Lithium preferentially deposits at the

separator negative electrode interface[110,121,192], but can also deposit in the inner pore structure[192]. Close to the separator is the first position where the anode potential falls below 0 V[110].

Another cell design parameter influencing lithium plating is the optimization to **high power** or **high energy** usage. To achieve a higher power density, the electrodes have lower coating weights, lower areal capacities, smaller active particles and higher positive electrode porosities[193]. A lower coating thickness decreases the ion diffusion resistance. Ion diffusion needs to be optimized because it has the largest time constant[194,195]. The charge transfer resistance becomes dominant. Smaller particles increase the surface and decrease length for solid-state diffusion. Higher porosity also increases the effective diffusion[196]. These differences impact the aging behavior of the cells[197,198]. Most importantly, high energy cells are more prone to lithium plating due to decreased kinetics as described above[198].

2.3.2 Charge Throughput

The dependency of cyclic aging on the charge through-put was discussed by Cloos et al.[2]:

*... the capacity fade dependency on time or charge throughput can show three different **trajectories** – accelerating, linear and decelerating.[111,199] To describe a decelerating trajectory, a root-square dependency was commonly used to account for diffusion limited steady-state growth[200] and Solid Electrolyte Interface (SEI) growth[201] which was especially applied for calendar aging.[202,203] However, Attia et al.[204] have pointed out that SEI growth is not always diffusion limited. A transition over the different potencies of time from 1 over 0.5 to 0, which vary from reaction to diffusion and migration limitation of the SEI, were coupled by Kolzenberg et al.[100] Cyclic aging data can follow a power law less than 0.5.[204,205] In other cyclic aging studies a linear dependency of the charge throughput has been*

found.[203,206,207] Kolzenberg et al.[208] correlated a transition from square-root to linear dependency during cyclic aging to decreased self-repairing of the SEI. These models mostly neglected the appearance of sudden deaths.[206] This seems adequate as the sudden death usually happens after reaching a remaining capacity of 80 %[206,209] which is defined as End of Life (EoL) by USABC test procedures.[210] [2]

Even though these sudden deaths also called “**knees**” are not usually considered for aging modeling, the prediction is highly interesting. From a physical point of view, Attia et al.[199] have identified six pathways resulting in a knee – lithium plating, electrode saturation, resistance growth, electrolyte and additive depletion, percolation-limited connectivity and mechanical deformation. Depending on the pathway, the knees can have a snowball, hidden or threshold trajectory. What’s more, lithium plating can show in different forms. For example, C-rate independent lithium plating can occur due to loss of active material of the negative electrode (LAM_{NE}) when the negative electrode becomes limiting. The consequence is the same as for an initially misbalanced LIB. C-rate dependent lithium plating occurs due to high charging rates and low temperature but also due to mechanical stresses, LAM_{NE}, pore clogging and decreased charge-transfer kinetics.

Different combinations of electrical load or lack thereof alter the aging behavior which is called **path dependency**. Calendar and cyclic aging were found to be highly non-linear in superposition[211]. Long continuous cycling without rest was detected to be particularly harmful[212]. One mitigating effect during resting could be, that the homogeneization of uneven lithium distribution leads to capacity recovery[180]. In direct comparison, cells aged under different sequences of the same load including rest revealed small but relevant differences in capacity and resistance[213]. Karger et al.[214] proposed the non-commutative capacity fade not be the correct metric for measuring path-dependent aging.

2.3.3 Temperature Level

Temperature is a high ranking aging stress-factor as summarized by Cloos et al.[2]:

*An important stress factor on cyclic aging is temperature.[11,17] To account for the temperature influence on capacity loss during aging, the **Arrhenius** relation (1) [Eq. 2.1][215] was proposed to model the temperature dependency of SEI growth,[216], including the activation energy E_A , Boltzmann-constant k_B and temperature T . [2]*

$$r = A \cdot \exp\left(-\frac{E_A}{k_B \cdot T}\right) \quad (2.1)$$

This relation was also found for the temperature dependency of cyclic aging.[201,217] In this case, a second temperature regime that is governed by a different aging mechanism was found.[207] Therefore, a double exponential form is used to describe both increased SEI growth and manganese dissolution at higher temperatures and lithium plating at lower temperatures on the example of an NMC/LMO blend positive electrode.[11] This dependency was also applied to other systems.[14,16,17] For this approach, a linearization of the aging rate is assumed.[11] [2]

Few experimental studies exist on the **temperature dependency of different LIBs** which were mainly differentiated by the cell chemistry. For NMC alone, different optimum aging temperatures were found. Preger et al.[15] observed decreasing capacity loss for higher temperatures which is in line with few studies showing less capacity fade for higher aging temperatures of around 45 °C[218,219]. Schuster et al.[209], however, found the least resistance increase for 25 °C rather than 35 °C. Yang and Wang[14] differentiated not between the cell chemistry but between EV and plug-in hybrid electric vehicle cells. They found an optimum aging temperature of around 20 °C for their NMC622 graphite PHEV cell and 35 °C for the electric vehicle cell with thicker electrodes and lower initial porosity. In comparison, LMO is

attributed to have poor cycling stability at higher temperatures[94]. Contrarily, LMO fared better during aging in an NMC-NCA-LMO blend[87]. The optimum aging temperature for such blends was found around 25 °C for NMC-LMO cells[11,220]. This supports the conclusion that not only the cell chemistry[15] but other stress-factors like the C-Rate[12–14] and cell design factors such as the electrode thickness and energy density[12–14] impact the aging behavior at different temperatures. This is also dependent on the dominant aging mechanism which is linked to the temperature dependency[12,13,15].

Path dependency was also reported for the stress-factor temperature level. Different temperatures during charging and discharging resulted in different temperature dependencies. Instead of an Arrhenius dependency, Ruiz et al.[221] proposed a quadratic relationship of the charging temperature and a linear with discharging temperature. The highest capacity loss was seen for a discharging temperature of -5 °C and charging at 30 °C. This is different for fast charging. There, the temperature is proposed to be drastically increased and then decreased again during discharging which prolonged the lifetime of the cell[222]. Feinauer et al.[223] changed the temperature not during every cycle but after some cycles. Changing from low temperature cycling to high temperature cycling did not affect the aging rate. Aging at high temperatures reduced lithium plating risk at subsequent aging at lower temperatures.

2.3.4 Inhomogeneous Temperature

While the overall aging temperature is unarguably important, the effect of different local temperatures on aging was discussed by Cloos and Wetzel[1]:

Moreover, the temperature inside lithium-ion battery cells can become inhomogeneous during application due to an interplay of heat flux and solid state-diffusion.[22] Temperature differences arise depending on the current rate (C-rate),[19] the cell format and material

loading,[19] tab design[24,190,224] and the cooling scenario.[23,24] For example, in case of an 16 Ah nickel manganese cobalt oxide (NMC)/graphite pouch cell, forced air cooling at 25 °C and 8C loading, Waldmann et al.[19] found the in-plane gradient to be at a maximum of 10.5 K. On a 1.5 Ah NMC / graphite pouch cell with in-built sensor, they concluded the through-plane thermal gradient to be an order of magnitude lower. Another study on 20 Ah lithium iron phosphate pouch cells and extreme conditions such as low ambient temperatures (-10 °C) and high C-Rates (10C) revealed an in-plane and through-plane temperature difference of 18-20 K.[18] [1]

Nonuniformities in temperature have shown to cause nonuniform aging.[47,225] Oftentimes, areas of higher temperature, usually in the cell center, are prone to lithium plating due to an interplay of increased temperature and current density.[3,47,110,225,226] More specifically, the temperature and current distribution was suggested to cause a lithium concentration gradient which breaches the operating potential window.[47] Changes in the local potential were also observed by others.[225,227] Also, on a smaller scale, the lithium deposition rate was proven to increase in areas of thermal hotspots due to increased current densities.[228] [1]

However, for cells exposed to a thermal gradient, lithium plating was also found in lower-temperature areas of the cells during fast charging[186] and normal cycling.[45] The intercalation reaction is strongly Arrhenius-dependent.[229] Sun et al.[227] could explain this shift from plating at the area of higher to lower temperature. At the beginning of charging, the plating occurs at the area with higher temperature due to increased current density and then begins to accelerate in the area of lower temperature due to the named increased resistances. The shifting to the area of lower temperature increased with increasing temperature difference. [1]

Not only the temperature difference but also the direction of the gradient was found to alter the aging mechanisms.[23,48,110] This is true for both the direction of through-plane and in-plane thermal gradients[23,110] as well as the location of negative and positive electrode relative to the through-plane gradient.[48] In-plane thermal gradients did not cause a higher amount of lithium plating compared to a cell at the average temperature.[110] Also, for other aging mechanisms, Paarmann et al.[45] could correlate local aging behavior to the local temperature. A different behavior was observed for through-plane gradients. As soon as the negative electrode temperature is below the positive electrode temperature, lithium plating is favored.[110] When the negative electrode temperature is higher than the positive electrode temperature, increased positive electrode degradation was observed.[48] [1]

For the overall capacity loss under cyclic aging with thermal gradients, different conclusions were drawn. In one experimental cyclic aging study[17] on commercial cells with a superimposed thermal gradient, the authors compared the aging behavior to a cell aged at the average homogeneous boundary condition. In this study, the capacity loss for a cell with an in-plane thermal gradient of 50 K (0-50 °C) were found to be comparable to a cell aged at 25 °C. In a simulative study, the hypothetical average aging temperature was found to increase by 10% of the temperature difference in comparison to the mean temperature.[40] Contrarily, through-plane thermal gradients due to surface cooling have shown accelerated capacity loss in comparison to in-plane thermal gradients due to tab-cooling.[23] Even though the surface cooling led to lower average temperature and therefore less aging than expected from an aging law, the temperature difference caused accelerated aging. A positive feedback mechanism was found between current inhomogeneity, inhomogeneous aging and resistance increase.[42] Others predicted the opposite. They have simulated a reduction in impedance gradients in the cell due to the higher

stress and rise of the impedance in areas of higher temperature.[40,41] In the case of increased fundamental aging for higher temperatures, tab cooling was found to result in a higher aging rate than surface cooling.[230] The influence of through-plane thermal gradients was also investigated in a coin cell setup. The capacity fade was massively increased with a superimposed through-plane thermal gradient.[48] [1]

Regarding the impact of gradients on the aging behavior of single cells, both a positive and a negative feedback mechanism have been postulated. This is similar for parallel connected cells with inhomogeneities. Parallel connected cells were previously used to represent a single cell.[23,231] Parallel connected cells with different SoH have shown to converge over the course of aging.[35] However, in other experiments with superimposed thermal gradients[232,233] or inhomogeneous temperature fields due to self-heating[234,235] no such converging was observed. On top, thermal gradients have caused accelerated aging in parallel connected cells.[32,236,237] Marlow et al.[43] found that the cells could only converge during aging under homogeneous temperature and not with thermal gradients. [1]

2.3.5 Temperature Changes

The temperature is not only inhomogeneous in application but can also be transient. During real-life driving cycles and during fast-charging, the temperature can increase rapidly[20,21]. These changes are considerably faster than the observed temperature path dependency by Feinauer et al.[223]. Cloos et al.[3] summarized the known effects of these temperature changes on aging:

Werner et al.[44] have seen a significantly increased capacity loss for cells, that cycled while constantly changing the temperature between

0 °C and 50 °C. Both Paarmann et al.[45] and Carter et al.[26] detected **lithium plating** for cells subjected to a temperature change. [3]

Additionally, the **temperature of a cell after lithium plating** already occurred seems to be a decisive factor for the further aging, as it impacts the reaction rate of the plated lithium with electrolyte. Plated lithium from low temperature cycling can react with the electrolyte to insoluble and hardly conductive products.[112] SEI formation is mostly accompanied with gas evolution.[83] If gassing due to the reaction of electrolyte with plated lithium occurred, this gassing is intensified by storing that cell at a higher temperature of 40 °C.[238] Chang et al.[46] did not only increase the ambient temperature from 10 °C to 60 °C, but kept on cycling, which led to rapid failure of the cells. This cell failure was also induced by the reaction of lithium-rich SEI with electrolyte, which led to severe gassing.[46] The change to a higher temperature is also suspected to be of importance by Paarmann et al.[45] They suggested, that increasing the temperature from 0 °C to 50 °C during charging influences the reaction rates of all occurring processes slightly different enabling lithium plating.[45] [3]

2.4 Interim Conclusion

In previous chapters, main aging mechanisms of LIB and aging stress factors were summarized from literature. All in all, understanding the interaction of stress-factors and aging mechanisms is very complex. Thereby, not only the applied stress-factors during cycling but also cell design parameters can alter the aging behavior and induce inhomogeneities (Figure 2.6). It became obvious that, even when focusing on one stress-factor, even other effects need to be taken into account.

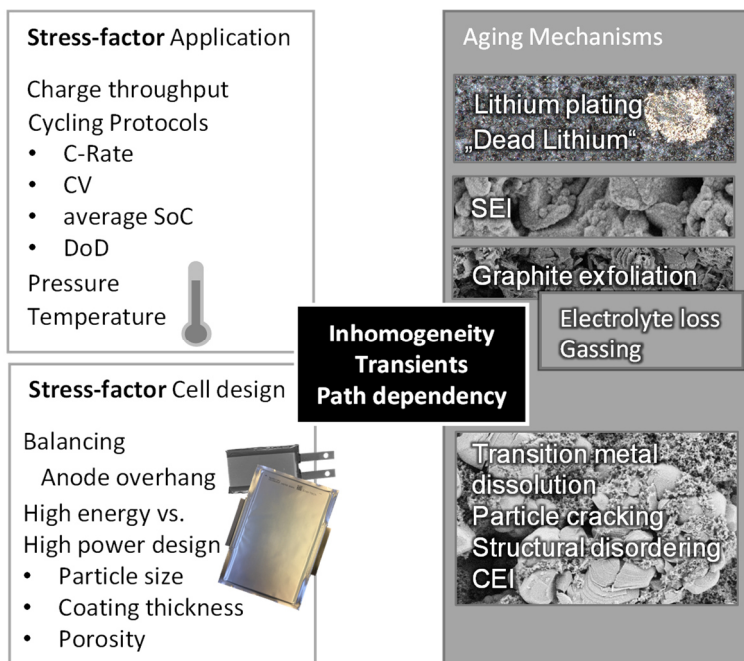


Figure 2.6: Summary of stress-factors and aging mechanisms from literature (part of figures reproduced with permission under the terms of Creative Commons Attribution 4.0 License CC BY.[2] Copyright 2024, The Authors. Published on behalf of The Electrochemical Society by IOP Publishing Limited and with permission under the terms of Creative Commons Attribution 4.0 License CC BY.[1] Copyright 2025, The Authors. Energy Technology published by Wiley-VCH GmbH.).

Firstly, relevant **stress factors** during application were summarized to be the charge-throughput or time itself, the cycling protocols, pressure and temperature. Path dependencies and inhomogeneities add complexity. Secondly, the presented stress-factors can have a different effect depending on the investigated cell. It is known that different electrode chemistries age differently. Also, the balancing of positive and negative electrode which can change due to aging might accelerate aging. Another related cell design

factor is the anode overhang which is one cause of inhomogeneous lithiation. More generally, the electrode coating design also affects the aging behavior. A high-power cell is able to endure higher currents without plating. This is achieved by optimizing particle sizes, coating thicknesses and porosities.

The global aging behavior of capacity loss and resistance increase is determined by the underlying **aging mechanisms**. The interplay between the aging mechanisms of the positive electrode (structural disordering, CEI, transition metal dissolution, particle cracking) and the negative electrode (SEI, Lithium plating) with the respective activation at certain aging temperatures, charges or voltages are essential. Furthermore, both thermodynamic and kinetic processes are relevant for aging. Therefore, multiple analysis methods such as DVA, EIS and PMA are applicable.

Temperature is one of the most important aging stress factors and the temperature field in LIB can be inhomogeneous and transient during application. However, only few experimental and simulative aging studies specifically tested steady-state **inhomogeneous and transient homogeneous temperature** boundary conditions. Judging by the capacity loss acceleration, thermal transients caused a strong acceleration while different results were obtained for the impact of inhomogeneous temperatures. Even though thermal transients have caused strong aging acceleration for most tested conditions, the exact reason is not entirely clear yet. The effect of inhomogeneous steady-state temperature fields during cyclic aging on the capacity loss is in part contradictory in literature. This is problematic because inhomogeneities were predicted to become more important in larger format cells. The interplay of temperature, current and aging was suggested to be important and can either be negative or positive. Furthermore, different results for through-plane thermal gradients versus in-plane thermal gradients are possible.

These (partially) contradicting results in literature lead to the following relevant research questions:

- I. Storch et al.[47] suggested a suppression of gradients to be critical for a long lifetime of large format LIB. In their study, they found local lithium plating caused by a relation of temperature, current density and lithium concentration gradient.
Can this conclusion be confirmed and substantiated?
- II. Are through-plane thermal gradients worse than in-plane thermal gradients?
- III. Why do thermal transients increase capacity loss during cyclic aging?

To answer these complex questions, further investigations are necessary to evaluate the dominant aging mechanisms on a specifically extended database. To do so, the interaction of aforementioned aging-stress factors and aging mechanisms need to be taken into account when designing and performing the experiments and analysis. The latter analysis will be supported by developing an aging model that bridges the gap between global aging and local aging phenomena observed at the end of life.

3 Methods – Locally Resolved Aging Experiments and Model

As shown in chapter 2, the impact of inhomogeneous and transient temperatures on the aging behavior has varied from study to study. One of the few experimental aging studies in literature was performed on a 3 Ah NCA-LCO / graphite pouch cell[17,30,44,239]. This experimental study is taken as the basis of this work but will be substantially extended (Figure 3.1, left).

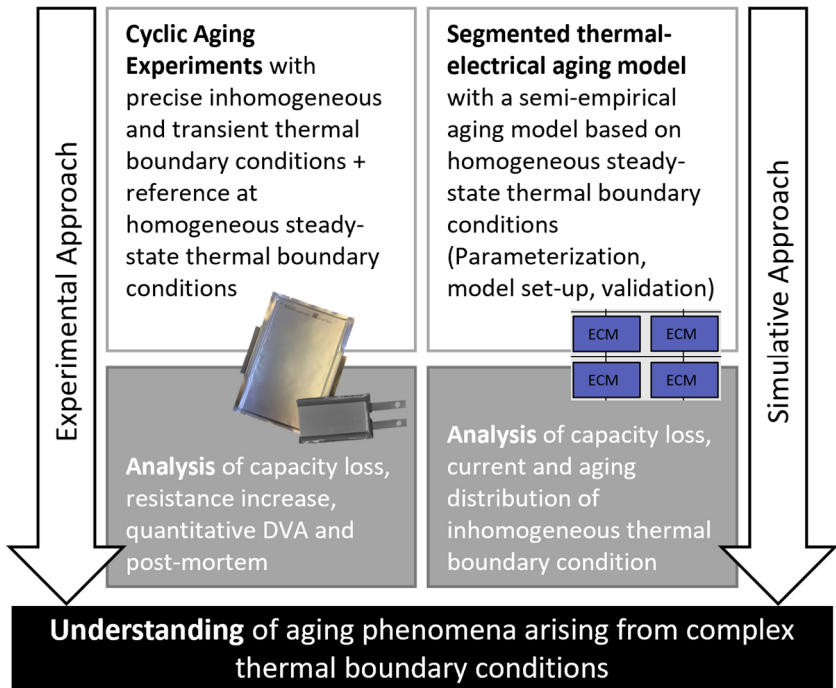


Figure 3.1: Overview over the methods to analyze the effect of complex thermal boundary conditions on the cyclic aging behavior of lithium-ion batteries.





Modeling can be used as an additional tool to predict relations of local variables inside the cell. The internal parameters in a cell are not easily measurable without altering the cell itself which can result in slightly accelerated aging[38] or neglecting compression[240]. For modeling, a similar approach as the former successfully validated model for inhomogeneous aging by Li et al.[42] is chosen in this investigation. A segmented thermal-electrical aging model is used to simulate the internal aging, current and temperature distribution which was found detrimental to some aging phenomena[42,47]. These experimental and simulative methods are then used to improve understanding of the aging behavior under complex thermal boundary conditions as summarized in Figure 3.1.

3.1 Electrochemical and Aging Experiments

To get a larger data basis on the aging behavior of LIBs with superimposed complex thermal boundary conditions, multiple **cells** are investigated. Comparisons are made to the previous aging study on the 3 Ah NCA-LCO / graphite cell[17,44,45,241] – now referred to as “Kokam” (Kokam Co., Ltd., Suwon). Additionally, a larger scale 20 Ah NMC111-LMO / graphite “Enertech” (SPB58253172P2, Enertech Internation, Inc.) pouch cell[2] was chosen. The cell was specifically selected due to its larger size and its comparability to the “Kokam” cell. Storch et al.[47] suggested inhomogeneities to be particularly important for the operating window of large format LIB. The chosen larger format “Enertech” cell is tolerant to higher C-rates which is comparable to the high-power cell “Kokam”. Furthermore, the “Enertech” has the optimal tab configuration of long thin tabs in counter tab configuration. This configuration decreases temperature inhomogeneities arising from the tab design[190]. Also, a small scale NMC532 / graphite 3.4 Ah pouch cell (“L 3.4”) was aged[3]. NMC532 was a state-of-the-art positive electrode material in 2018[242]. The cell has a lower maximum charging C-rate. It serves as a counterpart to the other cells. Lastly, a shorter aging test series was conducted on 1 Ah nickel rich NMC / Si-graphite pouch cell “L 1”

which is a more current electrode material (made to order by ISEA, RWTH Aachen). The investigated cells are listed in Table 3.1.

Table 3.1: Investigated cells with nominal capacity C_N , cell chemistry and investigated thermal boundary condition.

Cell names (based on manu- facturer)	C_N / Ah	Cell chemis- try	Thermal boundary conditions	Ref.
"Kokam" 	3	NCA-LCO / graphite	T, I_y	[17,44,45,241]
"Enertech" 	20	NMC111- LMO / Graphite	I_z, I_y	[1,2]
"L 3.4" 	3.4	NMC532 / Graphite	T, I_z	[3]
"L 1" 	1	Ni rich NMC / Si-Graphite	T, I_z	-

The focus of the aging test series was on the **complex thermal boundary conditions**. These were homogeneous transient boundary condition T , an inhomogeneous steady-state boundary condition with a gradient through-plane I_z and an inhomogeneous steady-state boundary condition with a gradient in-plane I_y . For reference, additional test points with a homogeneous and steady-state boundary condition at the respective equivalent aging temperature T_{EAT} were performed. The equivalent aging temperature is a temporal and spatial mean temperature[17].

The aging experiments require customized test stands for the individual cells for the application of inhomogeneous and transient temperature boundary conditions. Furthermore, different non-destructive and destructive analysis techniques need to be applied to analyze the aging mechanisms and degradation modes and to parameterize the model. The following subchapters summarize the experimental procedures of the performed electrochemical-thermal characterization and validation as well as aging studies on four different cells.

The electrochemical-thermal characterization and procedure was developed and implemented in collaboration with Oliver Queisser at TVT (KIT). The aging study on the “Kokam” and its experimental setup is published in Werner et al. [17,44]. The aging study on the “Enertech” and “L 3.4” including the experimental procedure is published in Cloos et al.[1–3,243,244]. The “L 1” was aged in the same test rig as the “L 3.4” with few adjustments.


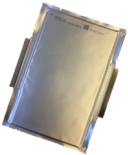
3.1.1 Experimental Setups

Since the focus was on temperature, other stress factors were kept constant. This concerns both electrical and mechanical stresses. Therefore, the cells were compressed with springs and plates at a constant pressure of 0.5 bar. Furthermore, gapfillers (TGF-V-Si, HALA Conec GmbH & Co. KG) were used between the thermal plates for electrochemical characterization and aging tests. An optimum level of **compression** reduces capacity loss due to reduced layer delamination or contact loss[245]. It also leads to a higher reproducibility during aging[246].



Electrical boundary conditions during cyclic aging were also kept constant for all test points. A similar testing procedure to the aging experiments of the “Kokam” was chosen for the “Enertech”. CC charging and discharging without pauses and CV phases between the cut-off voltages of 3 V and 4.2 V were applied. Pauses and CV phases were neglected to reduce the testing time. Furthermore, the lack of pauses and CV phases reduces the effect of

the anode overhang[174]. Another smaller test series on the “Enertech” was performed with a DoD of 70 % from the upper cut-off voltage. Similarly, the aging tests on the “L 3.4” and “L 1” were done with a DoD of 70 % from the upper cut-off voltage. The C-rates during cyclic aging for the different cells are listed in Table 3.2.

Table 3.2: Electrical boundary conditions during cyclic aging (“Cycling”), checkup (“Aging”) and electrochemical characterization (“Char”) for the investigated cells.

Cell names	C-Rate				EIS Amplitude, min. max. frequency f	Ref.
	<i>Cycling</i>	C_N	$qOCV$	<i>Pulse</i>		
“Kokam” 	3C CC, DoD: 100 %,	C/2	Aging: C20 Char: C40	Aging: 1C	Aging: 1 A, 2.5 mHz < f < 100 kHz Char: 500 mA, 5 mHz < f < 80 kHz	Aging: Werner et al.[17,44]
“Enertech” 	2C CC, DoD: 100 %, (70 %) ¹	C/2	Aging: C10 Char: C40	Aging: 1C Char: C/2	Aging: 1 A, 10 mHz < f < 30 kHz Char: 1 A, 5 mHz < f < 50 kHz	Aging: Cloos et al.[1,2]

¹ If indicated in the figure.

	$C2_{ch}$ $(C5_{ch})^1$ $1C_{dch}$ CC, DoD: 70 %	C/3	Aging: C15	Aging: 1C	Not pre- sented	Aging: Cloos et al.[3]
	$C2_{ch}$ $C3_{dch}$ CC, DoD: 70 %	C/3	Aging: C15	Aging: 1C	Not pre- sented	-

The **checkups** during cyclic aging, also called reference performance tests (RTP), were conducted in regular full cycle intervals. The number of full cycles were increased for cycle aging tests at lower aging temperatures to reduce pauses before the checkups. Smaller pauses were not critical for these conditions because they rested at the nominal voltage and at a low temperature. The checkups were always performed in the same manner. In a first step, the temperature was set to 25 °C and relaxation was checked with the cell surface temperature and the cell voltage. Then, the cells were charged with nominal C-rate and a CV phase to the upper cut-off voltage. Again, relaxation was awaited before the nominal capacity measurement in discharging direction was conducted. Then, the cells were charged again to the upper cut-off voltage and the quasi-OCV (qOCV) measurement is conducted in discharging and in some cases also in charging direction. Naturally, the checkup time during aging experiments should be reduced to minimize its impact on the aging result[247]. Therefore, the C-rates for qOCV measurement during cyclic aging were optimized for DVA previous to the aging experiments. Then, from 100 % SoC, the cells were discharged Ah based to multiple SoC points with respect to the previous nominal capacity measurement. At the respective SoC, after relaxation, an impedance measurement was performed. Again, the impedance measurement settings were optimized with regards to the testing time. Then, a pulse measurement was

performed in discharging direction. At lower SoCs, the pulse was performed in charging direction. The exact parameters are given in Table 3.2.

The **electrochemical characterization** measurements differ slightly from the checkup routine. They are optimized towards precision and not towards time efficiency. Therefore, the qOCV is always performed with C/40. More SoC points for impedance and pulse measurements are performed. They were optimized in a range from 0 % SoC to 100 % SoC in 5 to 10 % steps. The overvoltages during charging and discharging differ. The name “resistance hysteresis” was introduced for this phenomenon[248]. Therefore, pulses were also performed in charging direction. The same procedure was performed from 5 °C to 45 °C in 10 K steps.

The **measurement equipment** for the electrochemical characterization and cyclic aging measurements are listed in Table 3.3. The impedance measurements were conducted with a Zennium and multiplexer either PMUX for electrochemical characterization and BC-MUX for aging checkup (Zahner-Elektrik GmbH & Co. KG). To measure impedance spectra above 4 V, a powerpotentiostat P242 was additionally added for electrochemical characterization (Zahner-Elektrik GmbH & Co. KG). All test facilities were automated using LabVIEW (National Instruments). The processing of the obtained measurement data was done in a routine in MATLAB®.

Table 3.3: Used equipment for electrochemical characterization and cyclic aging tests.

Test stand	Cycler	Impedance	Cryostats	Ref.
Electrochemical-Thermal Characterization	BaSyTec CTS (BaSyTec GmbH)	Zennium + PMux (Zahner-Elektrik GmbH & Co. KG)	RE1250S; RE1050S (LAUDA DR. R. WOBSE GMBH & CO. KG))	-
Cyclic aging	BaSyTec	Zennium +	ECO 4S; RE1050S;	[1,2]

“Enertech”	XCTS (BaSyTec GmbH)	BCMux (Zahner- Elektrik GmbH & Co. KG)	VARIOCOOL 2000 (LAUDA DR. R. WOBSE GMBH & CO. KG)	
Cyclic aging “L 3.4” and “L 1”	BaSyTec CTS (BaSyTec GmbH)	Zennium + BCMux (Zahner- Elektrik GmbH & Co. KG)	RE1050S (LAUDA DR. R. WOBSE GMBH & CO. KG)	[3]

The test setup for **entropy coefficient measurement** of the “Kokam” with a standard potentiometric procedure and a novel procedure was performed. The novel method and experimental setup is described in detail in Widanage et al.[249]. Two different methods are common to measure the entropic coefficient, namely the potentiometric and calorimetric method[250]. The first needs equilibrium at multiple SoC and temperature points[251,252], while the second subtracts the heat generation during discharge and charge[253,254]. The potentiometric method was suggested to be more accurate[255].

A precise **temperature control** of the pouch cells was achieved with thermal plates in all aging studies[1–3,17] and also in electrochemical characterization. The thermal plates were supplied with water from thermostats and cryostats as summarized in Table 3.3. Only the frequency controlled and standard potentiometric measurement of the entropy coefficient of the “Kokam” cell was performed with Peltier elements[249]. A thermal plate setup has shown to increase temperature homogeneity and reduce the maximum temperature[256] due to a high heat transfer coefficient[17]. Enhanced thermal control further improved modeling accuracy in comparison to forced air cooling with a climate chamber[257]. Thermocouples of type K (ES Electronic Sensor GmbH) ensured temperature control on the surface of the cells with previous calibration (OCEANUS-6 series, millik

precision thermometer, PT-25 reference thermometer (Isothermal Technology Limited))[2]. Cyclic aging is performed in a temperature range of 3 °C to 48 °C. The exact measured mean temperature during cyclic aging is given in the Appendix "Cyclic Aging Studies". In this work, the test conditions are addressed with the "cell names" also given in the Appendix "Cyclic Aging Studies". Reproduction tests were performed for most test conditions and indexed with "b, c, ...". Generally, it was concluded that testing of at least 9 to 13 cells for each condition is necessary to account for cell-to-cell variability[258]. However, this was practically not feasible. Therefore, initial testing of the cell-to-cell differences in nominal capacity were performed[1,3]. Previous to the aging study, the optimum post-formation procedure was investigated for the "Enertech" by tracking the capacity and resistance. Four C/2 full cycles were performed on the "Enertech". Post-formation cycles were neglected for the "L 3.4" to accelerate the aging tests.

The temperature control was further refined for the application of **thermal gradients** which is presented for the "Enertech" cell by Cloos and Wetzel[1]:

A schematical depiction of the thermal plate setup for in-plane (I_y) and through-plane (I_z) thermal gradients is given in Figure 1a,b [Figure 3.2]. In the case of a through-plane gradient, the thermal plates on either side of the pouch cell had different temperatures (Figure 1a) [Figure 3.2]. The in-plane gradient was achieved with fluid channels at different temperatures over the width of the pouch cell stack (Figure 1b) [Figure 3.2]. The temperature on the pouch cell surface was controlled with thermocouples with a diameter of 0.5 mm placed on top of the pouch cell (type K, ES Electronic Sensor GmbH)). The position of these thermocouples depends on the direction of the thermal gradient. They were either positioned in the center on each side of the pouch cell (through-plane gradient) or at the edge of the pouch cell stack underneath the fluid channel (in-plane gradient). The height of the thermocouple was compensated using a 1 mm gap filler (TGF-V-Si, HALA Conec GmbH & Co. KG) indicated in a dark grey. [1]

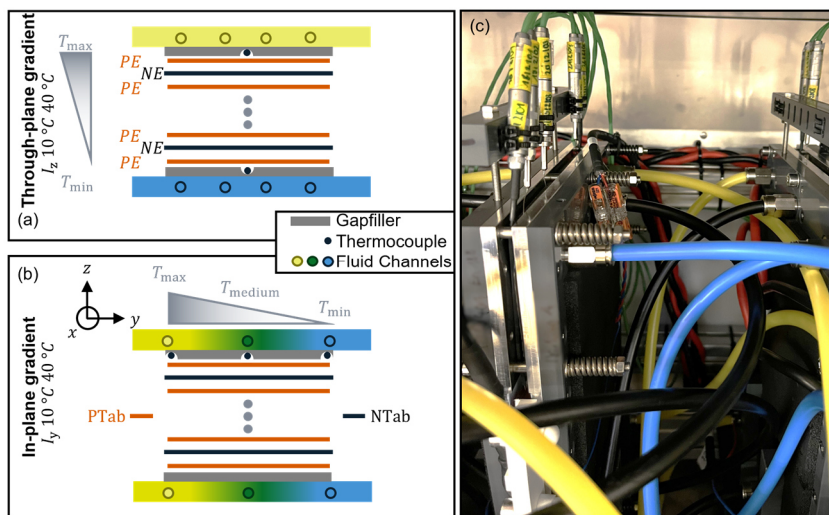


Figure 3.2: Schematic of (a) in-plane and (b) through-plane thermal gradient with thermal plates and thermocouples and (c) picture for an in-plane thermal gradient (Reproduced with permission under the terms of Creative Commons Attribution 4.0 License CC BY.[1] Copyright 2025, The Authors. Energy Technology published by Wiley-VCH GmbH.).

Special emphasis was put on the tab cooling. The tab temperature is expected to affect the nearby electrode stack temperature field.[259,260] While this was advantageous for the in-plane thermal gradient, it was expected to disturb the through-plane thermal gradient temperature field. Therefore, the tabs with through-plane thermal gradient were not actively cooled. They were isolated from the thermal plate with a polyoxmethylen layer. In case of active cooling for the in-plane thermal gradient, the tabs were only electrically insulated from the plates via a thin gap-filler (KERATHERM U90K, KERAFOLE Keramische Folien GmbH & Co. KG). [1]

The selection of tested **thermal gradients** for the aging of the “Enertech” cell was further explained by Cloos and Wetzel[1]:

A spatially and temporally average temperature is determined using the concept of the equivalent aging temperature T_{EAT} . [17] Applied on the current problem, the equivalent aging temperature simplifies to an average of the minimum and maximum temperature measured over the cycling time at the spatial boundaries of the cell. Three temperature levels with different temperature differences were selected to ensure a broad test matrix while keeping the electric and fluidic infrastructure reliably manageable. The temperature differences were chosen in the order of 20 K as such values have previously been observed for extreme load scenarios and 20 Ah cells. [18] For each condition, at least one test point was performed with an in-plane and through-plane thermal gradient. A second test point was performed for medium and higher average temperatures. The low to medium temperature test point was between 10 and 25 °C with an equivalent aging temperature of 17.5 °C which is approximately comparable to the cell aged at a homogeneous temperature of 19 °C. The highest temperature difference stretched from 10 to 40 °C which is directly comparable to homogeneously aged cells at 25 °C. The medium to high temperature test point was between 30 and 50 °C. This test point is also directly comparable to the homogeneous test point at 40 °C.

[1]

The application of **thermal transients** on the “L 3.4” cells was explained by Cloos et al.[3]:

To enable fast temperature changes for the transient conditions, the fluid supply was controlled by pneumatic valves. An automatization routine in LabVIEW (National Instruments) controlled a relay that controls the valves. Two cells were cycled in pairs. An example for two cells cycled between 5 °C and 45 °C is given in Figure 6. At one point in time each cell was supplied by one cryostat, thus, had the according

actual temperature T_{act} . As an example, one cell of the pair always had the temperature change from 45 °C to 5 °C at the beginning of charging, while the other cell had the temperature change from 5 °C to 45 °C respectively. This allowed for the specific investigation of the direction of the temperature change during charging. Reaching the final temperature at the surface of the cells took a couple of minutes. The entire charging process lasted about 1 h to 1.5 h at BoL depending on the temperature condition. During the temperature change in these first view minutes, bends in the voltage curves can be seen (Figure 7) [Figure 3.3]. [3]

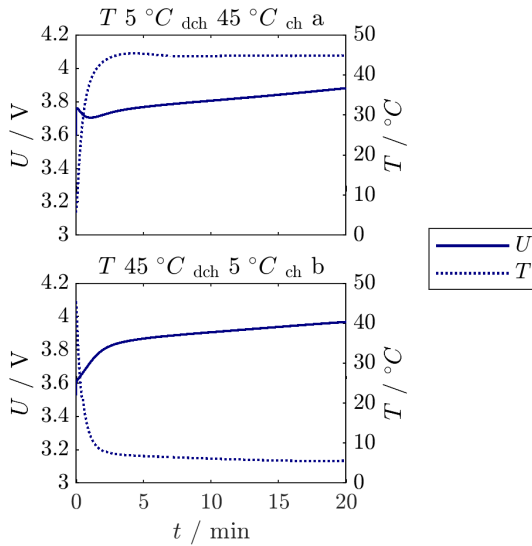


Figure 3.3: Example of voltage and temperature over cycling time in minutes at the beginning of charging with superimposed temperature change from 5 °C to 45 °C (top) and 45 °C to 5 °C (bottom) (Reproduced with permission under the terms of Creative Commons Attribution 4.0 License CC BY.[3] Copyright 2023, The Authors. Batteries & Supercaps published by Wiley-VCH GmbH.).

We assume this to be mainly due to the temperature dependent resistances.[261] A drop in voltage during charging could also be attributed to lithium deposition as seen by Carter et al.[26] during a temperature change. [3]

3.1.2 Non-Invasive Aging Analysis

A combination of different non-invasive analysis techniques to analyse degradation modes and capacity loss trajectories were presented by Cloos et al.[2]:

*To **quantify the degradation modes** via DVA,[130] the approach presented by Schmitt et al.[131] is used. They aligned half-cell DVA curves that can be measured at one point in time to the aged pouch cell DVA curves.[131] Afterwards, the degradation modes could be calculated based on the alignment factors,[131] which was done accordingly in this study. The half-cell measurements at BoL were used for this method. The minimization was performed with the lsqnonlin solver in MATLAB®. Contrary to the method described by Schmitt et al.[131] the voltage curves were used for alignment, which was also previously done by Hu et al.[262]. Another difference to Schmitt et al.[131] is the cut-off at the sides of the voltage curves was increased from 1 % to 5 % to avoid optimization to the steep slopes. [2]*

*As another quantification step, the capacity loss was analyzed for **acceleration onsets and knees**. A Bacon-Watts[263] model which was adapted by Férmín-Cueto et al.[264] to identify knee-points can be used for this purpose. Férmín-Cueto et al.[264] also proposed a double Bacon-Watts function to predict the knee onset. Similarly, we used this double Bacon-Watts function to identify an acceleration onset and the final knee. Again, the lsqnonlin solver in MATLAB® was utilized. [2]*

3.1.3 Post-Mortem Analysis

A **cell opening** of the cells were conducted both at BoL and after cyclic aging in PMA. At BoL, cells were opened to characterize the individual cell components thermally for model parameterization. Furthermore, BoL cell opening is necessary for the half-cell alignment to the full cell, also called electrode balancing, as described in section 2.2.2. Such an electrode balancing was also performed after cycling for the “Enertech” cell to quantify the degradation modes[2]. The opened cells were also used for a visual inspection of the electrode sheets. The procedure differed slightly between the individual cells and can be checked in the respective publications given in Table 3.1. For reference, the procedure on the “Enertech” cell as explained by Cloos et al.[2] is given:

The cells were opened in a controlled inert argon atmosphere in a glove-box. The electrodes underwent a thorough preparation process involving their separation and triple washing with Dimethylcarbonate (DMC) to eliminate any residual conductive salt originating from the electrolyte. Additionally, the active material of the electrodes was delaminated from the current collector on one side through the utilization of N-methyl-2-pyrrolidone (NMP). Circular coins with a standardized diameter of 18 mm were punched out from the electrodes for further experimentation. [2]

*The **experimental cell** configuration encapsulated within a PAT-Cell housing (EL-CELL GmbH) was used for the electrical characterization of the electrodes. In the context of half-cell measurements, negative and positive electrode coins were individually assembled against lithium. For full-cell measurements, a cell with both negative and positive electrode was constructed. The electrode coins were isolated by an insulation sleeve (EL-CELL GmbH), comprising a polypropylene (PP) fiber/polyethylene (PE) membrane, alongside a lithium reference. The*

separator was soaked with 80 μ l LP30 (1M LiPF₆ EC/DMC) electrolyte. [2]

Cycling of the experimental cells was executed utilizing a BaSyTec XCTS (BaSyTec GmbH) from 3 V to 4.3 V for the positive electrode half-cell (positive electrode vs lithium), 0.01 V to 1 V for the negative half-cell (negative electrode vs lithium) and 3 V to 4.2 V for the full cell (negative electrode vs positive electrode). The applied currents for cycling procedures were based on the calculated areal capacity derived from the cell's overall capacity and the aggregate area of the active material. The cyclic protocol included formation cycles before a cycle with C/100 was conducted. [2]

*Samples were cut from the electrodes and washed with DMC. Then, they were only exposed to the ambient atmosphere shortly before inserting them into **microscopes**. Both a digital light microscope (VHX 7000, Keyence Corporation) and a scanning electron microscope (SEM) (LEO 1530 Gemini) were used. For the latter, an acceleration voltage of 2 kV to 5 kV was applied for the SEM images. Energy dispersive X-ray spectroscopy (EDX) was performed with an acceleration voltage of 15 kV. Inductively coupled plasma optical emission spectroscopy (ICP-OES) was applied for the found depositions on the sample 45 °C a. The depositions were scraped off with a scalpel. The sample was dissolved in acid while traces of graphite, that stuck to the depositions, remained. The measurement was conducted with an iCAP 7000 (ThermoFisher Scientific). [2]*

3.2 Segmented Thermal and Electrical Aging Model

In order to simulate the temperature dependent aging behavior, a thermal-electrical aging model is necessary. Multiple modeling approaches exist for the electrical, thermal and aging behavior. A computationally efficient electrical model is the equivalent circuit model (ECM)[265]. The thermal behavior can be modeled based on the heat transfer equation[266]. Aging modeling is mostly dependent on data fitting[267]. Semi-empirical aging models have the advantage of combining simplicity[267] with the inclusion of physics-informed aspects[202].

Oftentimes, electrical and aging models assume a homogenization of the entire cell. These so-called lumped models neglect inhomogeneities by applying only one ECM for the electrical behavior of the entire cell. This assumption leads to unprecise simulation results[42]. **Segmented Models** – in form of electrical circuit network (ECN) models – were first presented by Newman, Tiedemann, Gu and Kwon et al.[268–271] and allowed modeling the current and potential distribution on electrode level. An elemental functional unit in most segmented model approaches within the ECN is described by a unit cell (negative current collector, active material, positive current collector) connected by current collector foils as serial resistances[40,42,272].

A **resolution of the cell stack** is necessary for modeling the impact of an inhomogeneous in-plane and through-plane temperature distribution on the internal cell states such as temperature, current and aging as well as their interaction. Therefore, a 2D segmentation of the cell is chosen in the direction of the thermal gradients which are in the y-z-plane. A schematic depiction of such a 2D resolution with an ECN is shown on the example of the “EnerTech” in Figure 3.4. In comparison to literature, further simplification is explored on the ECN model as a compromise between high modeling accuracy and low computational cost.

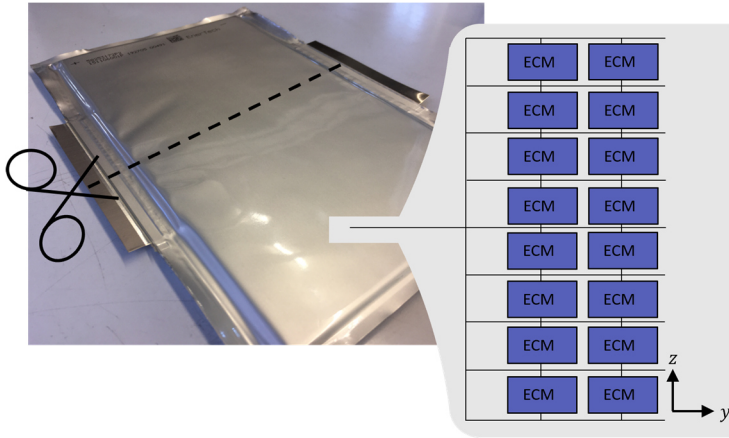


Figure 3.4: Schematic depiction of a network in y-z-plane for counter-tab pouch cells.

Resolving the serial resistances of the current collector foils requires solving Kirchhoffs' circuit laws which adds complexity. This complexity is necessary for resolving the spatial current and voltage distribution resulting from solely the geometry. This might be necessary if extensive lithium plating close to the tab region due to high local currents is observed[187]. However, many arguments speak in favor of simplification. Firstly, the electrical resistances of aluminum and copper are low. Secondly, the thermal gradients chosen in the experiments represent extreme application cases in the order of 20 K[18] and are likely dominating the geometry effect. Neglecting the current collector resistances leads to an **ideal parallel connection** of the ECMs. In an ideal parallel connection, all terminal ECM voltages must be equal.

The thermal-electrical ECN model was developed and implemented in Python by Oliver Queisser at TVT (KIT). An **overview of the thermal-electrical model** is shown in Figure 3.5.

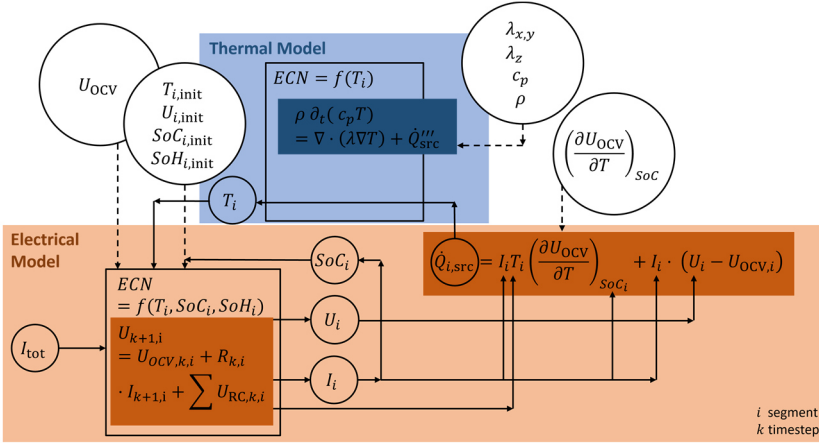


Figure 3.5: Schematic illustration of the interrelations of thermal (blue) and electrical (orange) model.

The interactions of the ECN are shown for an applied total current I_{tot} on a LIB. The output is the SoC, voltage and current distribution over the segments i for the timestep k . With these variables and relevant parameters, such as the entropic coefficient $\left(\frac{\partial U_{OCV}}{\partial T} \right)_{SoC}$, the heat source distribution can be calculated. Together with the thermal material properties, the thermal model predicts the temperature field which is an input in the electrical model.

In the following chapters 3.2.1 and 3.2.2, the fundamentals and additional developments of the thermal-electrical model are highlighted. In chapter 3.2.4, the focus is laid on the implementation of the aging model. Finally, in chapter 3.2.5, the model will be validated. The model development is mainly presented on the example of the “Enertech” which was in focus for the investigation of thermal gradients and aging.

3.2.1 Electrical Network Model

The Thévenin theorem says that parts of an electrical network can be modeled as an equivalent circuit[273]. An overview over different equivalent circuit models for LIB is given by Hu et al.[274]. They differ in capturing dynamic effects, hysteresis and in their order[274]. An appropriate **ECM** needs to be selected for the electrical model.

The parameterization of the ECM and the allocation of electrode processes to the elements is based on the works on time-domain modeling by Gantenbein et al.[139]. The overvoltages result from ohmic losses, contact resistances, charge transfer resistances, SEI and diffusion processes. The contact and ohmic resistances can be summarized. Then, the operating voltage U of the cell can be described as the sum of the open-circuit potential U_{OCV} and the overpotentials η in formula (3.1).

$$U = U_{OCV} + \eta_{\Omega} + \eta_{SEI} + \eta_{CT,PE+NE} + \eta_{Diff} \quad (3.1)$$

Per definition, these overvoltages are negative in case of discharging and positive in case of charging LIB. While processes at high to medium frequencies can be parameterized by EIS, a time domain measurement was proposed for diffusive processes at low frequencies. More specifically, the relaxation after a pulse can be described by formula (3.2).

$$\eta_{Diff} = R_{Diff} \cdot I \cdot \left(1 - \exp\left(\frac{-\sqrt{t}}{\tau_{Diff}}\right) \right) \quad (3.2)$$

This is based on modeling of diffusion processes following a square-root behavior as presented by Pop et al.[275]. Thereby, the decay is dependent on the time constant τ_{Diff} which is equivalent to $(R \cdot C)_{Diff}$.

To obtain a **physically meaningful ECM**, the methodology of Gantenbein et al.[139] needs to be supplemented with knowledge of the time constants of the electrochemical processes. This relation is dependent on the investigated LIB as discussed in section 2.2.2. Stiaszny et al.[147] described the medi-

um frequency impedance of an NMC-LMO cell by SEI, negative electrode and positive electrode processes with decreasing frequency. This knowledge is used to interpret the DRT of the “Enertech”.

The **time constants** can be identified with DRT which was performed by Marc Schiffler at IAM-ET (KIT) with the in-house DRT tool “LinKK” on an aged “Enertech” (light copper in Figure 3.6). The DRT shows four very distinct peaks at 1560 Hz, 690 Hz, 2 Hz and 0.09 Hz.

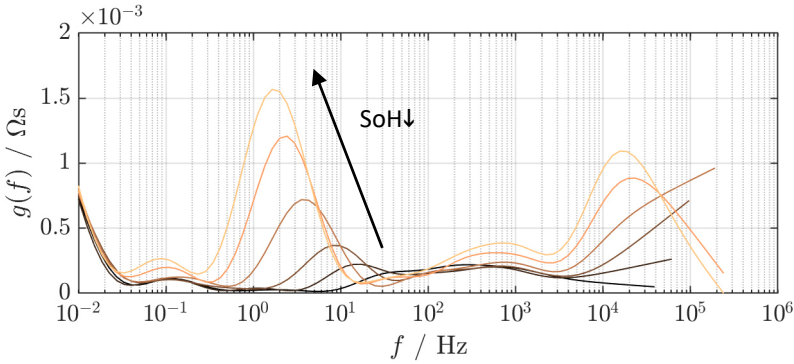


Figure 3.6: DRT of “Enertech” from BoL (black) to aged (copper) during checkups at SoC of 50 % and 25 °C obtained from “LinKK” by IAM-ET (KIT).

A separation of semi-circles in the Nquist plot as well as the peaks in DRT could be observed over aging, indeed[150]. The frequency of the peak at 15600 Hz is very high and in the region of ohmic and contact losses[139]. The less distinct peak in the region of 10^2 Hz and 10^3 Hz describes interfacial losses of the negative electrode including SEI and charge transfer[139]. The most prominent peak at 2 Hz drastically shifted over aging to lower frequencies and can be attributed to charge transfer resistances of the positive electrode[139,147]. A large increase in charge-transfer resistance of the positive NMC-LMO electrode was previously seen by Stiaszny et al.[149].

According to the time constants derived from DRT, the EIS of the “Enertech” can be fitted with an ECM consisting of $(L) - R_{\Omega} - 3RQ - (FLW) - (C)$ which is represented in Figure 3.7 (top left).

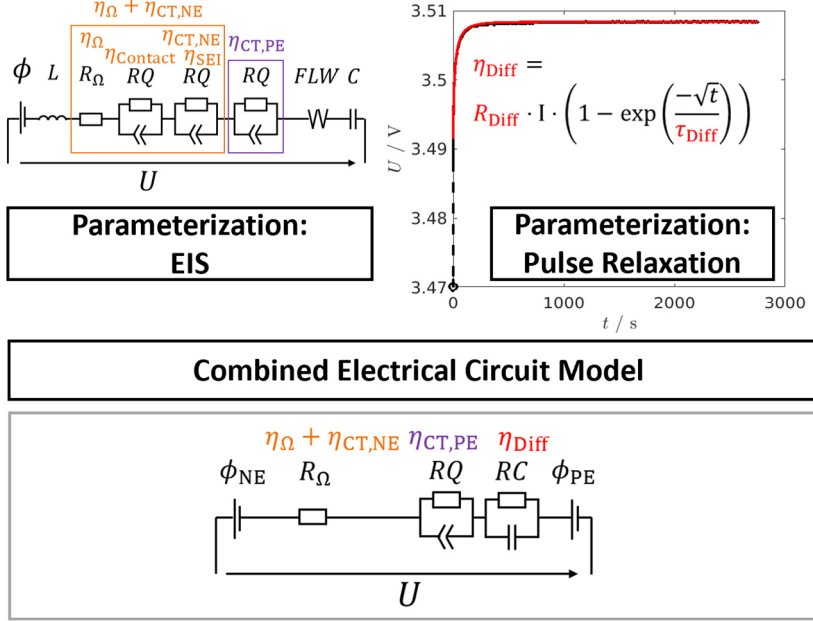


Figure 3.7: Development of an ECM for the electrical model as a combination of parameterization on impedance and pulse relaxation data.

ECM elements in brackets are solely used for fitting the EIS but not for simulation. The model for the “Kokam” cell consists of $(L) - R_{\Omega} - 2RQ - FLW - (C)$. The complex element RQ which is a constant phase element (CPE) only exists in the frequency domain and is later fitted with 5 RC elements each in the thermal-electrical model on the basis of the works of Buller[145] and Handschuh[146]. The ECM fit to the EIS spectrum was performed in the TVT (KIT) in-house tool “LIBMat” implemented in

MATLAB® with the solver *patternsearch*. Start parameters and boundaries for the “EnerTech” were chosen according to DRT results.

The ECM which is parameterized in the thermal-electrical model is a **combination of ECM** elements parameterized on EIS and pulse relaxation data (see Figure 3.7). High frequency processes above 100 Hz in the EIS are simplified because the model is used for time-domain simulation with a minimum time step of 0.01 s which is equal to 100 Hz. The processes are 99 % developed after $5 \cdot \tau$. Therefore, the serial resistor in the combined ECM (see Figure 3.7) represents the sum of the ohmic, contact, SEI and charge transfer resistance of the negative electrode derived from the real parts of the ECM elements. These high frequency processes are called “ohmic resistance” in the following. This ohmic resistance, including the original ohmic resistance parameterized on the EIS, is assumed to be fully attributed to the negative electrode. This assumption is essential for the calculation of the negative electrode potential.

A necessary extension of the thermal-electrical model in for the use of aging is the **electrode potential splitting** as shown by Drees et al. [276] and Zhang et al.[277]. With a regular ECM, only the full cell potential is parameterized. With an electrode equivalent circuit model, the negative electrode potential can be estimated. This is necessary for lithium plating prediction. In this work, the method is applied in a simplified way. The full cell OCV is parameterized with electrode potentials and the alignment factors obtained from balancing as described in chapter 3.1.2. Then, the assumption is made that each single element of the combined ECM is assigned to a specific electrode. As shown in Figure 3.7, $\eta_{\Omega} + \eta_{\text{Contact}} + \eta_{\text{CT,NE}} + \eta_{\text{SEI}}$ are attributed to the negative electrode while $\eta_{\text{CT,PE}}$ and η_{Diff} are attributed to the positive electrode. These assumptions pose some limitation on quantitative interpretations and could be optimized in future work. An example for splitting the ohmic resistance into positive and negative electrode parts is given by Merla et al.[278] and requires further assumptions and modeling. Also, a separation of the diffusion processes of the negative and positive electrode requires

additional measurements. These limitations and additional measurements which are not within the scope of this work are the reason for the simplified procedure. With this procedure, the electrode potential can be calculated for each timestep with formulas (3.3) and (3.4) in this work.

$$U_{NE,k+1} = U_{NE,OCV} + R_{NE,k} \cdot I_{k+1} \quad (3.3)$$

$$U_{PE,k+1} = U_{PE,OCV} + R_{PE,k} \cdot I_{k+1} + \sum U_{PE,RC,k} \quad (3.4)$$

The resistances at BoL are a **function of SoC and temperature**. A small dependency on the current was observed for the charge transfer of the positive electrode[139] which is neglected here. The SoC and temperature dependency is often implemented as a look-up table. In such a look-up table, the parameters are interpolated from existing test points[261,279]. The SoC sampling points in the performed experiments were already finely distributed. Small scattering could be observed (Figure 3.8) which were reduced by applying a spline fit in MATLAB®. Then, the splinefit was evaluated at every 1 % SoC and parameterized as a look-up table. Generally, the trends are as expected with an increase of the resistances towards lower SoCs[280].

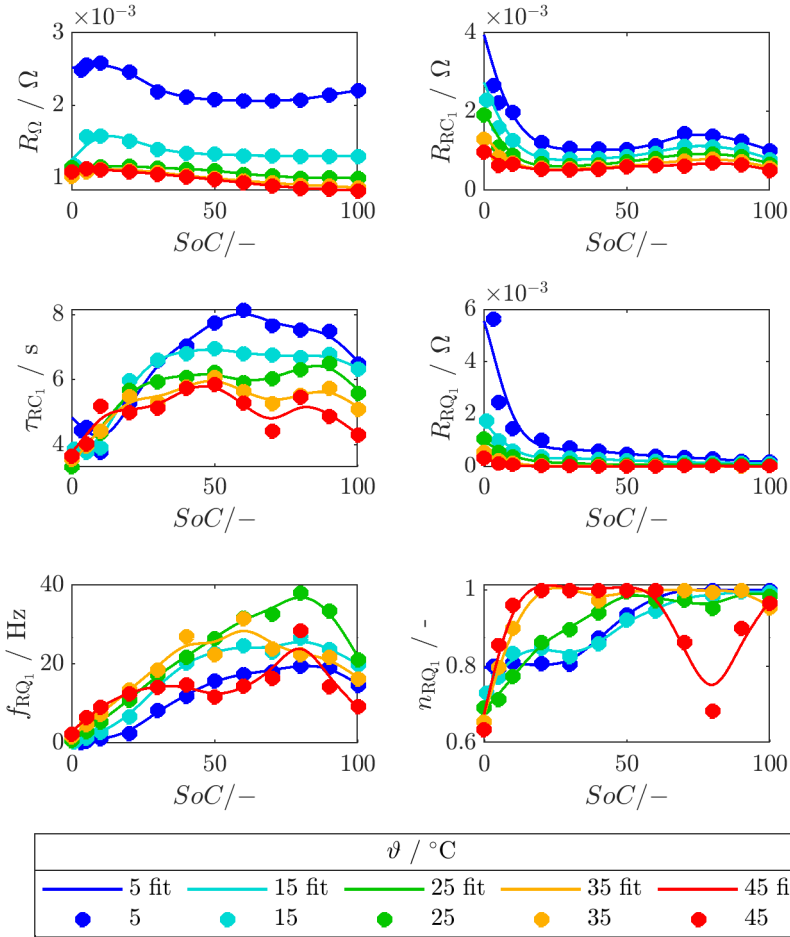


Figure 3.8: ECM parameters as a function of SoC and temperature with spline fits of the “Enertech”.

In the thermal-electrical model, a linear interpolation method for the SoC and temperature dependency was implemented. The temperature dependency of resistances is often described with an **Arrhenius behavior**[138,194]. On the example of the 18 s resistance R_{R18} extracted from a pulse meas-

urement, the temperature dependency is checked in an Arrhenius plot in Figure 3.9 for the “Kokam” and in Figure 3.10 for the “Enertech” cell.

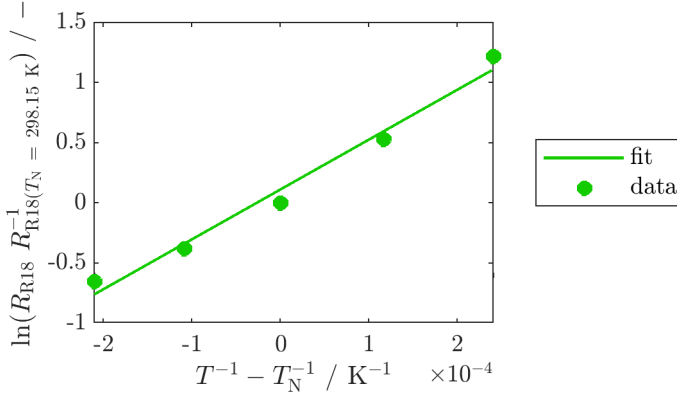


Figure 3.9: Temperature dependency of the 18 s pulse resistance of the “Kokam” at SoC 50 % in an Arrhenius plot with linear fit.

The Arrhenius behavior is confirmed if a linearization can be achieved in an Arrhenius plot. Therefore, the Arrhenius function in equation (2.1) needs to be linearized with a natural logarithm \ln and plotted over the inverse temperature T in K. That means that the temperature decreases with increasing x-axis.

The resistances of the “Kokam” follow the Arrhenius dependency with small discrepancies at the edges at 5 °C and 45 °C (Figure 3.9). For easier model parameterization, the temperature dependency is normed to the resistance at 25 °C. In the model, the SoC dependency is interpolated for a temperature of 25 ° first. Then, the temperature dependency is calculated with the Arrhenius activation.

The discrepancy of the resistances to the Arrhenius behavior is more pronounced for the “Enertech” as can be seen in Figure 3.10 for all investigated SoCs.

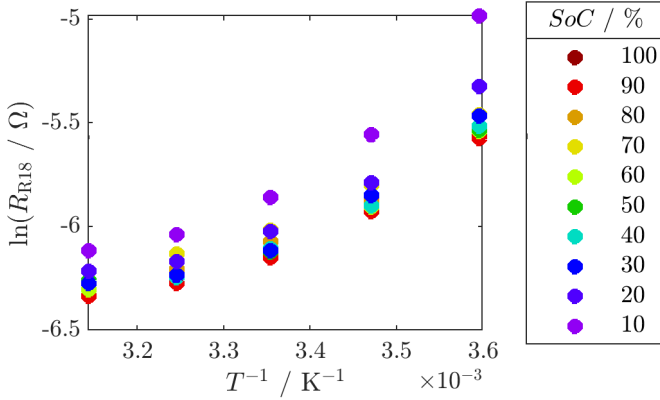


Figure 3.10: Temperature dependency of the 18 s pulse resistance of the “Enertech” at SoCs from 10 % to 100 % in an Arrhenius plot.

This can be attributed to a temperature behavior of the ohmic and diffusive resistance not following an Arrhenius behavior. At higher temperatures, further processes lead to a more linear resistance decay in a non-logarithmic plot. It can be concluded, that an Arrhenius dependency of the resistances of the “Enertech” is not viable. Therefore, the temperature dependency of the resistances was implemented as look-up table for the “Enertech”.

3.2.2 Thermal Model

Thermal models usually solve the energy balance based on the first law of thermodynamics[281] and on the Fourier law to describe the kinetics transfer. The **transient heat equation** – applied on modelling of LIBs[269,282] – takes the following form.

$$\rho \partial_t (c_p(T) T) = \nabla \cdot (\lambda(T, x, y, z) \nabla T) + \dot{Q}_{\text{src}}''' \quad (3.5)$$

The **heat generation** term[254] can be written according to Bernardi et al.[283] when neglecting the enthalpy-of-mixing and phase change terms.

The heat generation term consists of an irreversible and reversible or entropic part. The following notation is according to Gu and Wang[284].

$$\dot{Q}_{\text{src}}'''(T) = I''' \cdot \left[(U_{\text{OCV}} - U) - T \cdot \left(\frac{\partial U_{\text{OCV}}}{\partial T} \right)_{\text{SoC}} \right] \quad (3.6)$$

Both equations require parameterization of the thermal material properties and **entropic coefficient** $\left(\frac{\partial U_{\text{OCV}}}{\partial T} \right)_{\text{SoC}}$. In Figure 3.11, various non-calorimetric methods for the measurement of the entropic coefficient are compared for the “Kokam” cell.

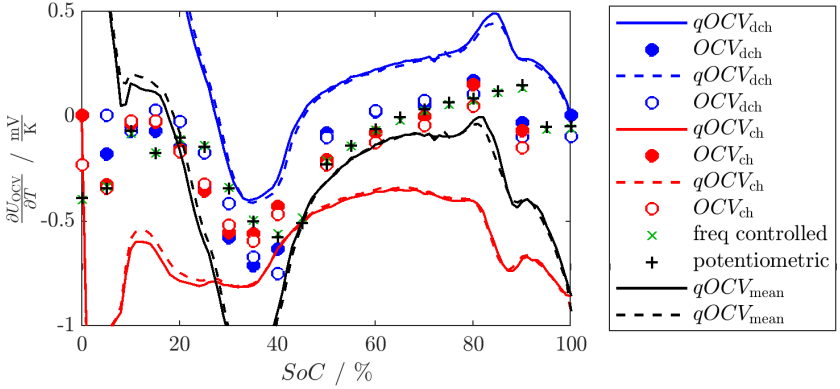


Figure 3.11: Comparison of non-calorimetric measurement methods for the Kokam cell. Reproduction cells are indicated with dashed lines or unfilled markers. Data points for the frequency controlled and standard potentiometric method are obtained from Widanage et al.[249] (Adapted with permission under the terms of Creative Commons Attribution 4.0 License CC BY. [249] Copyright 2025, The Authors. Published on behalf of The Electrochemical Society by IOP Publishing Limited.).

Firstly, a standard potentiometric and a novel frequency-controlled method are shown with green and black crosses respectively[249]. Secondly, the relaxed voltage before impedance or pulse measurements evaluated over 5 °C to 45 °C was extracted from the electrochemical characterization

(circles) which is similar to GITT. A similar method was first presented by Farmann and Sauer[285]. Thirdly, an estimation of the entropic coefficient with the $qOCV$ evaluated at each 1 % SoC point over the characterization temperatures from 5 °C to 45 °C is shown. This was done for two cells (line and dashed line) and also for discharge (dch, blue), charge (ch, red) and average of the two (mean, black).

A **comparison of the entropic coefficient measurement methods** is made on the “Kokam” so that an appropriate method can be applied to the “Ener-tech” at BoL and at aged state. The standard potentiometric measurement serves as reference because it was suggested to be an accurate method[255]. A high agreement can be observed for the frequency-controlled measurement. The entropic coefficient obtained from the OCV in both discharging and charging direction of the electrochemical characterization show very good agreement with the reference except for low and high SoCs. At high SoCs, the discharging direction OCV shows a better agreement while at low SoCs, the charging direction OCV is more accurate. The measurement point of the other direction is not visible in the shown boundaries of -1 to 0.5 mV K⁻¹. This is due to the measurement uncertainties in coulomb-counting of the battery cycler and potential voltage off-set after an impedance measurement of the impedance measurement device. During electrochemical characterization, the SoC points were adjusted Ah-based for each temperature. SoC 100 % was the starting point in discharging and 0 % the starting point in charging direction. This approach is different to the potentiometric measurement for which the SoC was adjusted and then the temperature was changed. Furthermore, the cell and the measurement setup differed for the freq-controlled and potentiometric method in comparison to the $qOCV$ and OCV measurement as described in chapter°3.1.1.

The $qOCV$ measurement method highlights the trend of the entropic coefficient but largely over- and underestimates the coefficient for high absolute values of the entropic coefficient. Also, the mean of the discharging and charging $qOCV$ cannot reproduce the reference measurement result. It can

be concluded that the **quality of the *OCV* measurement** is a time and test equipment efficient alternative to the standard potentiometric and frequency-controlled method. Therefore, the *OCV* measurement method is evaluated for the “Enertech” cell. For the model, a continuous parameterization of the entropic coefficient over the SoC is advantageous. Therefore, a spline fit (MATLAB®) was applied based on the observations above. The data points from SoC 100 % to 20 % were selected from the discharging direction and at low SoCs from the charging direction excluding SoC 0 % for the spline fit. The spline fit is later illustrated in Figure 3.13.

In the thermal model, the **thermal material properties** – the density ρ , specific heat capacity c_p and the thermal conductivity λ – are also necessary. These are temperature and SoC dependent[286]. However, the evaluation of the SoC dependency is highly time consuming on material level and therefore not within the scope of this work. The thermal material properties were published for the “Kokam” in Queisser et al.[260], for the “Enertech” in Cloos et al.[243] and the “L 3.4” in Cloos et al.[244]. They were obtained at the TVT (KIT) with a measurement methodology developed by Oehler et al.[286].

From the individual materials of the active material, current collectors and separators, the **homogenized temperature dependent thermal material properties** can be calculated. For example, under the assumption of a series and parallel connection the thermal conductivity can be calculated[287]. The calculations are performed within a MATLAB® code written by Oliver Queisser at TVT (KIT).

3.2.3 Aging of Thermal and Electrical Properties

So far, the dependencies of the electrical parameters such as resistances and thermal parameters were only discussed at BoL. Over aging, not only the electrical and thermal parameters themselves can change but also their dependencies on for example SoC.

Pastor-Fernandez et al.[288] have proven, that the **SoC dependency of the resistances** change during cyclic aging and different time constants are affected to a different degree. The question remains if the interrelation of the SoC, T and SoH dependencies is significant. Again, the pulse resistance at 18 s over SoC is evaluated for all checkups for two aged “Enertech” cells. In Figure 3.12, this dependency is plotted for a cell aged at the equivalent aging temperature of 19 °C on the left and 45 °C on the right.

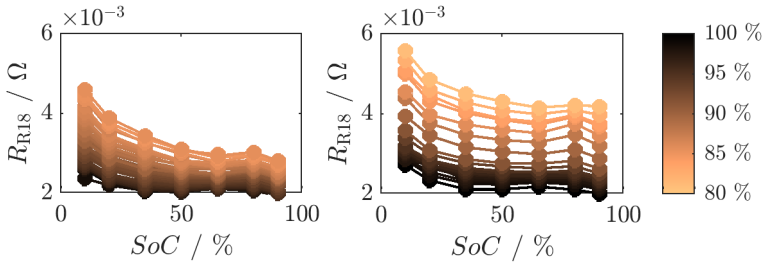


Figure 3.12: Evolution of SoC dependency of pulse ECM over aging of “Enertech” aged at 19 °C (left) and 45 °C (right).

Qualitatively, the SoC dependency of the resistance stays the same over the course of aging with a slight increase at lower SoCs. This is more pronounced for the lower aging temperature. This effect is not due to an SoC shift because the SoC was set with respect to the aged standard capacity. Potentially, this is related to increased degradation at lower SoCs[288], hence, loss of lithiated or delithiated active material[134]. Similarly, the temperature dependency of the resistances can change due to decreased Li^+ diffusion or reduced porosity and electrochemical reaction rate[289]. However, these effects require further analysis going beyond the scope of this work. Therefore, the aging of resistances ECMs is parameterized at an SoC of 50 % and checkup temperature of 25 °C.

It was reported in literature that the SoC dependency of the **entropic coefficient** alters with aging. The general trend was measured to be the same

before and after cycling[290,291]. The maximum entropic coefficient shifted from medium SoCs to higher SoCs[292]. Yun et al.[290] related the entropic coefficient to the intercalation state in the negative electrode, as this was dominant for degradation. They found the shift of the length of lithium intercalation (or SoC) to be due to the lost lithium over aging. The authors concluded the entropy coefficient to be independent of cell aging. Due to the limited number of investigations on this topic, it was checked for the “EnerTech”. The entropic coefficient over aging was evaluated based on the electrochemical characterization performed on a BoL “EnerTech” and a cell aged at a homogeneous temperature of 25 °C (25 °C *b* see Section 3.2.4). Comparing the fit of the BoL and EoL entropic coefficient in Figure 3.13, literature findings can be confirmed.

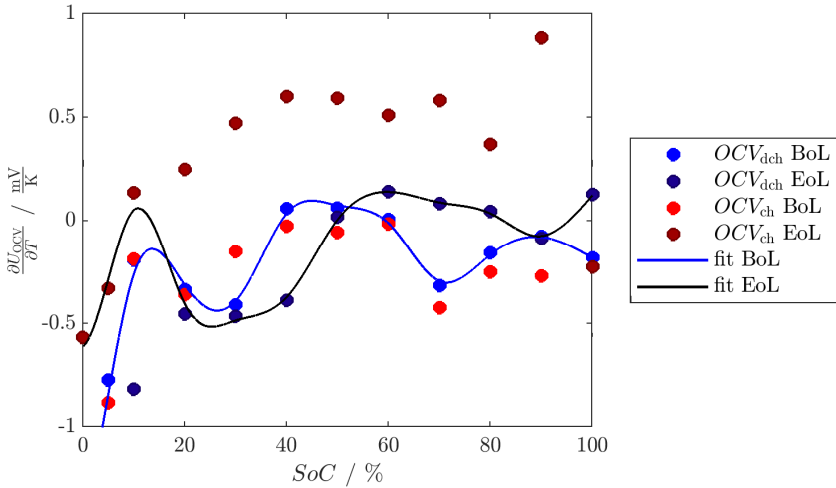


Figure 3.13: Entropy coefficient of the OCV (circle) measurements during electrochemical characterization for both charging (red) and discharging direction (blue) for the “EnerTech” cell. A cell at BoL (lighter color) is compared to a cell at EoL (darker color) aged at 25 °C (25 °C *b*) including a spline fit.

The maximum entropic coefficient is shifted to higher SoCs, indeed. This might also be related to the dominant degradation mode which will be discussed in the next chapter. Inexplicably, the entropic coefficient from the *OCV* measurement in charging direction is almost entirely positive and a lot higher than that of the discharging direction. This is not the case at BoL and it is unclear if that is a measurement artifact. Further investigations are necessary before a conclusive model on that behavior can be formulated. Therefore, the aging of the entropic coefficient will be neglected in this aging model.

The **thermal material properties age** as well. The thermal conductivity was found to reduce from 4 % to 23 %[293] and up to 40 %[294] of the initial state. While lithium plating does not affect the thermal conductivity strongly, electrolyte loss has an effect[294]. This is in line with the findings of Marconnet et al.[295] who found reduced thermal conductivity for increasing temperature. The reduction is significant and needs to be taken into account when discussing modeling results. So far, results are only available for the “Kokam” cell at EoL. Therefore, the data basis is not sufficient for model parameterization but could be of interest for improving the quality of the thermal aging model in further works.

3.2.4 Semi-Empirical Aging Model

Similar to the modeling of the electrical behavior, the aging of LIBs can be modeled from fully physics informed to fully empirical. Physically motivated aging functions usually represent changes in resistance and capacity as a function of stress factors as done by Schmalstieg et al.[296]. The focus of the model in this work is on the aging with inhomogeneous temperature. Therefore, the cyclic aging studies used for parameterization and validation were designed with care, keeping other stress factors than temperature constant.

Aging Model Simplifications: Stress Factors

Even when keeping the global electrical stress-factors constant during aging, this assumption is predicted to be false for cells with internal thermal gradients[42,227]. Li et al.[42] insisted that modelling the current dependency of the cyclic aging behavior is a necessity. Ignoring this current dependency led to an inability of reproducing experimental results with a forced thermal gradient. This influence seems so important because the current influences many aging mechanisms. Firstly, locally higher current densities, higher SoCs and lower temperatures favor lithium plating[111]. The SEI growth is also dependent on the current[100]. Furthermore, graphite exfoliation, loss of electrical contact and electrode particle cracking can be enhanced with increasing current load[52]. The difficulty is in the parameterization of the current dependency of the cyclic aging behavior. Current dependent aging data is not available for the investigated cells in this work and is not easily transferrable from literature values due to different aging behavior of different cell chemistries and electrode designs. Therefore, this dependency needs to be neglected in a first step. Furthermore, this aspect is likely to be less relevant for the main cell “Enertech” due its high C-rate tolerance.

The same is true for the stress-factor depth of discharge “DoD”. At the end of discharging with a thermal gradient, the overall cell resistance increases[28]. The lower cut-off voltage is reached earlier[239] because the lower temperature region of the cells with the highest resistivity needs to supply the highest current[42]. This also implies less accessible capacity because of a wide SoC distribution[43]. Since a lower DoD – and this does not imply shallow cycling or low mean SoCs – usually causes less severe aging[155] it might be necessary to parameterize and model this stress-factor.

All in all, the most important stress-factors for the aim of this work are the equivalent aging temperature T_{EAT} and the charge-throughput or *EFC*. They affect multiple parameters of the thermal-electrical model. As discussed in the previous chapters not all aging dependencies are significant. The aging

of thermal material properties, entropic coefficient, SoC dependency of ECM parameters are neglected in a first step. The focus is put on the energy and performance – or more specifically the capacity and impedance. An aging function describing the changes of these variables as a function of the stress factors needs to be set up. To do so, knowledge of the relation of the dominant degradation modes and aging mechanisms is necessary. This is done by Cloos et al.[2] on the basis of a “Enertech” cyclic aging study at homogeneous aging temperatures between 4 °C and 48 °C with the exact equivalent aging temperatures given in Table 1 A in the Appendix. Afterwards, the semi-empirical aging model can be derived. Even though it is only shown for the “Enertech”, the model can also be applied on the “Kokam”.

Understanding the Temperature Dependent Aging Behavior

The relative nominal capacity over cycling time t in days d in Figure 3.14 (a) on page 65 revealed two distinct changes in the aging trajectory. These were indicated with dotted and stroked vertical lines in the figure identified by the Double-Bacon Watts model. Firstly, a decelerating capacity loss with slightly different slopes for the aging temperature were seen. Then, the aging trajectories followed a linear function before a capacity knee could be observed for high aging temperatures above 45 °C. [2]

The three aging trajectory regimes were only obvious for these higher aging temperatures. Lower aging temperatures of 3 °C and 17 °C resulted in a lower capacity loss. A transition from decelerating to linear regime could also be seen in an increase in LAM_{PE} being swiftly followed by an increase in LLI (Figure 3.14 (b, c)). This suggested a correlation between positive electrode processes and an increase in LLI which is the dominant degradation mode for this cell while LAM_{NE} being negligible (Figure 3.14 (d)). LLI being dominant for NMC-LMO graphite cells is in line with literature[210,297]. [2]

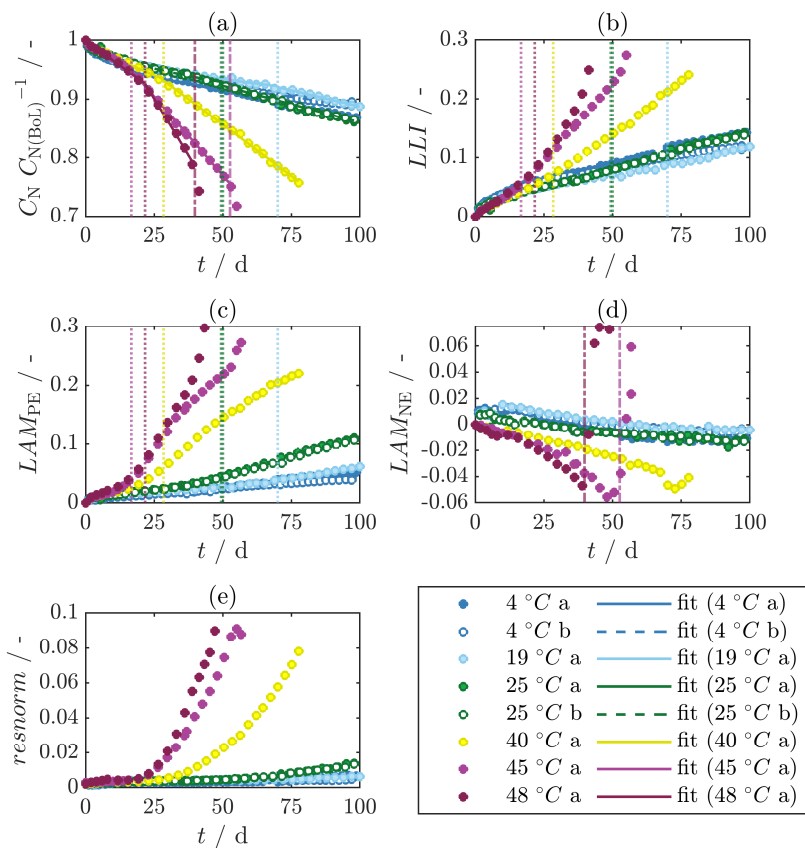


Figure 3.14: Degradation mode analysis and capacity loss over time in days with fitted aging function for homogeneous aging temperatures from 4 °C (blue) to 48 °C (dark violet) for the cells of the "EnerTech" study (Adapted with permission under the terms of Creative Commons Attribution 4.0 License CC BY.[2] Copyright 2024, The Authors. Published on behalf of The Electrochemical Society by IOP Publishing Limited.).

SEM pictures of aged negative and positive electrode particles showed visible alterations in comparison to BoL electrode particles (Figure 3.15). [2]

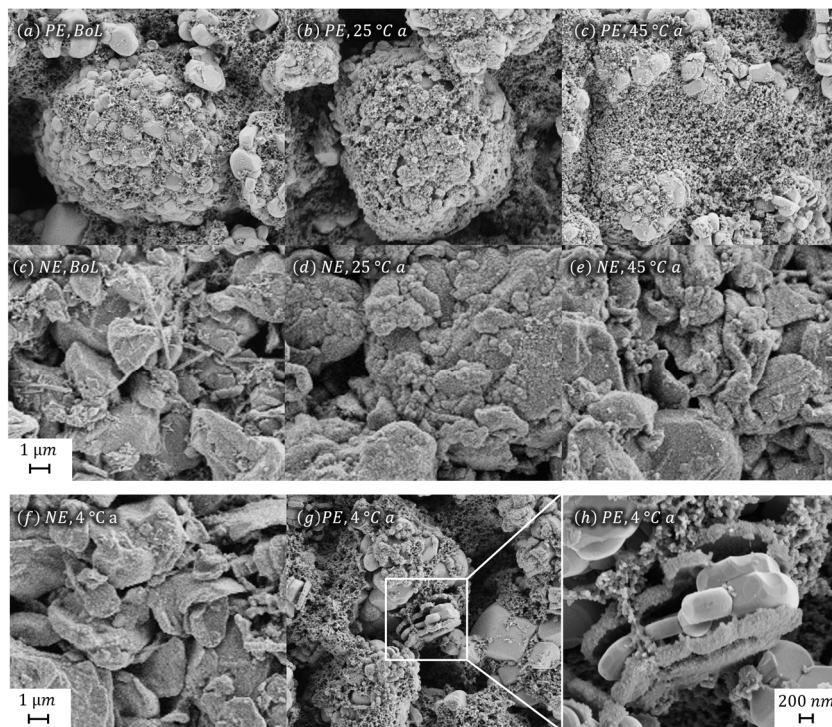


Figure 3.15: SEM pictures of aged positive (b, c, g, h) and negative (d, e, f) electrodes of the “Enertech” in comparison to BoL (a, c) (Reproduced with permission under the terms of Creative Commons Attribution 4.0 License CC BY.[2] Copyright 2024, The Authors. Published on behalf of The Electrochemical Society by IOP Publishing Limited.).

The aged positive electrode particles showed a cover layer formation which can be seen in Figure 3.15 (b) and with a higher magnification in Figure 3.15 (h) in comparison to the state at BoL in Figure 3.15 (a). At high aging temperatures of 45 °C, areas of particle pulverization were observed in

Figure 3.15 (c). In a literature study on a NMC-LMO-NCA blend positive electrode, stressed and microcracked NMC particles were already found for voltages of 4.05 V[87,88]. For the negative electrode, visible changes were only observed for medium (25 °C) to higher aging temperatures (Figure 3.15 (d, e)) in comparison to the state at BoL in Figure 3.15 (c). At lower aging temperatures of 4 °C only very mild changes to the graphite particles were observed in Figure 3.15 (f). These findings were related to increased SEI growth with increasing aging temperature for the investigated “Enertech”. [2]

The findings could be correlated to an additional phenomenon that was seen for higher aging temperatures of 45 °C in Figure 3.16.

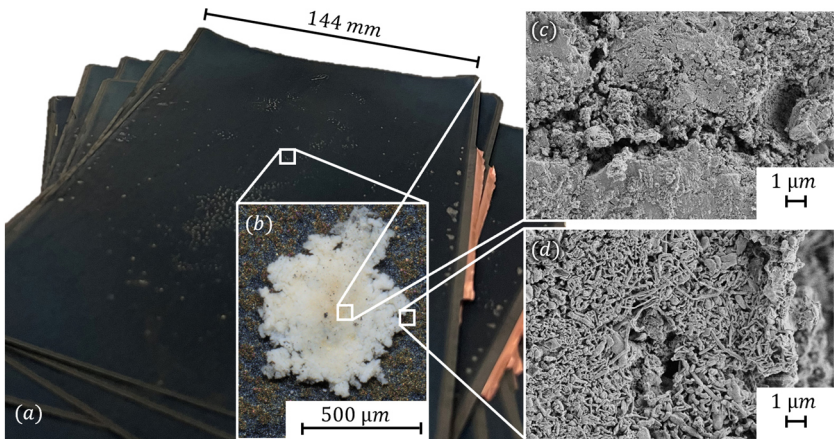


Figure 3.16: (a) Picture of the negative electrode sheets of a “Enertech” aged at 45°C and (b) light microscopy and (c, d) SEM pictures of depositions (Reproduced with permission under the terms of Creative Commons Attribution 4.0 License CC BY.[298] Copyright 2024, The Authors. Published on behalf of The Electrochemical Society by IOP Publishing Limited.).

White depositions formed on the negative electrode with contents of lithium, oxygen, phosphorous and fluorine as well as transition metals. The SEI growth can be enhanced by transition metal dissolution from the positive electrode[93,94]. The shape of the depositions (Figure 3.16 (b)) as well as the mossy structure at the edges of the depositions (Figure 3.16 (d)) led to the assumption of mossy lithium dendrite growth[299] which reacted to dead lithium[119]. The increased charge transfer due to increased SEI growth were a probable reason for the depositions being correlated to a capacity knee[199]. [2]

Setting Up a Semi-Empirical Aging Model

The global behavior of the “Enertech” cell over aging was ruled by LLI. A significant increase LAM_{PE} was observed as well. These losses originated from aging mechanisms on the negative and positive electrode and their interaction. In order to model the global behavior accurately, both negative and positive electrode aging mechanisms need to be taken into account. To this date, positive electrode degradation models were not in focus of literature. Kindermann et al.[300], for example, simplified the positive electrode degradation to positive electrode dissolution to be proportional to the maximum lithium-concentration. Still, the processes are not fully understood[301]. Therefore, the effects of the positive electrode degradation on the active material loss and resistance increase will be parameterized fully empirical in this work.

The focus of the aging model in this work, should be on the aging mechanisms which were dominant for the aging trajectory of the “Enertech” and are expected to be important for aging with thermal gradients (see chapter 2.3.4). Following from this, SEI growth and lithium plating causing LLI need to be modeled. What is more, lithium plating was found important in literature for aging with inhomogeneous temperature distribution[48,227]. The possibility of lithium plating can be predicted by the negative electrode potential. The thermodynamical limit of lithium plating at 0 V[109,112] serves as a limit. For the “Enertech”, lithium plating was also attributed to

the capacity knee[2]. While the possibility of such a capacity knee can be predicted with this approach, the modeling of the actual capacity knee would require further work which is not within the scope of this work. An overview of the aging modeling approach of this work is shown in Figure 3.17.

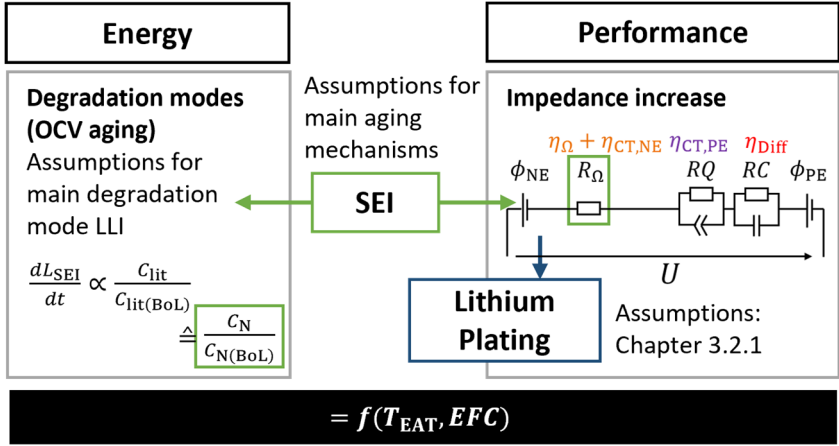


Figure 3.17: Aging modeling approach with focus on LLI and SEI growth.

In this work, the SEI growth is modeled with a reduced order approach[302] based on the works of Kolzenberg et al.[100,208]. SEI growth leads to changes in the OCV and the ECMs. More specifically, it causes increased LLI or decrease of capacity of available lithium $\frac{C_{lit}}{C_{lit}(BoL)}$ and increased SEI resistance η_{SEI} . The SEI growth was divided in three regimes in the SEI theory of Kolzenberg et al.[100]. In the first regime, the apparent SEI thickness L_{SEI} is well below the critical diffusion thickness. Here, the growth is reaction limited. This is only true for very thin SEI which will be neglected due to the application on commercial cells with already formed initial SEI. In the second regime, the apparent SEI thickness is between the critical diffusion and migration thickness. The SEI growth is diffusion limited and proportional to

square-root of time. For a SEI thicknesses larger than the critical migration thickness L_{mig} , the SEI growth is linear with time during charging. The process is limited by electron migration through the SEI. The SEI growth is completely suppressed during discharging in this regime. [100]

The SEI model of Kolzenberg et al.[100] depends on many parameters which need to be simplified. The parameterization will be done with aging data from medium to higher aging temperatures where SEI growth is kinetically favored[11]. The optimum aging temperature for the “EnerTech” was found in the region of 19 °C which was similarly low in an aging study on plug-in hybrid electric vehicle NMC cells[14]. Therefore, the aging temperatures of 19 °C to 48 °C were used for parameterization. SEI is a main contributor of increasing LLI which was found dominant for the “EnerTech”. That leads to the assumption that the relative capacity decrease mirrors the capacity of available lithium decrease $\frac{C_{\text{lit}}}{C_{\text{lit(BoL)}}} \triangleq \frac{C_{\text{N}}}{C_{\text{N(BoL)}}}$. Furthermore, the available lithium $\frac{C_{\text{lit}}}{C_{\text{lit(BoL)}}}$ is related to the change of SEI thickness $\frac{dL_{\text{SEI}}}{dt}$ in the model.

With these assumptions, the aging functions can be derived. The aging function of the capacity loss – representing LLI and the apparent SEI thickness – is parameterized as a function of charge-throughput and equivalent aging temperature. Thereby, the charge through-put is normed with the equivalent full cycles (EFC). In this work, EFC is defined as the sum of cycled capacity in both discharging and charging direction divided by two times the nominal capacity at BoL. Function (3.7) represents the diffusion limited SEI growth below the critical migration thickness in the linear regime.

$$\frac{C_{\text{N}}}{C_{\text{N(BoL)}}} = 1 - r_{\text{pow}} \cdot \text{EFC}^{\alpha_{\text{pow}}} ; \frac{C_{\text{N}}}{C_{\text{N(BoL)}}} \leq \left(\frac{C_{\text{N}}}{C_{\text{N(BoL)}}} \right)_{L_{\text{mig}}} \quad (3.7)$$

This critical migration thickness is represented by a relative nominal capacity threshold $\left(\frac{C_{\text{N}}}{C_{\text{N(BoL)}}} \right)_{L_{\text{mig}}}$. Even though, in theory, diffusion limited SEI growth follows a square root dependency it is rarely justified for real life aging data

on LIB[204]. For the “Enertech”, a square-root dependency was only seen for lower to medium (25 °C) aging temperatures in the first capacity loss regime. This dependency was analyzed with fitting a power function over a sliding window of 15 days to the relative nominal capacity as shown in Figure 3.18[2].

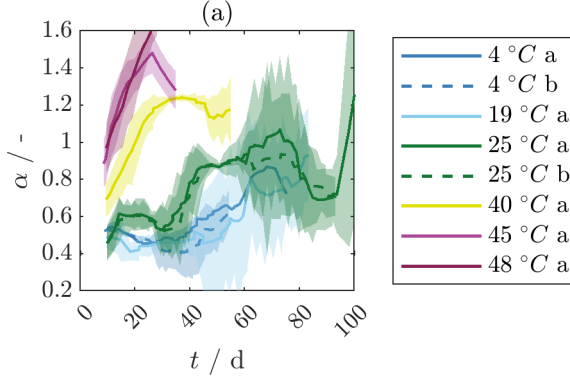


Figure 3.18: Evaluation of the exponent α_{pow} of a power function over a sliding window of the relative nominal capacity over time in days (Reproduced with permission under the terms of Creative Commons Attribution 4.0 License CC BY.[298] Copyright 2024, The Authors. Published on behalf of The Electrochemical Society by IOP Publishing Limited.).

Higher aging temperatures showed an exponent above 0.7 which was previously seen for transition metal induced SEI growth[84]. Consequently, the capacity loss function in the first regime is dependent on the slope r_{pow} and the exponent α_{pow} . The second capacity loss regime follows a linear function with slope r_{lin} starting from the relative nominal capacity threshold (equation (3.8)).

$$\begin{aligned} \frac{c_N}{c_{N(\text{BoL})}} &= \left(\frac{c_N}{c_{N(\text{BoL})}} \right)_{L_{\text{mig}}} - r_{\text{lin}} \cdot (EFC - EFC_{L_{\text{mig}}}); \\ \frac{c_N}{c_{N(\text{BoL})}} &> \left(\frac{c_N}{c_{N(\text{BoL})}} \right)_{L_{\text{mig}}} \end{aligned} \quad (3.8)$$

In a first step, this relative nominal capacity threshold representing the critical migration thickness needs to be identified. It marks the transition from the power function to the linear function. For the “Enertech” this transition was also seen in LLI and LAM_{PE} which was correlated to increased SEI and a positive electrode cross-talk[2]. It could also be related to increased solvent consumption which was found to result in a capacity loss acceleration by Li et al.[101]. This transition was identified with a Double-Bacon-Watts model[264] (Figure 3.14). For medium to higher aging temperatures, this transition was found at a mean of 94 % SoH for the “Enertech” and “Kokam”.

In a second step, the equivalent aging temperature dependency is identified for the parameters of the capacity loss aging function r_{pow} , α_{pow} and η_{lin} . The Arrhenius plots in Figure 3.19 (a-c) on page 73 confirm the predicted Arrhenius activation for medium to higher equivalent aging temperatures in Kelvin on the example of the “Enertech” aging study. The errorbars mark the 95 % CI of the parameters.

A fit with equation (3.9) was performed to obtain the Arrhenius activation.

$$r_{pow} = \exp\left(A + B \cdot \frac{1}{T_{EAT}}\right) \quad (3.9)$$

In a third step, the OCV aging which is determined by the degradation modes needs to be fully parameterized. Therefore, the capacity loss and the alignment parameters α_{PE} , α_{NE} , β_{PE} and β_{NE} are of interest. Equation (3.10) was deduced from Schmitt et al.[131] describing the capacity of available lithium C_{lit} with these alignment parameters.

$$C_{lit} = (-\beta_{NE} + \alpha_{PE} + \beta_{PE}) \cdot C_N \quad (3.10)$$

The loss of active material of the negative electrode was found to be negligible for the “Enertech” cell. With an empirical parameterization of the relative change of the positive electrode alignment factor α_{PE} and the

relative capacity loss $\frac{c_N}{c_{N(\text{BoL})}}$ from the SEI model, all parameters can be calculated.

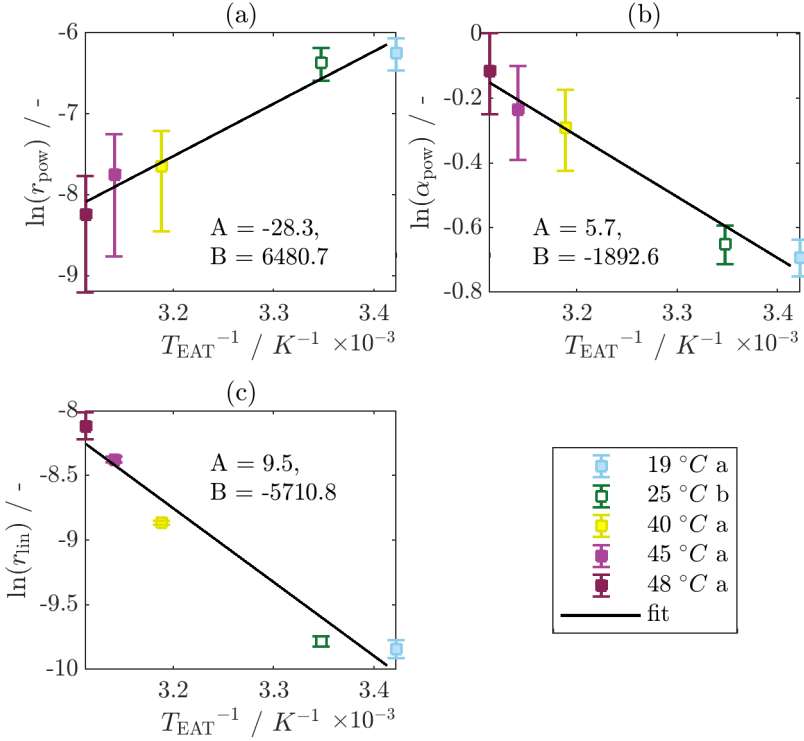


Figure 3.19: Arrhenius plot of the parameters of the capacity loss aging function derived from the “Enertech” aging study[2].

The relative change of the positive electrode alignment factor is parameterized as a function of the equivalent aging temperature and EFC. Thereby, the equivalent aging temperature dependency is derived from the double Arrhenius function presented by Werner et al.[17]. The start values for the fitting parameters A , B , C and D were also taken from the results of Werner

et al.[17]. The exponent of the EFC dependency was defined temperature dependent resulting in equation (3.11).

$$\frac{\alpha_{PE}}{\alpha_{PE(BoL)}} = 1 - (A \cdot e^{-B \cdot T_{EAT}} + C \cdot e^{D \cdot T_{EAT}}) \cdot EFC^{E \cdot T_{EAT} + F} \quad (3.11)$$

The fit in Figure 3.20 was performed with the *Levenberg-Marquardt* method in MATLAB® and is implemented as a look up table in the model.

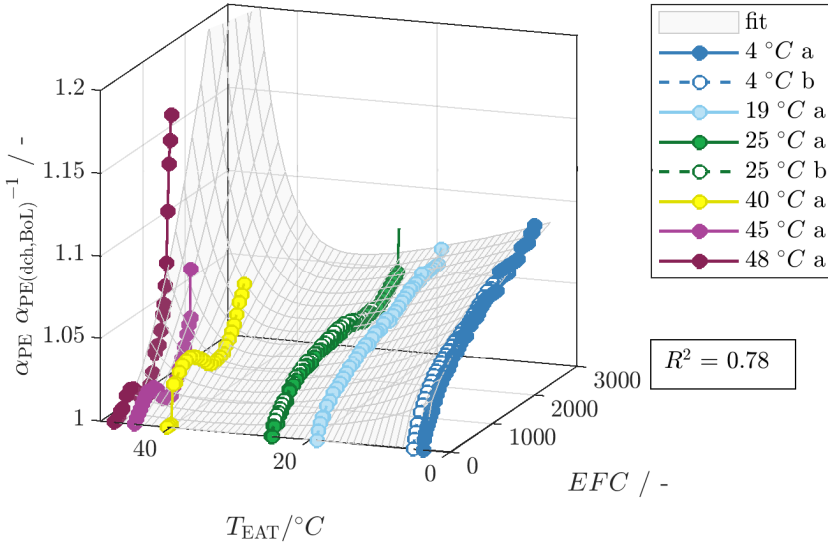


Figure 3.20: Empirical fit of equivalent aging temperature and EFC dependency of relative alignment parameter α_{PE} on “Enertech” aging study[2].

Now, the **impedance increase** needs to be described. This resistance increase is included as a relative aging factor multiplied with the BoL value which is interpolated between temperature and SoC. The relative aging factor varies for each element of the ECM. Each element was attributed to different electrode processes which age differently (see chapter 3.2.1).

The ohmic resistance in the combined ECM describes the negative electrode including the SEI resistance and should be linked to the SEI model. The SEI model of O’Kane et al.[303] in the PyBAMM model describes the overpotential η_{SEI} as a linear dependence of the SEI thickness. The SEI thickness is represented by the relative capacity loss in this model. A plot of relative capacity loss versus relative ohmic resistance increase reveals a linear dependency, indeed (Figure 3.21).

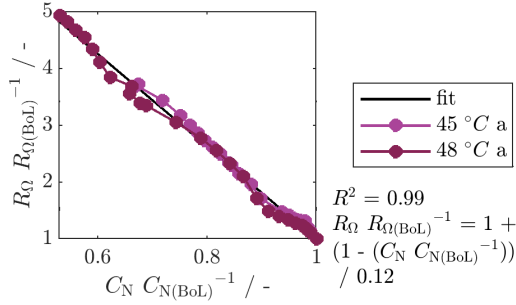


Figure 3.21: Dependency of relative capacity and relative ohmic resistance from combined ECM on the example of high aging temperature of 45 °C and 48 °C with linear fit on “Enertech” aging study[2].

A fit with equation (3.12) could be performed.

$$\frac{R_{\Omega}}{R_{\Omega(BoL)}} = 1 + \frac{\left(1 - \frac{C_N}{C_{N(BoL)}}\right)}{G} \quad (3.12)$$

However, this dependency which is described by the fit parameter G is temperature dependent. The relation can be described with the same Arrhenius dependency in equation (3.9) and is plotted in Figure 3.22.

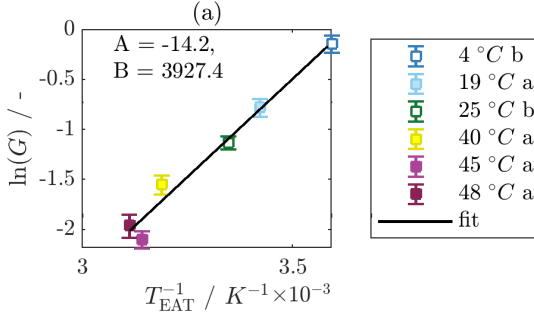


Figure 3.22: Arrhenius fit of slope G representing the relation of relative capacity loss and ohmic resistance from combined ECM increase on “Enertech” aging study[2].

The ECM elements describing the positive electrode charge transfer and diffusion processes are parameterized empirically. Specifically, the RQ element representing the positive electrode charge transfer shows only slight dependence on the equivalent aging temperature (Figure 3.23 on page 77). This confirms the analysis of SEM pictures in Figure 3.15 where all positive electrode particles showed similar changes. Only higher aging temperatures led to larger changes[2]. This means that the positive electrode charge transfer is mostly related to the amount of performed cycles. Therefore, only the EFC dependency is described with a power function as indicated in Figure 3.23. The presented functions in Figure 3.23 are only valid in the depicted EFC interval. As always in this chapter, the changes of the parameters are related to their initial state at BoL.

The equivalent aging temperature is implemented as a double Arrhenius to describe the diffusion RC element using start parameters of Werner et al.[17] (equation 3.17).

$$\frac{R_{RC}}{R_{RC(BoL)}} = 1 - (A \cdot e^{-B \cdot T_{EAT}} + C \cdot e^{D \cdot T_{EAT}}) \cdot EFC^E \quad (3.13)$$

The resistor and capacitor of the RC element as implemented in the model are presented in Figure 3.24 on page 78.

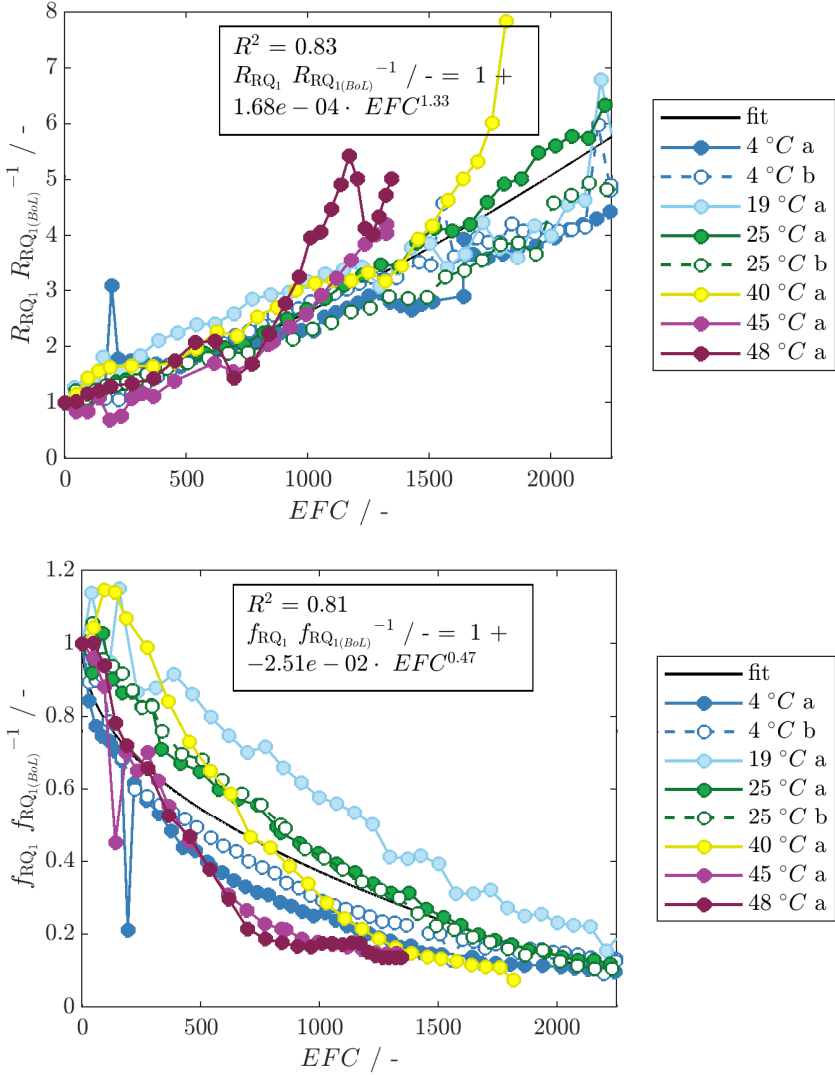


Figure 3.23: Empirical fit of relative resistor R_{RQ} (top) and capacitor C_{RQ} (bottom) (n=1) of positive electrode charge transfer RQ element as a function of EFC on "Ener-tech" aging study[2].

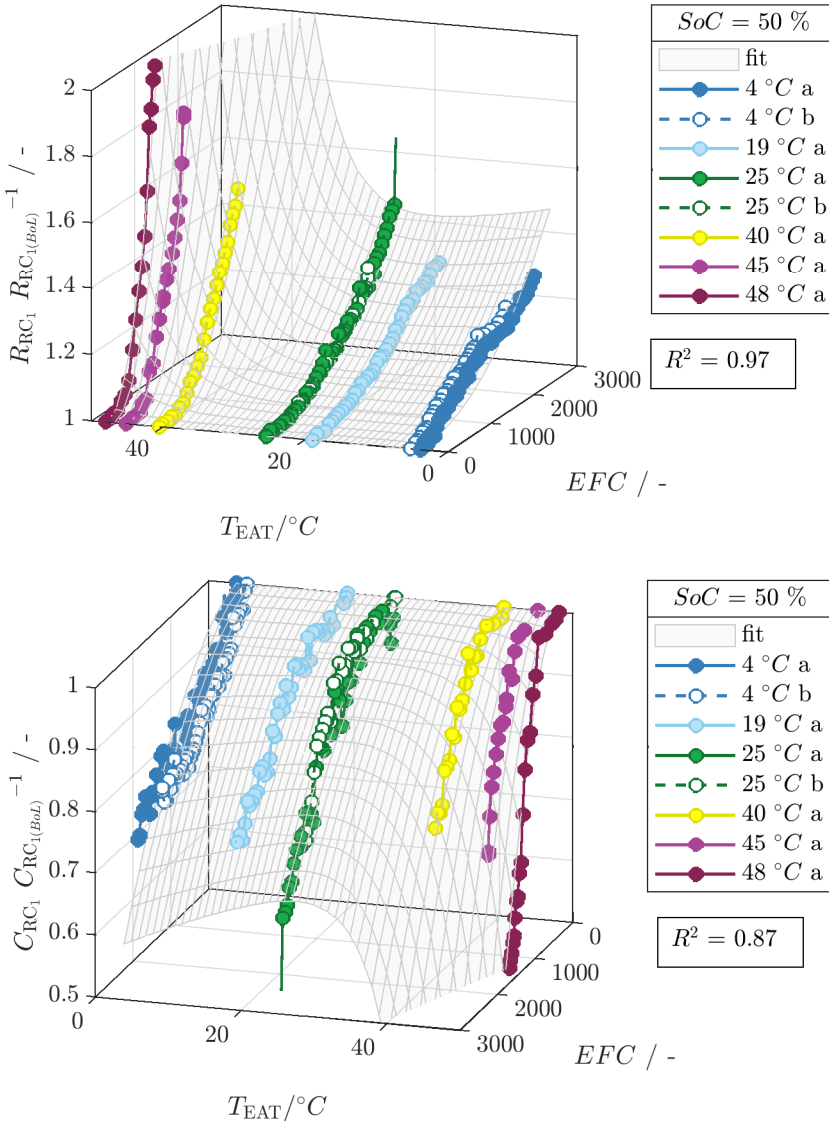


Figure 3.24: Empirical fit of relative resistance and capacitor of diffusive RC element as a function of the equivalent aging temperature and EFC on “EnerTech” aging study[2].

Apart from the development and parameterization of the aging model, the spatial and temporal discretization are of interest as they are decisive for the computational effort. An automatic spatial discretization of the cell geometry and an adaptive time stepping of the charging and discharging cycles was already implemented in the thermal-electrical model. For the aging model, an aging time stepping was implemented to reduce computational effort. Similar to the aging tests, a full discharge and charge cycle is calculated after a defined number of cycles. This is under the assumption that the individual cell parameters do not change during this number of cycles. Therefore, in the beginning, every 5th full cycle is calculated until 10 EFC. Then, every 200th cycle is calculated. If a segment approaches the relative nominal capacity threshold, the EFC stepping is reduced to 25 cycles again. Specifically, this is done from 0.95 to 0.94 relative nominal capacity of each segment.

3.2.5 Validation

Model validation is a necessity. Here, the semi-empirical aging model including the thermal-electrical model is validated. In this way, the aging time discretization as well as the time stepping and spatial discretization is checked. The applicability of the modeling assumptions for thermal-electrical behavior was preliminarily checked and can be found in the Appendix “Preliminary Validation of Thermal-Electrical Model”.

To add complexity to the aging model validation, the thermal boundary condition was chosen with respect to the relevant “Enertech” aging studies. An inhomogeneous temperature condition in-plane from 40 °C to 10 °C was applied with a Dirichlet boundary condition in y-direction. Finally, the spatial segmentation was chosen as an optimum compromise of sufficient accuracy and the reduction of simulation time. The y-direction of the cell was divided in 7 segments while the z-direction was splitted in 6 segments.

Here, the voltage curves serve as a validation baseline in Figure 3.25. Further results on the relative capacity loss are shown in the discussion in chapter 4.2.

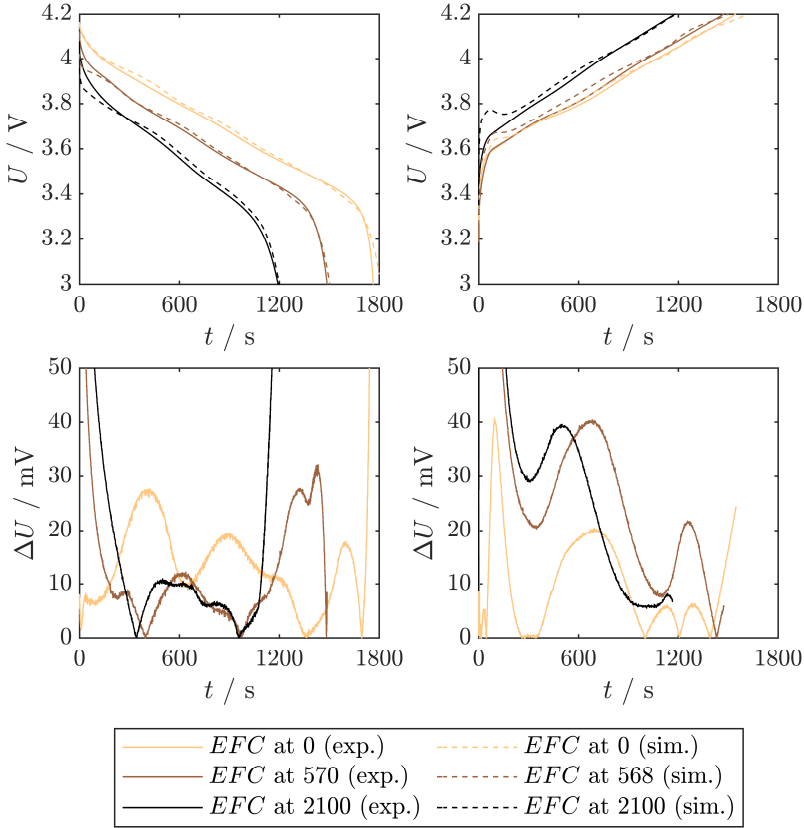


Figure 3.25: Voltage U during 2C-CC discharging (left) and charging (right) of I_y 10 °C 40 °C “Enertech” at different EFCs, experiment (exp.) from “Ener-tech” aging study[1] and simulation (sim.) as well as error ΔU of simulation (bottom).

The voltage curves are compared at similar EFC (± 10 EFC) of experiment (exp.) and simulation (sim.) with their difference ΔU . The experimental voltage curves presented here were the second full cycle after the checkup. Knowledge of the exact aging states is only available during the checkup in the experiment. Since the checkup interval of the experiment did not exactly match the simulation discretization of the aging model, slight differences in EFC arise.

Overall, the simulated voltage signal is in good accordance with the experiment. The end of discharging and charging are predicted with high accuracy even at lower SoH. Solely the overvoltages at the beginning of discharging and charging are overestimated during aging. In this SoC region the error exceeds the 30 mV range. This could be due to difficulty in parameterization at high and low SoC, the electrode potential splitting and neglecting changes in the time constants of the high frequency ECM elements. Overall, the results suggest that not only the aging modeling approach but also the time discretization were chosen with sufficient accuracy.

4 Discussion – Local and Global Aging Behavior

The developed experimental and simulative methods are now used to examine the local and global aging behavior of LIB cycled with complex thermal boundary conditions. Firstly, the effect of inhomogeneous steady-state temperature is analyzed and put into context of contradicting results in literature.

4.1 Experiments on In-Plane Versus Through-Plane Inhomogeneous Steady-State Temperature Effects

An inhomogeneous temperature field during cyclic aging of LIB can cause a positive feedback mechanism on the aging acceleration[42]. In another study, cells exposed to an inhomogeneous temperature field showed a comparable aging rate to the cell aged at the equivalent aging temperature. Furthermore, differences between the capacity loss with in-plane and through-plane thermal gradients are possible[227]. Cloos and Wetzel[1] performed additional experimental investigations to analyze the cyclic aging behavior with in-plane and through-plane thermal gradients on the “Ener-tech”. The homogeneous steady-state aging temperatures from Cloos et al.[2] served as reference. The comparison is made on the basis of the equivalent aging temperature T_{EAT} as explained in chapter 3.1.1. In this chapter, the results of Cloos and Wetzel[1] are summarized (highlighted with corresponding reference at the end of the paragraphs) and supplementary analysis results are shown.

The **relative nominal capacity** was plotted over EFC in Figure 4.1 (a).

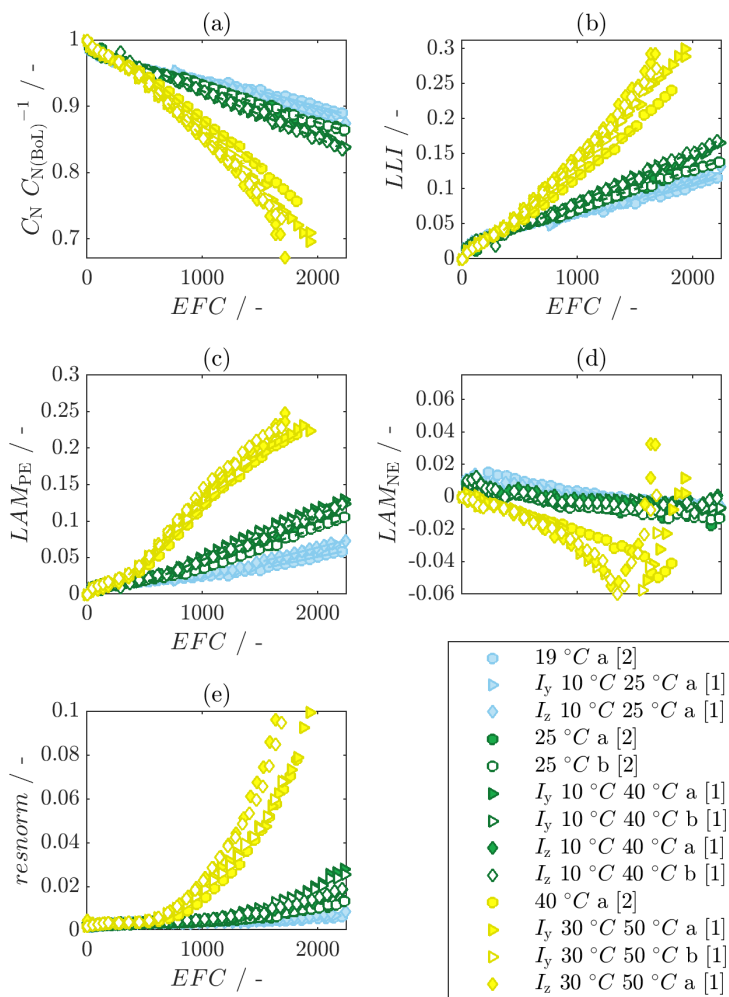


Figure 4.1: (a) Relative capacity loss over EFC; Quantitative change of degradation modes over EFC (b) LLI , (c) LAM_{PE} , (d) LAM_{NE} , (e) Squared norm of residuals. (Adapted with permission under the terms of Creative Commons Attribution 4.0 License CC BY.[1] Copyright 2025, The Authors. Energy Technology published by Wiley-VCH GmbH and with permission under the terms of Creative Commons Attribution 4.0 License CC BY.[2] Copyright 2024, The Authors. Published on behalf of The Electrochemical Society by IOP Publishing Limited.)

The capacity loss trajectories for higher (40 °C – yellow), medium (25 °C – green) and lower (17.5 °C / 19 °C – light blue) aging temperatures were qualitatively comparable between inhomogeneous steady-state (triangles and diamonds) and homogeneous steady-state (circles) thermal boundary conditions. Consequently, the use of the concept of equivalent aging temperature proved to be appropriate. Still, in the linear capacity loss regime, an acceleration was observed for all inhomogeneous steady-state temperature aging conditions in comparison to their reference. Also, at higher equivalent aging temperatures (yellow), a slight difference in the linear capacity loss slope was observed between in-plane and through-plane thermal gradients. This was apparent for the cells I_z 30 °C 50 °C a and I_y 30 °C 50 °C a which were cycled until the capacity knee. The knee onset of the through-plane thermal gradient I_z 30 °C 50 °C a appeared earlier than that of the in-plane thermal gradient I_y 30 °C 50 °C a . [1]

This **capacity loss acceleration** was quantitatively analyzed for the linear aging trajectories. The acceleration (A_{II}) of the linear slope r_{lin} of the capacity loss with inhomogeneous steady-state (I) in comparison to the reference (ref) temperature condition is calculated using Eq. (4.1).

$$A_{II} = \frac{|r_{lin,I} - r_{lin,ref}|}{|r_{lin,ref}|} \quad (4.1)$$

This linear slope was obtained from a fitting procedure presented by Cloos et al.[2]. The uncertainty of the fit was assumed to highlight the uncertainty of the individual checkup measurements. Half of the 95 % confidence interval of the fit parameters was used as a measure of uncertainty. This uncertainty propagates into the calculation of the acceleration factor A_{II} (procedure according to type B GUM [304]). In case of reproducibility measurements, the average calculation was directly inserted in Eq. (4.1). This analysis revealed a high reliability of the reproducibility tests. As a worst-case assessment, the highest difference between two reproducibility tests was between I_z 10 °C 40 °C a and I_z 10 °C 40 °C b . The difference still lied within the combined standard uncertainty of 4 %. The uncertainty calcula-

tion also revealed a high uncertainty for the lower tested aging temperatures. For this reasons they were not discussed in more detail. [1]

The results of the acceleration analysis are shown in Table 4.1.

Table 4.1: Linear capacity loss acceleration analysis of inhomogeneous steady-state thermal boundary conditions. [1]

Reference	Inhomogeneous thermal boundary condition	$A_{II} / \% [1]$
25 °C <i>a</i> 25 °C <i>b</i>	I_y 10 °C 40 °C <i>a</i> I_y 10 °C 40 °C <i>b</i>	$25 \pm 4 \%$
25 °C <i>a</i> 25 °C <i>b</i>	I_z 10 °C 40 °C <i>a</i> I_z 10 °C 40 °C <i>b</i>	$26 \pm 4 \%$
40 °C <i>a</i>	I_y 30 °C 50 °C <i>a</i> I_y 30 °C 50 °C <i>b</i>	$8 \pm 3 \%$
40 °C <i>a</i>	I_z 30 °C 50 °C <i>a</i> I_z 30 °C 50 °C <i>b</i>	$19 \pm 3 \%$

Both in-plane and through-plane inhomogeneous thermal boundary conditions from 10 °C to 40 °C accelerated the capacity loss in the linear regime by $25 \% \pm 4 \%$ in comparison to the reference. This is comparable to the measured acceleration by Werner et al.[17] with 26 % for an in-plane thermal gradient from 0 °C to 50 °C. The calculated aging acceleration by increasing the overall temperature from 25 °C to 40 °C was still 6 times larger. Furthermore, only at higher temperatures, an increased capacity loss acceleration for through-plane thermal gradients in comparison to in-plane thermal gradients could be confirmed. While the in-plane thermal gradient accelerated the capacity loss little ($8 \pm 3 \%$), a through-plane thermal gradient caused a capacity loss acceleration of $19 \pm 3 \%$. [1]

It should be noted that the differences in acceleration for medium and higher temperatures could not be directly compared. While the temperature difference at medium temperatures was 30 K, it was only 20 K at higher temperatures. Different magnitudes of the temperature gradient most likely have different effects[43].

The analysis of **degradation modes** over EFC is shown in Figure 4.1 (b-d) on page 84. The analysis was performed with the same method developed for the homogeneous reference cases[2] shown in chapter 3.1.2. The trends of the references transfer to the inhomogenous steady-state thermal boundary conditions. Overall, LLI mirrors the behavior of the capacity loss. The differences in LAM_{PE} for inhomogenous steady-state versus homogeneous steady-state are even less clear than for LLI and relative capacity loss. Investigating this further, the slopes of the degradation modes in the linear regime are compared for different equivalent aging temperatures in an Arrhenius plot in Figure 4.2. The data presented in Figure 4.2 was evaluated over time in days instead of EFC as suggested by Waldmann et al.[11] for Arrhenius plots.

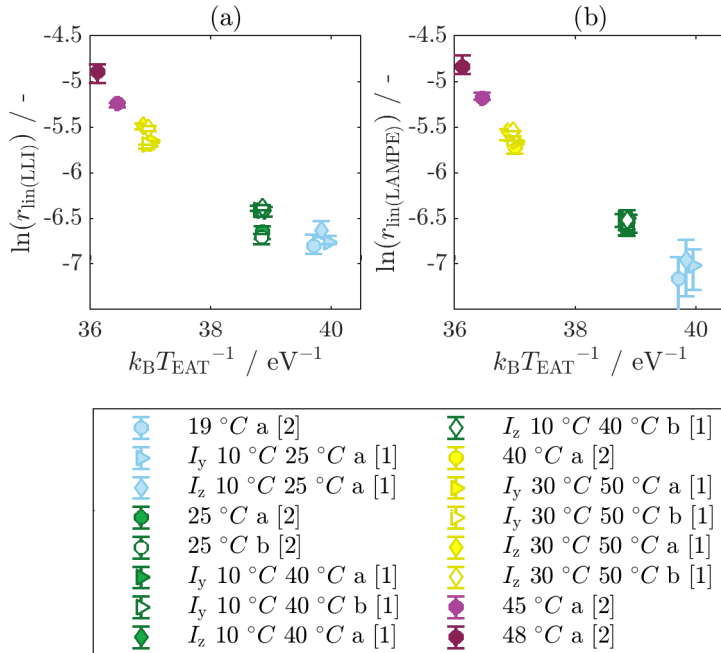


Figure 4.2: Arrhenius plots of linear region of quantitative degradation modes (a) LLI and (b) LAM_{PE} (Evaluation is based on “Enertech” aging studies[1,2]). Error bars represent 95 % CI of fitting parameter.

The Arrhenius plot of the linear slope of LLI (Figure 4.2 (a)) mirrors the acceleration for the capacity loss acceleration in Table 4.1. Different trends can be observed for LAM_{PE} in Figure 4.2 (b). The confidence intervals of the fitted slopes are overlapping for thermal gradient and reference temperature condition at the equivalent aging temperature level (light blue, green and yellow). This means that the processes causing LAM_{PE} are not accelerated for thermal gradient temperature condition. However, the trajectories of LAM_{PE} in Figure 4.1 (d) are not completely overlapping. This points in the direction of an earlier onset of the linear regime of LAM_{PE} of the inhomogeneous steady-state in comparison to homogeneous steady-state boundary conditions.

LAM_{PE} can be put into context of other measurable positive electrode aging mechanisms. Impedance data can be analyzed as well, even though, degradation modes and impedance do not always have the same trends. In chapter 3.2.4, the RQ element representing positive electrode charge transfer of the “EnerTech” was shown to be insensitive to the aging temperature. More so, it could be correlated to the cycling numbers and the time at high and low voltages. The cycle numbers are not drastically different between thermal gradient and reference temperature conditions. However, the predicted reduced DoD of the cells with thermal gradients could have an attenuating effect on the positive electrode degradation. Differences on particle level might be visible as well.

In Figure 4.3, in **post-mortem analysis**, sections of positive electrode particles closer to the lower (left) and higher (right) aging temperature boundary conditions are presented for in-plane and through-plane thermal gradients from 10°C to 40 °C.

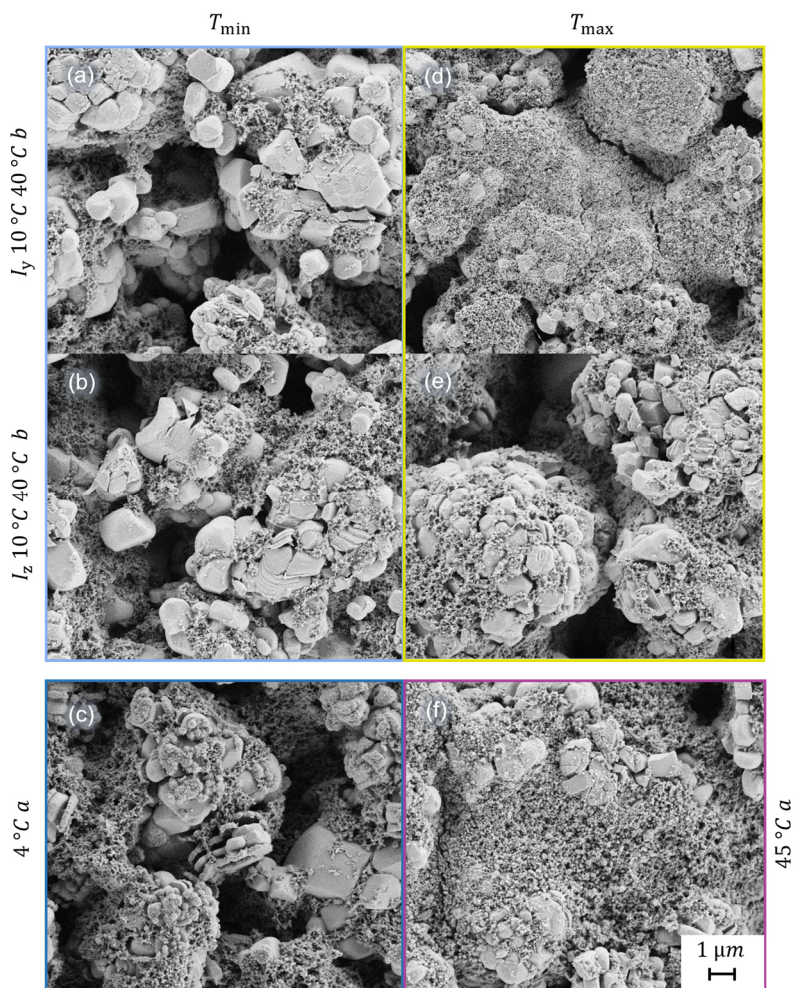


Figure 4.3: Pictures of SEM on aged "Enertech" positive electrodes aged at lower (left) and higher (right) local aging temperatures than 25 °C; Comparison of homogeneous steady-state thermal boundary conditions (bottom) to inhomogeneous steady-state thermal boundary conditions (top) ((c, f) Reproduced with permission under the terms of Creative Commons Attribution 4.0 License CC BY.[1] Copyright 2025, The Authors. Energy Technology published by Wiley-VCH GmbH.).

A comparison is made with homogeneous steady-state thermal boundary condition at 4 °C and 45 °C (bottom). The positive electrodes show many expected aging mechanisms. They vary from primary and secondary particle cracking[45,88,305,306] to particle pulverization[90]. The latter was only observed in some regions of higher local temperatures Figure 4.3 (d). No clear differences are observed for the other electrodes aged at an inhomogeneous thermal boundary condition in Figure 4.3 (a, b, d, e). Already at BoL, some particle cracking was observed[2].

Cracking is particularly well observable for the NMC secondary particles[74]. This can be nicely seen in Figure 4.3 (e). It was suggested that particle cracking is more of a symptom of surface reactivity of the positive electrode electrolyte interface. Reducing this surface reactivity and oxygen loss would improve cycle life[76]. This surface reactivity could also be linked to the visible surface layer for the reference cells aged at the homogeneous steady-state aging temperatures[2]. However, none of the evaluated images of the positive electrodes aged with a thermal gradient showed an additional surface film.

This additional surface film could have multiple causes as presented by Cloos et al.[2]. At very high voltages such as 4.5 V an increase of the CEI was observed[307]. Not only CEI but other structural changes increase. These can be the release of oxygen at higher charging levels for layered oxides[57] resulting in rock salt structure. This can further be supported by cation mixing[61,62]. LMO can form an oxygen-rich spinel phase[67] and can also oxidize electrolyte[70] at high charges. These processes can also be affected by LLI which causes “anode slippage” raising the positive electrode potential and increasing positive electrode impedance[167]. Even though increased positive electrode degradation is related to higher voltages, Jung et al.[308] have proven that the oxygen release onset is purely determined by the 81 % lithium ion removal from the NMC. It seems possible that there are differences in positive electrode charging between homogeneous steady-state and inhomogeneous-steady state cases because it was already shown in

literature that thermal gradients reduce the accessible capacity[43] and cause unutilized electrode areas[42]. However, the conclusions based on SEM are not robust without second evidence.

Apart from positive electrode, **negative electrode particle** aging should also be investigated (Figure 4.4).

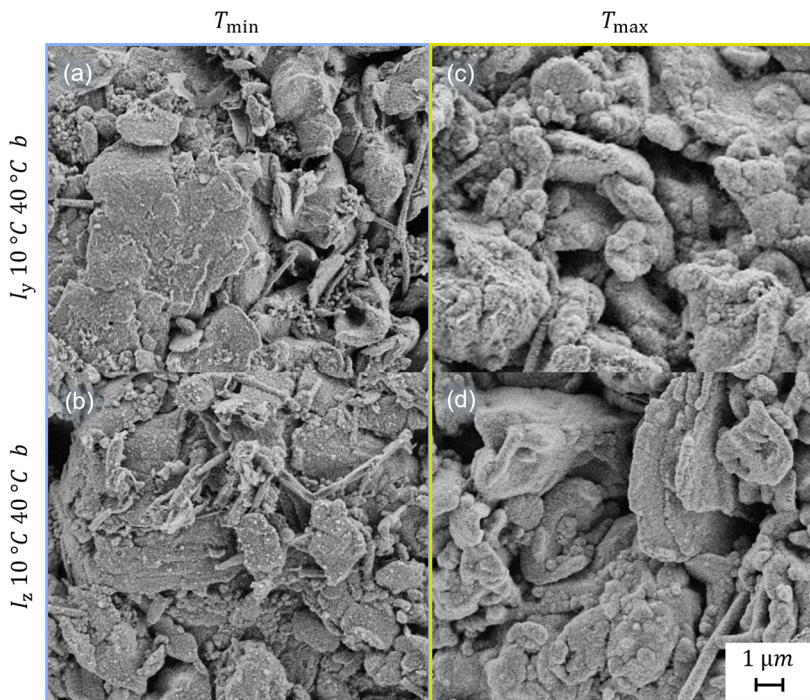


Figure 4.4: Pictures of SEM analysis on aged “Enertech” negative electrodes aged at lower (left) and higher (right) local aging temperatures than 25 °C ((a, c) Reproduced with permission under the terms of Creative Commons Attribution 4.0 License CC BY.[1] Copyright 2025, The Authors. Energy Technology published by Wiley-VCH GmbH.).

For the thermally inhomogeneously aged cells with and in-plane I_y 10 °C 40 °C and through-plane thermal gradient I_z 10 °C 40 °C SEM of the negative electrodes were checked with SEM in a first step. In Figure 4.4, the negative electrodes in areas of lower (left) and higher (right) local aging temperatures are presented. The graphite particles in the area of higher local temperatures close to the 40 °C boundary condition showed visible rounding of the edges which can be connected to increased SEI growth[45]. This effect was not as apparent for the graphite particles in the area of lower local temperature close to the 10 °C boundary condition. This supported the hypothesis of Paarmann et al.[45] that the local aging is according to the local aging temperature, specifically for SEI. [1]

The hypothesis of locally increased SEI was supported by a thickness measurement of the pouch cells with an in-plane thermal gradient I_z 10 °C 40 °C a before cell opening. The overall pouch cell thickness was significantly increased which can be seen at the top of the pouch cell (x-direction) and close to the tabs (green in comparison to gray at BoL, Figure 4.5). More importantly, the pouch cell thickness was significantly larger close to the positive electrode tab Tab_{PE} which was exposed to the higher temperature boundary condition of 40 °C. [1]

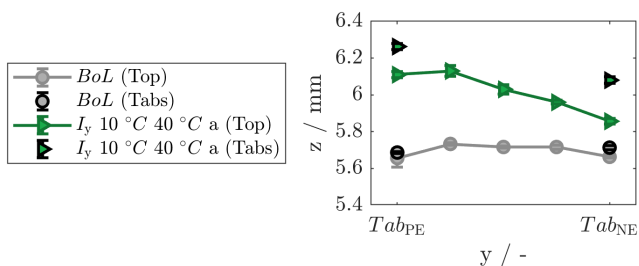


Figure 4.5: Pouch cell thickness of cell I_y 10 °C 40 °C a at the top of the “EnerTech” pouch cell and close to the tabs (Reproduced with permission under the terms of Creative Commons Attribution 4.0 License CC BY.[1] Copyright 2025, The Authors. Energy Technology published by Wiley-VCH GmbH.).

Alterations of the negative electrode sheets were also visible without magnification. In Figure 4.6, selected negative electrodes of cells aged with an in-plane (left) and through-plane (right) thermal gradient from 10 °C to 40 °C are shown.

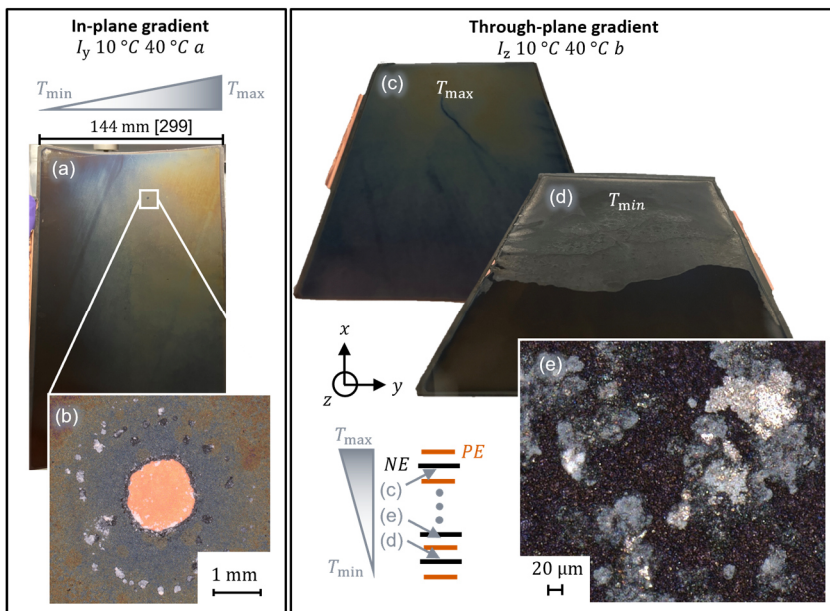


Figure 4.6: Pictures of negative electrode sheets of cell (a,b) I_y 10 °C 40 °C a and (c-e) I_z 10 °C 40 °C b with light microscopy pictures (b,e) (Adapted with permission under the terms of Creative Commons Attribution 4.0 License CC BY.[1] Copyright 2025, The Authors. Energy Technology published by Wiley-VCH GmbH.).

The applied thermal gradient during cyclic aging could be reconstructed with the color gradient of the negative electrode sheets. Areas which were exposed to a higher local aging temperature (Figure 4.6 (a, c)) showed a lighter blue and yellow coloration. Areas of lower local aging temperature had a grey coloration. The color differences of negative electrode sheets are usually related to different degrees of lithiation[124]. This seemed unlikely

because the cells had weeks to homogenize[176]. Another reason for this coloration was found by Storch et al.[309]. They related the blue coloration to additional surface effects such as increased SEI and presence of manganese which was already proven for this study. [1]

Additional differences were noticed from top to bottom of the negative electrode sheets with respect to the x-axis. The cells were cycled in an upright position (Figure 3.2) and it seemed possible that accumulated electrolyte in the bottom of the cell[310] could cause inhomogeneities. Also, slight inhomogeneity from the center to the corners of the cells were observed. This could have multiple reasons such as slight temperature differences[47] or pressure differences[178]. But it could also be due to salt inhomogeneity which was previously found due to the electrolyte motion in large format cells[311]. [1]

Bond et al.[312] also revealed spatially inhomogeneous kinetics correlating to positive electrode microcracking on smaller cells under heavy-duty cycling for 2.5 years. They also suggested inhomogeneous electrolyte, pressure or temperature as a possible origin. That highlights that such additional inhomogeneities are not necessarily just important in a larger format cell.

Additionally, a consistent cover layer on the negative electrode sheets exposed to the lower temperature boundary conditions for a through-plane gradient was seen (Figure 4.6 (d, e)). When taking a closer look with the light microscope in Figure 4.6 (e), metallic and white depositions were observed. ICP-OES and EDX of these depositions revealed lithium, phosphorus, manganese, aluminum as well as oxygen and fluorine. Potentially, these depositions were lithium plating with/or side reaction products. The origin of the cover layer could be the combination of a through-plane thermal gradient at the lower temperature side with a loss of LiPF_6 [313] facilitating lithium plating. This cover layer did not dominate the capacity loss, yet. [1]

Furthermore, the negative electrode sheets showed missing coating in distinct areas. Once, it was found in an area of medium to higher aging

temperature from a negative electrode sheet of cell I_y 10 °C 40 °C a (light microscopy in Figure 4.6 (b)). Other times, it was seen in areas of the cover layer (example in Figure 4.6 (d)) such as close to the tabs. Lithium plating close to the tabs was previously seen[187]. The missing coating could originate from a soft short-circuit. However, lithium dendrite growth is very complex[116,314] and is not discussed in further detail. [1]

The discussed aging results for the cells aged with a thermal gradient from 10 °C to 40 °C did not show a different capacity loss for in-plane versus through-plane thermal gradient. Even more interesting were the disassembled negative electrode sheets of the cells aged with an applied temperature difference from 30 °C to 50 °C. Not only did these aging conditions cause different capacity loss acceleration for in-plane and through-plane thermal gradients, they were also cycled past their capacity knee. A representative negative electrode sheet of the cell aged with an in-plane thermal gradient I_y 30 °C 50 °C a was shown in Figure 4.7 on page 96. [1]

The color differences were not as obvious. This was expected because the minimum and maximum local aging temperatures are both above 25 °C favoring similar aging mechanisms. However, in the center of the electrode sheet, pillar like white depositions were observed. These were attributed to the capacity knee of homogeneously aged cells at elevated temperatures[2]. [1]



Figure 4.7: Picture of negative electrode sheet of aged “Enertech” I_y 30 °C 50 °C a (Reproduced with permission under the terms of Creative Commons Attribution 4.0 License CC BY.[1] Copyright 2025, The Authors. Energy Technology published by Wiley-VCH GmbH.).

An in-plane thermal gradient of 20 K at an average temperature of 40 °C accelerated the capacity loss mildly. The acceleration was doubled for a through-plane thermal gradient. During cell opening of the cell I_z 30 °C 50 °C a , drastic changes to the electrode sheets became apparent. The electrode sheets were dry and debris attached to the separator (Figure 4.8 (b,f)).

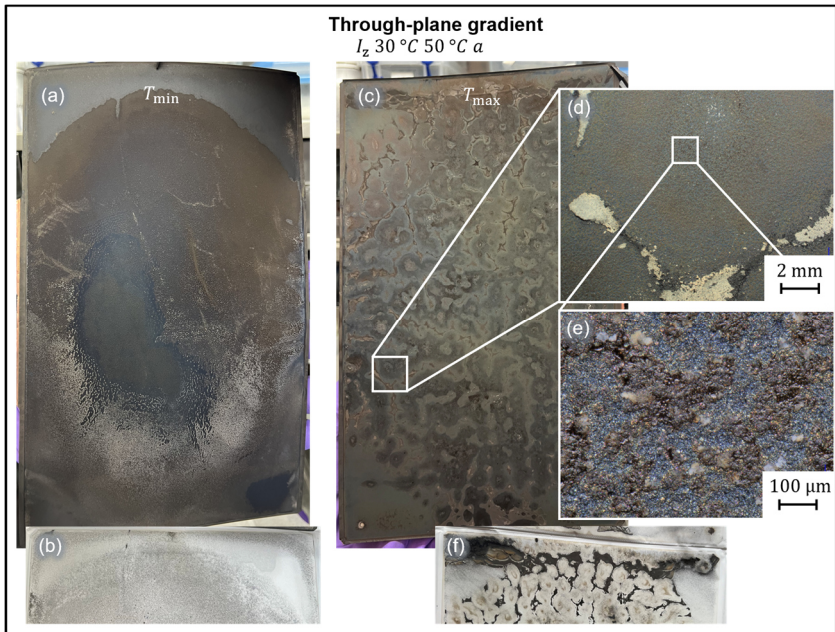


Figure 4.8: Pictures of negative electrode sheets (a, c) and separators (b, f) of cell I_z 30 °C 50 °C *a* with light microscopy pictures (d, e) Reproduced with permission under the terms of Creative Commons Attribution 4.0 License CC BY.[1] Copyright 2025, The Authors. Energy Technology published by Wiley-VCH GmbH.).

The negative electrode sheets close to the lower temperature boundary condition of 30 °C had an all over cover layer (Figure 4.8 (a)) as seen for the cell I_z 10 °C 40 °C *b*. Throughout the cell stack, the depositions on the negative electrode became more pillar like until an unknown alteration of the negative electrode (Figure 4.8 (c)) became visible. Under the light microscope, the structure looked like white honeycomb depositions with a darker area in between. Potentially, it is related to a dry-out phenomenon[315]. [1]

The aging acceleration due to a thermal gradient of 30 K around 25 °C in comparison to the reference was relatively small in comparison to the aging acceleration by increasing the overall aging temperature from 25 °C to 40 °C. The question remains whether some of the electrical stress-factors were chosen in such a way that they had a mitigating effect. The identified most relevant **aging stress factors and their potential interrelation** were discussed in chapter 3.2.3. The stress-factor DoD was determined to be potentially relevant for the global aging behavior with superimposed thermal gradients. Both aging studies on the “Kokam”[17,44] and on the “Ener-tech”[1] were done with a DoD of 100 % - between the cut-off voltages. The question arises whether a reduction of the DoD would lead to an inhomogeneous utilization of the regions in the cell stack and to an increased aging acceleration.

For this reason, an additional aging series with three “Ener-tech” cells at an equivalent aging temperature of 25 °C was conducted. A homogeneously tempered cell and one cell each with an in-plane and a through-plane temperature gradient of 30 K were cycled from the upper cut-off voltage to DoD of 70 % of the aged nominal capacity. The results are shown in Figure 4.9 on page 99 in black markers (70 % DoD) and compared to the previous aging study at 100 % DoD in green markers.

Unfortunately, the temperature setting was faulty at higher EFC as can be seen in Table 3 A in the Appendix. Specifically, the temperature control was correct until checkup 26 for cell $I_y 10\text{ }^{\circ}\text{C } 40\text{ }^{\circ}\text{C } a (70\text{ \% } DoD)$ which is sufficient for this analysis. Overall, a reduction of DoD is milder on the capacity loss which is in line with literature[155]. The acceleration A_{II} (Eq. 4.1) of $I_y 10\text{ }^{\circ}\text{C } 40\text{ }^{\circ}\text{C } a (70\text{ \% } DoD)$ in comparison to $25\text{ }^{\circ}\text{C } a (70\text{ \% } DoD)$ is $58\text{ \% } \pm 10\text{ \%}$. This is more than double the amount in comparison to the acceleration factor of $I_y 10\text{ }^{\circ}\text{C } 40\text{ }^{\circ}\text{C } a$ cycled for 100 % DoD. It seems possible, that the initial hypothesis of more inhomogeneous utilization of segments of cell stack is true. The simulative analysis of these cases will give some additional hints as described in the next section.

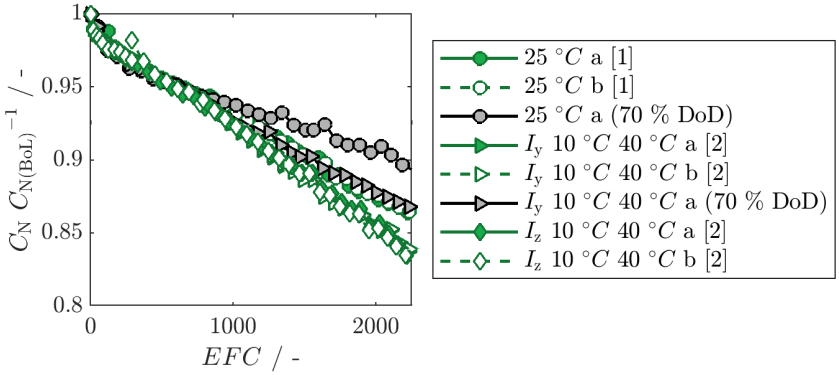


Figure 4.9: Relative capacity decrease over equivalent full cycles (EFC) for “EnerTech” with a depth of discharge (DoD) of 100 % (green) (Adapted with permission under the terms of Creative Commons Attribution 4.0 License CC BY.[2] Copyright 2024, The Authors. Published on behalf of The Electrochemical Society by IOP Publishing Limited and with permission under the terms of Creative Commons Attribution 4.0 License CC BY.[1] Copyright 2025, The Authors. Energy Technology published by Wiley-VCH GmbH.) and a DoD of 70 % (black) for an equivalent aging temperature of 25 °C and homogeneous steady-state (circles) versus inhomogeneous steady-state (triangle and diamond) thermal boundary condition.

4.2 Model Supported Insights into Inhomogeneous Steady-State Aging

The presented experimental analysis on the effect of inhomogeneous thermal boundary conditions on the local aging behavior of LIB was based on findings at EoL. The validated thermal-electrical aging model can give further insight into the internal behavior over the entire cycling time. The simulated states of each segment representing a spatial part of the electrode stack in the model can be analyzed. The available states are the capacity, resistance, temperature, voltage, current, SoC. Focusing on the aging behavior, the capacity loss of a cell cycled with an in-plane thermal

gradient is discussed first (Figure 4.10). The capacity loss of each segment at its distinct aging temperature will be compared to the full cell.

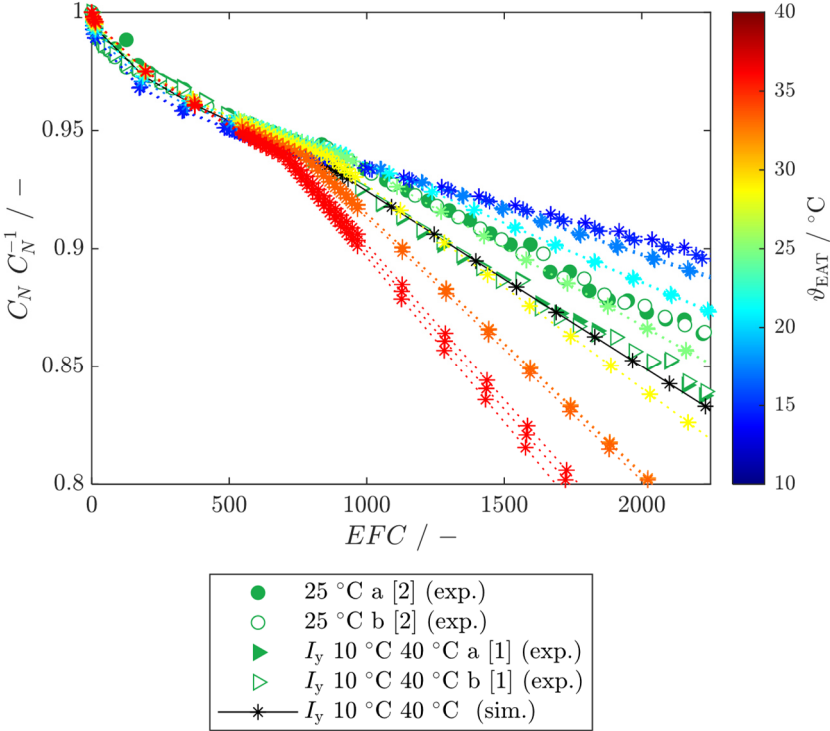


Figure 4.10: Relative nominal capacity over equivalent full cycles (EFC) comparison of experimental and simulative results (“Enertech”). Experimental data for aging at homogeneous aging temperature of 25 °C and inhomogeneous aging for I_y 10 °C 40 °C illustrated with markers (Adapted with permission under the terms of Creative Commons Attribution 4.0 License CC BY.[2] Copyright 2024, The Authors. Published on behalf of The Electrochemical Society by IOP Publishing Limited and with permission under the terms of Creative Commons Attribution 4.0 License CC BY.[1] Copyright 2025, The Authors. Energy Technology published by Wiley-VCH GmbH.) Simulative data for inhomogeneous aging for I_y 10 °C 40 °C for all segments indicated with lines and stars in the color of the local aging temperature. Black line represents simulated cell behavior of cell I_y 10 °C 40 °C.

A simulation for a 6x7 segmentation and a Dirichlet temperature boundary condition from 10 °C to 40 °C in y-direction (in-plane thermal gradient) was performed for the “EnerTech”. The settings were presented in detail in chapter 3.2.5. The result of the capacity loss of each segment is marked with stars (*) in the respective aging temperature rainbow color in Figure 4.10. The markers represent the “checkup” points of the simulation where an update of parameters and the simulation of a new cycle were performed. The experimental data is shown in green circles and triangles.

The average of the SoH and EFC of all segments for each simulated checkup is shown in black. This is in line with the hypothesis formulated from the experimental analysis. Cloos and Wetzel[1] suggested that *“the aging acceleration of an in-plane thermal gradient was determined by the sum of the local aging accelerations”*. For the simulation, it is interpreted in the following way: The sum of all aged segment capacities amounts to the aged capacity of the full cell. Thereby, the capacity of each segment is initially calculated as the spatial ratio of the entire cell. In other words, the relative full cell capacity can be calculated as the average of the relative capacity of all segments. The same was done for the calculation of the full cell EFC.

The **capacity loss** over EFC for the individual segments increases for higher aging temperatures as defined with the Arrhenius equation (3.9). As parameterized in the aging model, the segment at an aging temperature of 25 °C (light green) matches the experimental pouch cell data at 25 °C (green circles). The average of the simulated relative capacity of all segments (black stars) matches the experimental capacity loss of a full cell with inhomogeneous thermal boundary condition I_y 10 °C 40 °C (green triangles) precisely. The initial power decay, the point of acceleration and the linear regime are matched. These results support the hypothesis on the full cell capacity being the sum of the segment capacities. It also highlights that the capacity loss acceleration of aging with a thermal gradient from 10 °C to 40 °C was mainly due to increased SEI at higher local aging temperatures predicted by Cloos and Wetzel[1].

The findings suggest that knowledge of the capacity loss at different homogeneous aging temperatures and the local temperatures in the cell suffice to predict the capacity loss of an inhomogeneously aged cell analytically based on equations (3.7) – (3.9). Of course, this **analytical approach** neglects additional aging mechanisms found for through-plane thermal gradients[1]. These were in part related to the potential of lithium plating and a knee onset cannot be predicted. To estimate the potential of lithium plating, a model simulating the negative electrode potential during charging is necessary and evaluated in the following.

In Figure 4.11, the **current distribution** and the **negative electrode potential** U_{NE} during charging are shown for three selected segments for each simulated “checkup” as illustrated with a color fade.

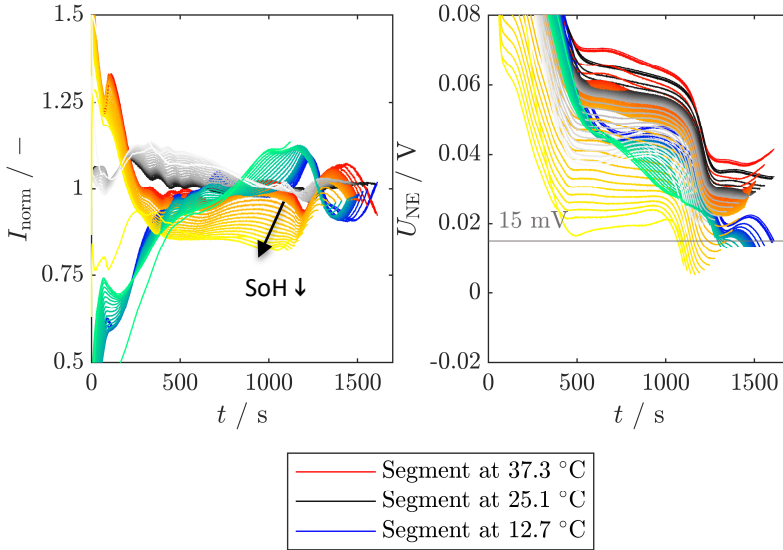


Figure 4.11: Simulated normed current distribution I_{norm} (left) and negative electrode potential U_{NE} (right) for three elements of an inhomogeneous temperature field I_y 10 °C 40 °C at high (red-yellow), medium (black-grey) and low (blue-green) segment temperature over aging in charging direction (simulated SoH_{min} of 79.6 %).

With each simulated “checkup” the SoH decreases as shown with the black arrow. The last simulated “checkup” is at a SoH of 79.6 %. The chosen segments are at the highest and lowest local temperature close to the tabs and the temperature boundary condition as well as a medium temperature segment at 25 °C. The current distribution is plotted as the normalized current I_{norm} . The normalized current of a segment is defined by Paarmann et al.[30] as the current of the segment multiplied with the number of segments and divided by the full cell current.

The current swapping during charging of the “Enertech” is shown in Figure 4.11 on the left. As expected, the segments with higher temperatures get loaded first due to the lower resistances at higher temperatures. The currents are widely spread at the beginning of charging. Then, the current distribution is converging and diverging again in relation with the OCV. At the end of charging, the currents converge again.

Over the course of aging, it is obvious that the current in the higher temperature segment reduces in the beginning and middle of charging. This supports the previously suggested mitigating effect of decreasing current in the segments of higher aging temperatures over aging. This could be guessed for the “Enertech” beforehand when comparing the increase of resistance due to temperature and aging. The changes are in the same order. However, this effect does not necessarily cause a reduction of current inhomogeneity as can be seen both for charging (Figure 4.11) and discharging direction (Figure 4.12 on page 104).

In discharging direction, a large discharging time reduction can be observed between the first and second simulated “checkup”. This is due to the fact, that the first discharge starts from defined SoC 100 %. Over the course of aging, the discharging and charging cycles oscillate in a lower DoD range and do not reach high SoCs again. Only in the beginning of discharging the inhomogeneity reduces over aging. Then, the spread of current actually increases both in charging and discharging direction. At the end, where high

local currents might be even more harmful, the current inhomogeneity stays the same. Clearly, the current swapping behavior is very complex.

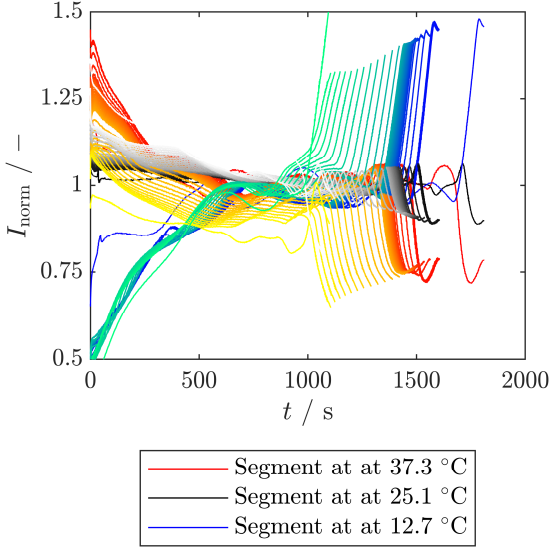


Figure 4.12: Simulated normed current distribution I_{norm} for three elements of an inhomogeneous temperature field I_y 10 °C 40 °C at high (red-yellow), medium (black-grey) and low (blue-green) segment temperature over aging in discharging direction (simulated SoH_{min} of 79.6 %).

In Figure 4.11 (right), the negative electrode potentials during charging of the same segments are presented. For better visualization, a voltage threshold of 15 mV is inserted. However, this plot can only be analyzed qualitatively because of initial assumptions of the negative electrode over-voltages given in chapter 3.2.1. The low temperature segment has low negative electrode potentials at the end of charging from BoL to EoL. This is qualitatively similar with simulative results by Sun et al.[227]. They found a higher concentration of lithium plating at the lower temperature side for a thermal gradient of 10 K. The low negative electrode potential might even enable lithium plating because additional local inhomogeneities of the

negative electrode potential on the particle scale are possible. Such inhomogeneities in negative electrode potential were found for the vertical distribution in the electrode coating by Klink et al.[191]. In post-mortem analysis of the I_y 10 °C 40 °C, small isolated cover layers on the negative electrodes were found in areas of the lower temperature[1]. This can also be stated for the higher temperature side. The negative electrode potential of the high temperature segment drops drastically over the course of aging, indeed. It even falls below the negative electrode potential of the lower temperature segment. For lower SoH, it is expected to drop even lower. A lithium plating onset in the higher temperature segment could then induce a capacity knee.

Experimentally, a **reduced DoD with superimposed thermal gradient** was found to be more harmful compared to the reference. Therefore, a simulation with the same thermal settings and same parameterization but a reduced DoD of 70 % was performed. The results in Figure 4.13 on page 106 can only be seen as a preliminary qualitative result. For more reliable results, the stress factor DoD needs to be included in the aging model which was not done here. This means that the predicted capacity loss is overestimated.

Nevertheless, preliminary conclusions can be drawn. The differences in the current distribution between a DoD of 100 % (Figure 4.11) and a DoD of 70 % (Figure 4.13) arise from the cycling in different OCV regions which alters the current swapping behavior. And this seems to become hazardous to the cell. The current does not converge at the end of charging as seen for a DoD of 100 %. The current in the lower temperature segment increases significantly. Even though the lower temperature segment is cycled in a smaller capacity window it is particularly loaded at the end of charging. This is in line with the initial hypothesis that a lower DoD would cause a more inhomogeneous utilization of the cell stack.

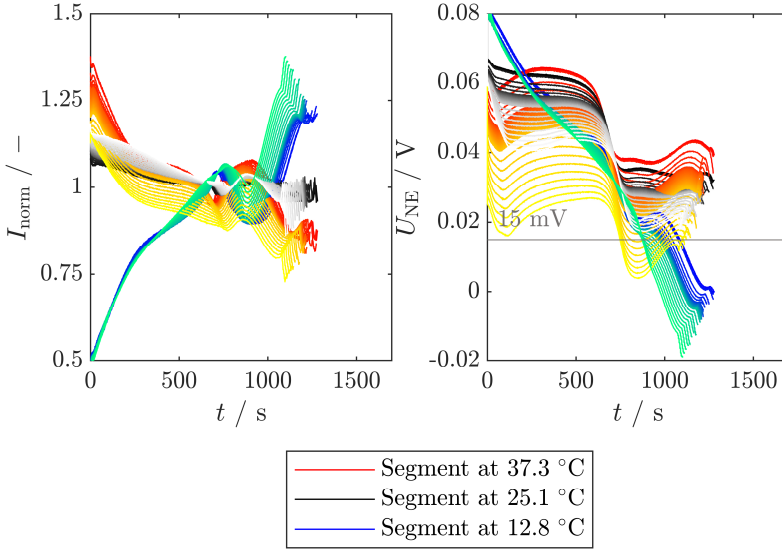


Figure 4.13: Preliminary trends for cycling at a reduced DoD of 70 % of the “EnerTech” – Simulated normed current distribution I_{norm} (left) and negative electrode potential U_{NE} (right) for three elements of an inhomogeneous temperature field I_T , 10 °C 40 °C at high (red-yellow), medium (black-grey) and low (blue-green) segment temperature over aging in charging direction. (simulated SoH_{min} of 84.4 %).

This current divergence is linked to the estimated negative electrode potential. It becomes negative in the lower temperature segment from the very first cycle at the end of charging. The negative electrode potential is low from the beginning of charging. This could explain the increased capacity loss acceleration for lower DoDs and inhomogeneous thermal boundary conditions in Figure 4.9. These preliminary findings highlight the necessity of understanding the current swapping in the cell due to thermal inhomogeneities. Further investigations in that direction would be beneficial for predicting hazardous combinations of electrical and thermal stress factors.

4.3 Effects of Homogeneous Transient Temperatures

In comparison to thermal gradients, thermal transients have previously accelerated the capacity loss more drastically[17,26]. Therefore, Cloos et al.[3] performed an aging study on the “L 3.4” cell to investigate the possibility of thermal transients to reduce the aging testing time[316]. In this chapter, the main findings of Cloos et al.[3] are summarized as referenced for each paragraph.

The **relative capacity decrease** and resistance increase in Figure 4.14 (a, b) for the homogeneous steady-state (circles) and homogeneous transient (stars) temperature boundary conditions from 5 °C to 45 °C revealed two groups of tested conditions. Thereby, cells in group A were predominantly charged at 5 °C and experienced a very fast capacity decay. Group A includes the homogeneous steady-state temperature boundary conditions at 5 °C (blue circles) and the transients $T\ 45\ ^\circ\text{C}_{\text{dch}}\ 5\ ^\circ\text{C}_{\text{ch}}$ and $T\ 25\ ^\circ\text{C}_{\text{dch}}\ 5\ ^\circ\text{C}_{\text{ch}}$ (light blue and green filled stars). Since the temperature change was always performed at the beginning of each half-cycle, these transients mostly experienced 5 °C during charging except for the beginning (Figure 3.3). This drastic capacity decay was combined with a very low reproducibility which can be seen on the example of 5 °C steady-state homogeneous boundary condition. Still, the thermal transients $T\ 45\ ^\circ\text{C}_{\text{dch}}\ 5\ ^\circ\text{C}_{\text{ch}}$ reached a lower SoH overall. On the contrary, Group B showed a linear capacity loss trajectory with good capacity retention and high reproducibility for homogeneous steady-state thermal boundary conditions of 25 °C (green) and 45 °C (red). As expected, an aging temperature of 45 °C resulted in a lower SoH than an aging temperature of 25 °C[11]. Still, homogeneous transient condition $T\ 5\ ^\circ\text{C}_{\text{dch}}\ 45\ ^\circ\text{C}_{\text{ch}}$ (green unfilled stars) resulted in an even steeper capacity decay. [3]

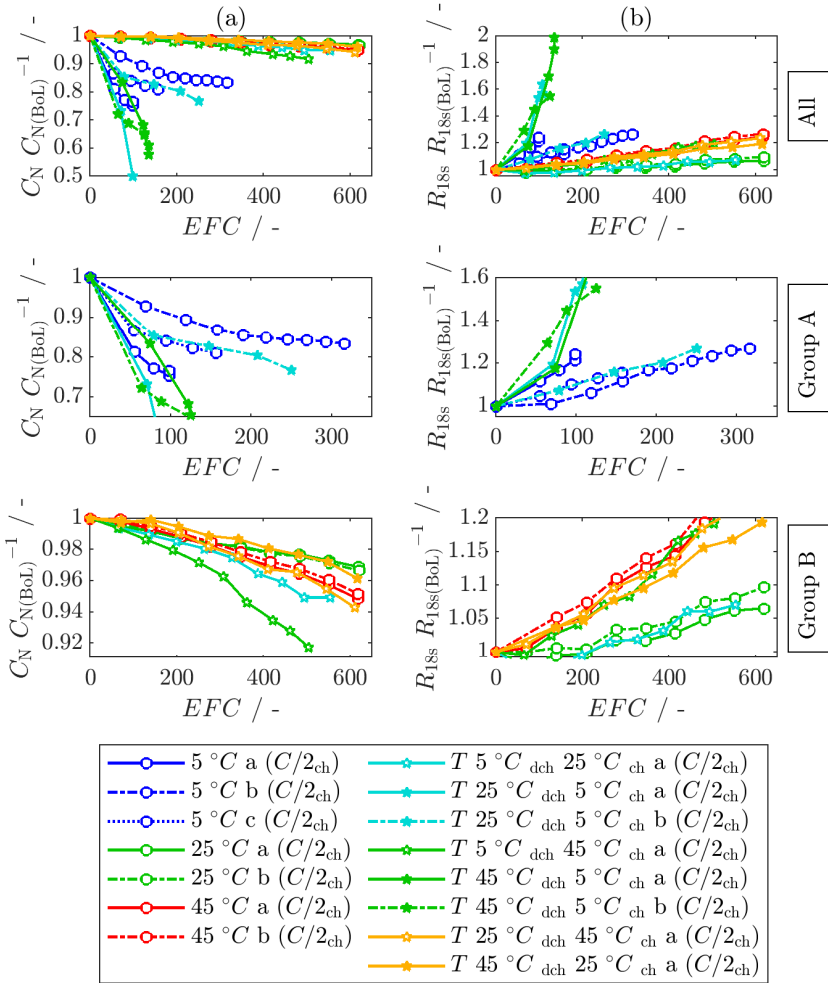


Figure 4.14: (a) Relative nominal capacity loss and (b) relative 18 s pulse resistance increase at 50 % SoC over equivalent full cycles (EFC) for “L 3.4” and homogeneous steady-state as well as homogeneous transient (T) thermal boundary conditions with spotlight figures of groups A and B (Adapted with permission under the terms of Creative Commons Attribution 4.0 License CC BY.[3] Copyright 2023, The Authors. Batteries & Supercaps published by Wiley-VCH GmbH.).

The **pulse resistance increase** showed different trends than the capacity loss. First of all, a resistance decay was observed for some of the investigated cells. Such a resistance decrease was previously found[44,317] and is potentially related to changes in SEI resistance[318]. Furthermore, higher equivalent aging temperatures resulted in a higher resistance increase. This could also be due to increasing SEI resistance[11] or positive electrode resistance[319]. Group A displayed a similarly steep pulse resistance increase as capacity loss. From capacity and resistance analysis it can be concluded that charging at 5 °C and C/2 is harmful to the cell which might be related to lithium plating[11]. [3]

Additional analysis methods were evaluated to support the findings. A **capacity difference analysis (CDA)** was performed to check for lateral diffusion of Li^+ in the negative electrode[184]. An increase in the difference of the measured capacity with a lower and higher C-Rate can hint towards a lithiation inhomogeneity and cover layer formation on the negative electrode[320]. The CDA result of all investigated cells is shown in Figure 4.15 on page 110. [3]

An increase in CDA could be observed for Group A and all cells aged with a thermal transient. A cover layer formation resulting from lithium plating at lower temperatures was expected. However, the CDA increase for the other transients including the ones at higher temperatures from 25 °C to 45 °C was unexpected. Potential inhomogeneities can be suspected by DVA results but only proven after cell opening. [3]

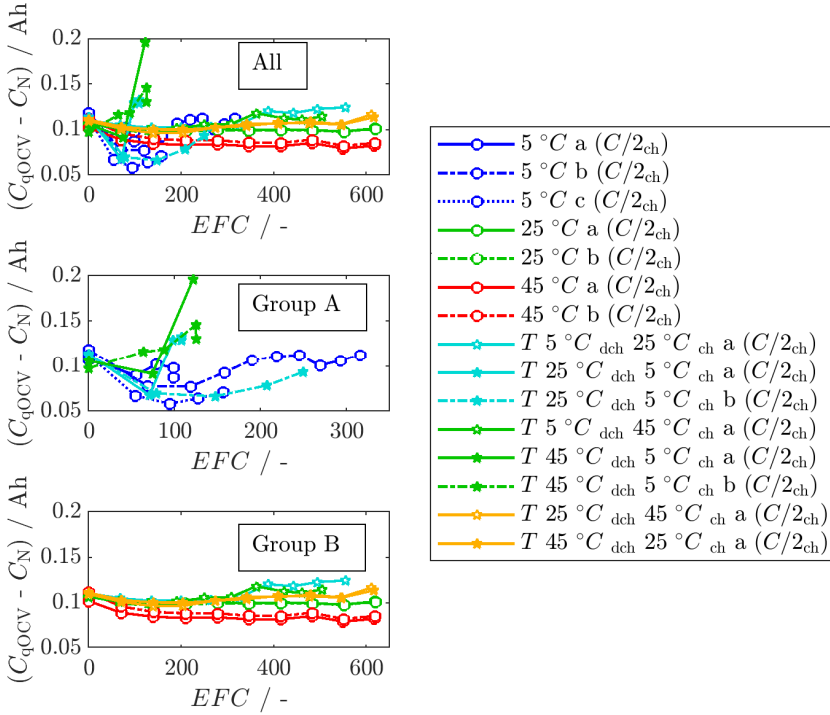


Figure 4.15: Capacity difference analysis (CDA) over equivalent full cycles (EFC) for “L 3.4” and homogeneous steady-state as well as homogeneous transient (T) thermal boundary conditions with spotlight figures of groups A and B (Adapted with permission under the terms of Creative Commons Attribution 4.0 License CC BY.[3] Copyright 2023, The Authors. Batteries & Supercaps published by Wiley-VCH GmbH.).

In **post-mortem analysis**, selected cells were opened and the negative electrodes were visually analyzed (Figure 4.16). A homogeneous steady-state aging temperature of $5\text{ }^{\circ}\text{C}$ caused an all-over metallic cover layer on the negative electrode ($5\text{ }^{\circ}\text{C c}$). This supported previous speculations on potential lithium plating. Burns et al.[321] also found very similar cover layers for their lithium plating investigation. A higher homogeneous steady-

state aging temperature of 45 °C (45 °C *b*) in comparison to 25 °C (25 °C *b*) resulted in a lighter negative electrode coloration and increased dryness which might be related to electrolyte decomposition and increased SEI growth[161]. [3]

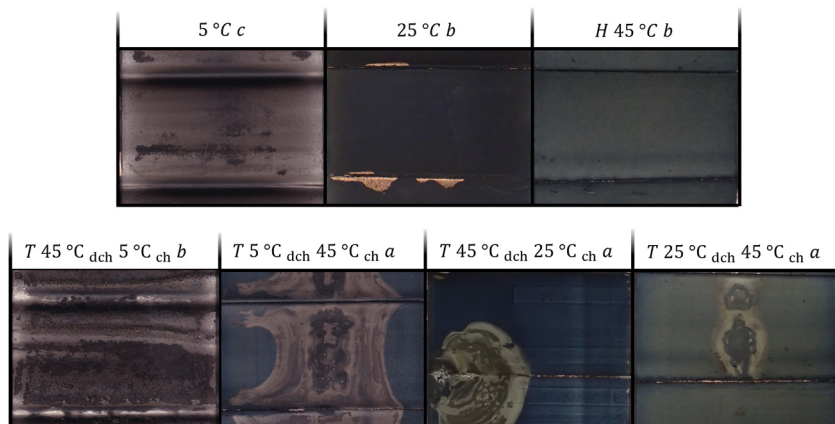


Figure 4.16: Pictures of selected negative electrodes of homogeneous steady-state aging temperatures (top) and homogeneous transient temperatures (bottom) of “L 3.4” (Reproduced with permission under the terms of Creative Commons Attribution 4.0 License CC BY.[3] Copyright 2023, The Authors. Batteries & Supercaps published by Wiley-VCH GmbH.).

All opened cells which were cycled with superimposed temperature changes showed cover layer formation on the negative electrode (Figure 4.16, bottom). These cover layers varied in their color, size and position. The cell $T\ 45\ ^\circ\text{C}_{\text{dch}}\ 5\ ^\circ\text{C}_{\text{ch}}\ b$ was part of group A as was $5\ ^\circ\text{C}\ c$. The pouch cell $T\ 45\ ^\circ\text{C}_{\text{dch}}\ 5\ ^\circ\text{C}_{\text{ch}}\ b$ showed obvious signs of gassing before cell opening which was not the case for the $5\ ^\circ\text{C}\ c$. The negative electrodes of both cells had a cover layer over the entire jelly role. In comparison to $5\ ^\circ\text{C}\ c$, the cover layer of $T\ 45\ ^\circ\text{C}_{\text{dch}}\ 5\ ^\circ\text{C}_{\text{ch}}\ b$ was strongly delaminating. Both were signs which could be related to the reaction of deposited lithium with electrolyte[112] which is enhanced at higher temperatures[46,238]. This

higher temperature was only present for the homogeneous transient thermal boundary conditions and not for the homogeneous steady-state boundary conditions of group A. [3]

The depositions on the negative electrodes for the cells of group B in Figure 4.16 were not visible over the entire jelly roll but only in particular positions. A **correlation** of the location of the depositions with respect to the temperature changes could be postulated. Thereby, the negative electrode depositions were mostly found in areas where the local temperature was predicted to be higher during the temperature change at the beginning of charging as illustrated in Figure 4.17 and explained in more detail by Cloos et al.[3]. [3]

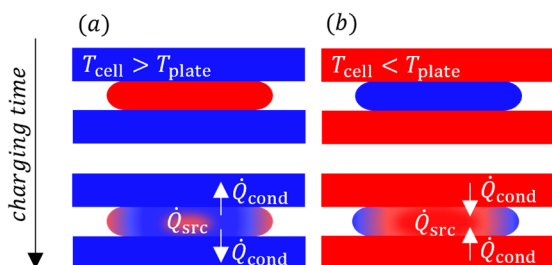


Figure 4.17: Schematic to illustrate temperature field during thermal transients (Reproduced with permission under the terms of Creative Commons Attribution 4.0 License CC BY.[3] Copyright 2023, The Authors. Batteries & Supercaps published by Wiley-VCH GmbH.).

Previously, steady-state inhomogeneous temperature conditions caused changes in the electrode potential which breach the lithium plating condition due to limited transport of lithium to the cell center at the higher temperature[47]. A comparison of the results for homogeneous transient and inhomogeneous steady-state thermal boundary conditions was made because of predicted inhomogeneous temperature fields during the temperature changes. However, a main difference between thermal transients

and thermal gradients is the temporal change. Paarmann et al.[45] suggested that the temperature change could cause local imbalances which impact rate-determining processes during charging on electrode level. Also, thermal transients can enable faster reaction of plated lithium during the subsequent higher temperature phase[46,238]. This explains why the thermal transient between 0 °C and 25 °C in the study of Werner et al. caused less severe capacity loss acceleration because 25 °C is in the medium temperature range. [3]

These results on fast temperature changes during cycling can be compared to a recent study by Feinauer et al.[223] for temperature changes between periods of cycling – also called temperature path-dependency. The results of Feinauer et al.[223] differed greatly. They found no aging acceleration when first cycling in lithium plating condition and then changing to a higher aging temperature. There are two possibilities. Either the aging results with thermal transients found on the “L 3.4” are not transferable. Or, the temporal change of the temperature field during cycling and the high number of changes of aging temperature is a main driver and difference to the study of Feinauer et al.[223]. The question of transferability of the aging behavior with thermal transients is examined in the next chapter.

4.4 Severity of Inhomogeneous Steady-State versus Homogeneous Transient Temperatures

Trends and relations between the complex thermal boundary conditions and the cyclic aging behavior could already be identified. Firstly, the capacity loss acceleration of an inhomogeneous thermal boundary condition in a range of 30 to 50 K was in a range of 25 % for the “Enertech” and the “Kokam” which had different cell sizes and chemistries but are both a high power cell. Secondly, the capacity loss was accelerated to a greater extent for some thermal transients which was proven on the “Kokam” and the “L 3.4” in comparison to homogeneous steady-state temperature conditions. These

cells have a similar cell size but different chemistries and differ in the cell stack configuration. Only for the aging study on the “Kokam” by Werner et al.[17,44] a direct comparison was made for thermal transients and thermal gradients. To prove these trends and relations, further studies were performed.

Comparison of Homogeneous Transient and Inhomogeneous Steady-State Thermal Boundary Condition

In Figure 4.18, the results of a cyclic aging test of “L 3.4” cells with through-plane thermal gradient boundary condition from 10 °C to 40 °C (I_z 10 °C 40 °C) are shown.

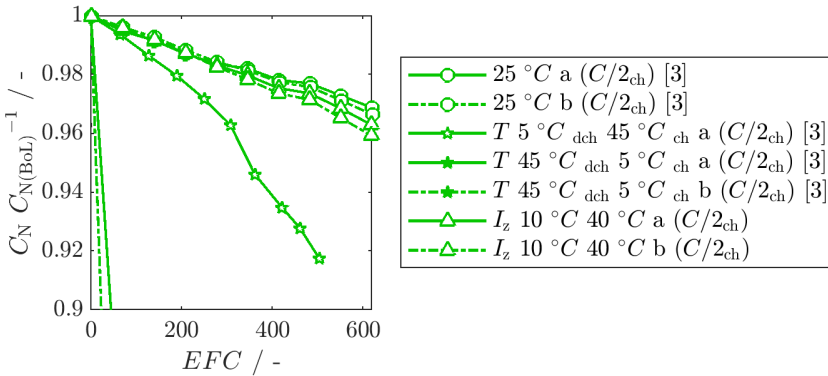


Figure 4.18: Relative nominal capacity loss over EFC for homogeneous steady-state, homogeneous transient T (Reproduced with permission under the terms of Creative Commons Attribution 4.0 License CC BY.[3] Copyright 2023, The Authors. Batteries & Supercaps published by Wiley-VCH GmbH.) and inhomogeneous steady-state I_z temperature boundary conditions on “L 3.4”.

The results are compared to the cyclic aging tests at a homogeneous steady-state temperature of 25 °C and homogeneous transient case of T 5 °C_{dch} 45 °C_{ch} a. The temperature difference is 10 K less for the

through-plane thermal gradient than the transient case. A comparison can be made, nonetheless.

During the testing time of approximately 600 EFC, the capacity loss caused by the steady-state inhomogeneous thermal boundary condition (triangle) was in the range of uncertainty of the reference steady-state homogeneous condition (circle). In the same testing time, the transient homogeneous thermal boundary condition had a three times higher capacity decrease[3]. The trends observed for the “Kokam” could be confirmed, indeed.

Even though the capacity loss acceleration due to the through-plane inhomogeneous steady-state boundary condition was in the range of uncertainty, an acceleration could be guessed in extrapolation. Therefore, the cell I_z 10 °C 40 °C b was opened to check for similarities and differences in aging mechanisms due to through-plane thermal gradients between “L 3.4” and “Enertech”. The same aging condition was applied to both cells. However, the SoH during cell opening was a lot higher of the “L 3.4” than the “Enertech”.

In Figure 4.19, the outermost negative electrode windings of the jelly roll of cell I_z 10 °C 40 °C b are shown from both sides. The color differences of the electrode “sheets” between the windings of the negative electrode are clearly evident. The color alternated between grey and blue according to the temperature boundary condition. Close to the lower temperature boundary condition, the negative electrode coating had a grey color. Close to the higher temperature boundary condition, it was blue in color. Towards the cell center the coloring become more homogeneous in a blue shade. This blue color could also be seen for “L 3.4” negative electrodes aged at 25 °C and 45 °C in Figure 4.16. It was also seen to a greater extent for the “Enertech” aged with the same through-plane thermal gradient from 10 °C to 40 °C in Figure 4.6 (c, d). These colors could be related to different lithiation stages or surface effects[309] at different aging temperatures[1].



Figure 4.19: Picture of negative electrode sheets of “L 3.4” with the aging condition I_z 10 °C 40 °C b.

Two more aging phenomena were observed. Firstly, the negative electrode coating with the blue coloration was very brittle. This was not the case for the homogeneous steady-state reference cases. It is a sign of additional stresses. Secondly, a cover layer onset could be detected at the negative electrode edges which were exposed to the lower thermal boundary conditions (see white arrow in Figure 4.19 bottom). A more prominent cover layer was also observed at the lower temperature side of the through-plane thermal gradient of the “Enertech” in Figure 4.6 (d).

The results confirm the importance of the local aging temperature for the local aging mechanisms. They also underline the risk of cover-layer formation at the negative electrode close to the lower temperature boundary condition in a thermal gradient. The observed cover layer onset for the through-plane thermal gradient on the “L 3.4” catalyzes a discussion about the directionality of the thermal gradient and the cell geometry. A consistent cover-layer at the lower temperature side was an additional aging mechanism observed for the “Enertech” with a through-plane in comparison to an in-plane thermal gradient. Potentially the cover layer of the “L 3.4” expands with decreasing SoH. But also the in-plane thermal gradient on the “Enertech” caused some sporadic cover layer formation. Theoretically, a through-plane thermal gradient on a cell with a wound jelly roll is comparable to an in-plane thermal gradient in a stacked electroded stack. For example, lateral lithium rehomogenization is possible. If such rehomogenization effects are relevant or not, cannot be concluded from these results. This also means that the exact mechanism behind the consistent cover layer formation for the through-plane thermal gradient in comparison to the in-plane thermal gradient of the “Enertech” remains unclear. Another hypothesis on the differences between in-plane and through-plane thermal gradient effect were potential temperature difference for the same applied temperatures. Again, spatially highly resolved thermal simulations could give an insight into the exact temperature field for different cell geometries.

Reduced Electrical and Thermal Aging Stress-Factors

Another open question from the last chapter was the reproducibility of aging acceleration due to thermal transients. This is interesting, because the charging with a C-rate of C/2 and temperature of 5 °C was found to be hazardous for the “L 3.4”. Additional tests at milder cycling conditions were performed to check whether the aging acceleration for thermal transients persists. The charging C-rate was reduced to C/5 and the minimum

temperature was increased to 10 °C. The relative qOCV capacity decrease is shown in Figure 4.20.

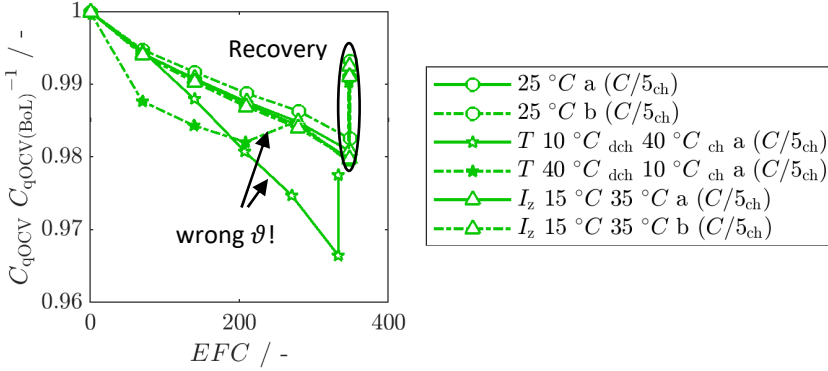


Figure 4.20: Relative qOCV capacity loss over EFC with reduced charging C-Rate and temperature differences for homogeneous steady-state, homogeneous transient T and inhomogeneous steady-state I_z temperature boundary conditions on “L 3.4”.

In this study, only few checkups were performed but the trends were already visible. The milder cycling conditions could eliminate any sudden capacity drops as seen for group A in Figure 4.14 (a). Even in this short amount of cycling time both thermal transient conditions have shown a higher relative capacity loss ($T 10\text{ °C}_{\text{dch}} 40\text{ °C}_{\text{ch}} a (C/5_{\text{ch}})$ and $T 40\text{ °C}_{\text{dch}} 10\text{ °C}_{\text{ch}} a (C/5_{\text{ch}})$) than the reference ($25\text{ °C } a$ and $25\text{ °C } b$). This was obvious before the fourth checkup. Afterwards, the temperature setting was faulty which strongly influenced the capacity loss trajectory as indicated in the figure. A through-plane thermal gradient between 15 °C and 35 °C caused a similar capacity loss than the reference at 25 °C.

After the sixth checkup, the cells were relaxed for a couple of days before a final checkup was performed. A strong recovery effect could be confirmed for the “L 3.4” cells as seen by Morales Torricos et al.[180] for another cell. It

is unclear why this recovery effect occurs in this study. It could be related to the anode overhang[174] or other rehomogenization effects[180].

This recovery undermines the usefulness of constant cycling without pauses in a laboratory setting. Raj et al.[212] have found cycling without rest to be one of the most harmful conditions. Furthermore, Schreiber et al.[322] have proven that CC-cycling largely underestimates the battery lifetime in automotive application in comparison to a commuter drive cycle. The application should be taken into account when designing experiments in the future. Nevertheless, not all cells show a strong recovery effect as can be seen in the following example.

Modern Cell Chemistry

In a similar testing setup than the “L 3.4”, the “L 1” was tested (Figure 4.21).

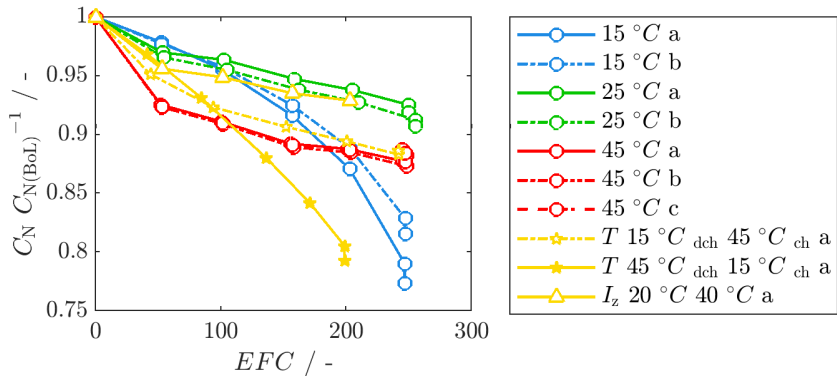


Figure 4.21: Relative nominal capacity loss over EFC for homogeneous steady-state, homogeneous transient T and inhomogeneous steady-state I_z temperature boundary conditions on “L 1”.

These cells comprise newer generation electrode materials with Ni-rich positive electrode and silicon containing negative electrode. Therefore, the general aging temperature dependency of the **references** (homogeneous

steady-state aging temperature) need to be analyzed first. The cells suffered from an initially higher capacity loss especially at higher cycling temperatures of 45 °C. Medium and higher homogeneous steady-state thermal boundary conditions (25 °C – green and 45 °C – red) resulted in a linear capacity decrease after the initial loss. An acceleration was observed for lower homogeneous steady-state thermal boundary conditions (15 °C – blue). Also, after a rest period of approximately one week, no capacity retention was observed.

The results are consistent with literature. Such a fast initial capacity loss also occurred for NMC811/Si-graphite cell from Laakso et al.[323]. Silicon is expected to shift the minimum aging rate[324]. They found mainly positive electrode degradation at higher aging temperatures of 45 °C and mainly negative electrode degradation at 5 °C. Overall, lower temperatures of 10 °C led to increased aging[325]. At lower temperatures, the stress in the negative electrode particles were predicted to increase[326].

In this study, the thermal transient conditions $T\ 15\ ^\circ\text{C}_{\text{dch}}\ 45\ ^\circ\text{C}_{\text{ch}}\ a$ and $T\ 45\ ^\circ\text{C}_{\text{dch}}\ 15\ ^\circ\text{C}_{\text{ch}}\ a$ have a higher equivalent aging temperature than 25 °C. Only a classification of the results in comparison to the performed references is possible. The capacity loss of the transient condition with a predominantly 15 °C charging temperature ($T\ 45\ ^\circ\text{C}_{\text{dch}}\ 15\ ^\circ\text{C}_{\text{ch}}\ a$) is greater than all reference at higher (45 °C) and lower (15 °C) aging temperatures. The findings confirm that certain temperature changes during cycling are hazardous across cell stack geometries and chemistries. The through-plane thermal gradient between 20 °C and 40 °C on the other hand experienced a low capacity decay.

The cells aged with a thermal transient $T\ 15\ ^\circ\text{C}_{\text{dch}}\ 45\ ^\circ\text{C}_{\text{ch}}\ a$ and $T\ 45\ ^\circ\text{C}_{\text{dch}}\ 15\ ^\circ\text{C}_{\text{ch}}\ a$ as well as a cell aged at a homogeneous steady-state temperature of 15 °C were visually investigated post-mortem. Some differences in the negative electrode coatings were observed (Figure 4.22).

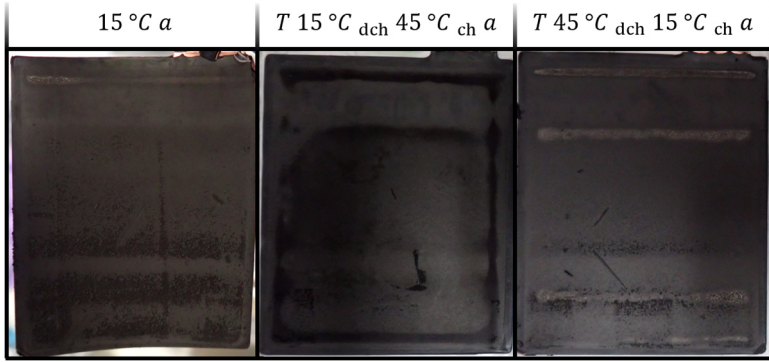


Figure 4.22: Pictures of negative electrode sheets of “L 1” after cycling at a homogeneous steady-state aging temperature of 15 °C (left) and homogeneous transient aging temperatures between 15 °C and 45 °C (middle and right).

For all negative electrode sheets, an imprint of the tapes of the outer separator or other inhomogeneities were visible. For the 15 °C homogeneous steady-state aging temperature, delamination of active material at the lower half of the negative electrode sheet was observed. Furthermore, there was some white cover layer at the top. This was similar for the cell with the 15 °C charging temperature and temperature change to 45 °C ($T\ 45\ ^\circ\text{C}_{\text{dch}}\ 15\ ^\circ\text{C}_{\text{ch}}\ a$) but the white cover layer was visible in more areas. The other transient cell $T\ 15\ ^\circ\text{C}_{\text{dch}}\ 45\ ^\circ\text{C}_{\text{ch}}\ a$ did not show strong delamination or cover layer formation but some color differences. This cell had experienced the smallest capacity loss.

For this cell, **mechanical effects** seem to be very important. Cracking and exfoliation of active material was a prominent aging mechanism observed by Laakso et al.[323] for a similar cell chemistry. Exfoliation and cover layer formation were only seen in certain areas of the cell geometry of the “L 1”. Cover layer formation in particular was only observed for the cells with predominantly charging at the lower temperature of 15 °C. Therefore, the onset of cover layer formation for transients at higher charging tempera-

tures could not be confirmed for the “L 1”. This could be related to the drastically decreased cell stack thickness of the “L 1” in comparison to the “L 3.4”. It seems possible that the temperature field during the temperature change is not as inhomogeneous for the “L 1”. This means that the cover layer formation which was assumed to be due to the inhomogeneous temperature field during the temperature change while charging[3] is geometry dependent and not relevant for all cells. However, the effect of the presence of alternating low and high aging temperatures has shown to accelerate the aging for this cell chemistry as well and is therefore likely independent of geometry as long as a lithium rich deposition is triggered.

All in all, thermal transients are of high interest as they can occur in real-life applications[20]. The influencing mechanisms and interrelation could be identified with these studies. However, exact predictions would not only require highly resolved thermal-electrical aging model but also mechanical modeling will become increasingly important for cells with silicon content. Furthermore, for the larger format cells, the modeling of other inhomogeneities such as the salt distribution could increase accuracy. This poses a very difficult task for predictions.

5 Conclusion

The operating window of LIB is crucial to their expected service life. Therefore, any significant stress-factors need to be taken into account. It is common knowledge that temperature is one of the most important stress-factors. However, literature is in part contradicting on the effect of complex thermal conditions on the cyclic aging behavior. This is related to the limited number of experimental investigations.

In this work, the effect of the stress-factors “inhomogeneous steady-state” and “homogeneous transient” aging temperature were looked at in more detail. The inhomogeneous steady-state temperature was investigated for two directionalities with regards to the electrode stack. In-plane and through-plane thermal gradients were previously suggested to have different impacts. Reference cyclic aging scenarios were chosen with the concept of equivalent aging temperature from literature and applied as a homogeneous steady-state aging temperature. The effect of the complex thermal boundary conditions on the global cyclic aging behavior was primarily judged by the capacity loss and resistance increase. On top, degradation mode analysis was performed to identify the main degradation modes. Furthermore, the local aging behavior was investigated to identify aging hot spots, and relate local aging mechanisms to the degradation modes and cell level capacity loss as well as resistance increase. To do so, both experimental methods and simulative methods were applied.

Cyclic aging tests were carefully designed for LIB of different formats and electrode chemistries. Other stress-factors than the aging temperature and charge throughput were initially kept constant. The complex temperature conditions were achieved with thermal plates on either side of the investigated pouch cells setting a temperature boundary condition. While it is experimentally challenging to get in-situ knowledge of the local aging states

during cyclic aging, a model prediction is possible. For this reason, a semi-empirical model extension was developed for an in-house electrical circuit network model (ECN) including a thermal model. The aging model was parameterized on the reference cyclic aging studies. Based on the analysis of the reference aging phenomena, the most relevant aging mechanisms for the modeling of thermal gradients were identified and implemented with a physically motivated modeling approach. Other aging mechanisms were parameterized fully empirically.

This holistic approach – on different scales and with experimental and simulative methods – was used to answer the research questions arising from literature:

- I. Storch et al.[47] suggested a suppression of gradients to be critical for a long lifetime of large format LIB. In their study, they found local lithium plating caused by a relation of temperature, current density and lithium concentration gradient.

Can this conclusion be confirmed and substantiated?

Yes. The conclusion can be confirmed and substantiated but needs to be addressed on different levels. These two levels are the general impact of the inhomogeneity on aging and their relevance in large-format cells. In this work, the general impact of a temperature inhomogeneity was judged by the capacity loss acceleration due to a defined temperature gradient. Therefore, the impact of the temperature gradient was investigated isolated in comparison to the study of Storch et al.[47]. Such an inhomogeneous steady-state temperature boundary condition caused a linear capacity loss acceleration of $8 - 25 \pm 4 \%$ in comparison to the homogeneous steady-state aging temperature reference for the investigated 20 Ah LIB. This is less than the acceleration of $153 \pm 8 \%$ by increasing the overall homogeneous steady-state aging temperature from 25 °C to 40 °C. However, with increasing requirements for the aging prediction, the acceleration due to the thermal inhomogeneities should be taken into account when defining the operating window.

This could be done in the following way. For the investigation on this 20 Ah cell with a cycling DoD of 100 % and inhomogeneous temperature fields, an easy approach was found to predict the capacity loss acceleration analytically before the capacity knee. Knowledge of the Arrhenius activation of the capacity decrease is required. Then, the capacity and charge throughput of the cell can be calculated as the sum of the capacities and charges of the cell segments at the local aging temperatures. The segmentation of the cell needs to be chosen with care depending on the cell geometry and boundary condition. This also suggest the calculation of a “new” reference temperature with means of an Arrhenius relation instead of a spatially and temporally average temperature. This approach neglects the capacity knee and was established for the dominating aging mechanism SEI growth. This finding is an essential addition to the hypotheses of Storch et al.[47] who only considered lithium plating as a main aging mechanism.

The presence of lithium plating is expected to alter the results and can be checked with an ECN including electrode potential splitting. This point needs to be stressed, because supplementary investigations with reduced DoD of 70 % and in-plane thermal gradients have shown increased capacity loss acceleration of $58 \% \pm 10 \%$. The model predicted potential lithium plating in the lower temperature region from the first cycle related to different current swapping behavior of the cell segments for the DoD 70 % case. This confirms parts of the suggested hypothesis of Storch et al.[47] that an inhomogeneous electrode potential causes inhomogeneous cell aging.

Regarding the cell format, a capacity loss acceleration in the order of 25 % was found for a 3 Ah cell with a superimposed in-plane thermal gradient from 0 °C to 50 °C as well as a 20 Ah cell with an in-plane thermal gradient from 10 °C to 40 °C. This is in line with the approach that the global aging is determined by the sum of the local aging. Even though the temperature gradient itself might not have different effects on different format cells with accurate temperature control, other relevant aging inhomogeneities were found in post-mortem analysis of the 20 Ah cell. These were potentially

related to salt inhomogeneity due to the larger format. That is why the statement by Storch et al.[47] can mostly be confirmed. However, such aging inhomogeneities are not limited to large formats and could also occur in smaller format cells during heavy-duty cycling.

II. Are through-plane thermal gradients worse than in-plane thermal gradients?

Yes and no. With regards to the capacity loss acceleration, different trends were observed for different temperature levels. A temperature difference from 10 °C to 40 °C yielded the same acceleration for a through-plane and in-plane thermal gradient. Nevertheless, additional aging mechanisms for the through-plane thermal gradient were found. These were more severe for higher temperature levels from 30 °C to 50 °C and not completely understood. At higher temperature levels, 30 °C to 50 °C a capacity loss acceleration for the through-plane thermal gradient in comparison to the in-plane thermal gradient was observed, indeed. One hypothesis on the different local aging behavior between in-plane and through-plane thermal gradients is based on the importance of the absolute local aging temperature. Possibly, maximum and minimum local temperature are different for in-plane and through-plane for the same externally applied temperature difference.

III. Why do thermal transients increase capacity loss during cyclic aging?

Only certain temperature changes can increase the capacity loss much more drastically than inhomogeneous steady-state aging temperature conditions. Temperature changes during cycling were found to be hazardous if the temperature changes themselves or the cycling condition triggers lithium rich cover layer formation on the negative electrode. Then, during subsequent higher temperatures, a reaction with electrolyte was suggested to be enhanced. The high number of cycles can reinforce this effect. The mechanism can be triggered because temperature changes during charging were found to cause cover layer formation even at higher aging temperatures for

some investigated cells. This was suggested to be related to the temporal change of the temperature field during charging.

Outlook

This work profoundly judged the importance of complex thermal stress-factors. Conclusive hypotheses on the interaction of local and global aging behavior were established and open ends were identified. Specifically, the interaction with other stress-factors during cyclic aging and the testing conditions are major challenges. For example, decreasing the DoD from 100 % to 70 % during cycling with inhomogeneous steady-state boundary conditions yielded a higher capacity loss acceleration. Other electrical stress-factors such as the current rate or the cycling profile might also alter the effect of these inhomogeneous temperature fields. Depending on the application, laboratory aging tests with CC-cycling have shown to overestimate the capacity loss in comparison to a commuter driving cycle including rest periods[322]. This is also related to the fact that resting during cycling can lead to recovery as was shown for some of the investigated cells. One possible explanation of this recovery effect was found in a rehomogenization of lithium distribution[180] which will be of interest when cycling with thermal gradients.

Two further aging mechanisms were found to interact with the complex thermal boundary conditions. The salt inhomogeneity in large format cells[311] was suggested to cause additional aging mechanisms in combination with a through-plane thermal gradient in large format cells. And, mechanical effects with silicon containing negative electrodes were suggested to become increasingly important in combination with thermal transients and need be taken into account.

This paragraph highlights the complexity of LIB aging and the ongoing need for research in this field. Particularly difficult will be modeling the interaction of all of these stress-factors with sufficient spatial resolution and physical fidelity.

References

- [1] L. Cloos, T. Wetzel, In-plane versus through-plane thermal gradients during cyclic aging of lithium-ion batteries – An experimental study, *Energy Technology* (2025). <https://doi.org/10.1002/ente.202402409>.
- [2] L. Cloos, J. Langer, M. Schiffler, A. Weber, Th. Wetzel, Challenges of Predicting Temperature Dependent Capacity Loss Using the Example of NMC-LMO Lithium-Ion Battery Cells, *J. Electrochem. Soc.* 171 (2024) 040538. <https://doi.org/10.1149/1945-7111/ad3ec3>.
- [3] L. Cloos, O. Queisser, A. Chahbaz, S. Paarmann, D.U. Sauer, T. Wetzel, Thermal Transients to Accelerate Cyclic Aging of Lithium-Ion Batteries, *Batteries & Supercaps* 7 (2024) e202300445. <https://doi.org/10.1002/batt.202300445>.
- [4] Bundesministerium für Wirtschaft und Klimaschutz, Klimaschutzplan 2050: Klimaschutzpolitische Grundsätze und Ziele der Bundesregierung, 2016.
- [5] K.P. Birke, ed., *Modern Battery Engineering: A Comprehensive Introduction*, World Scientific, 2019.
- [6] T. Placke, R. Klopsch, S. Dühnen, M. Winter, Lithium ion, lithium metal, and alternative rechargeable battery technologies: the odyssey for high energy density, *J Solid State Electrochem* 21 (2017) 1939–1964. <https://doi.org/10.1007/s10008-017-3610-7>.
- [7] A. Burkert, H. Fechtner, B. Schmuelling, Interdisciplinary Analysis of Social Acceptance Regarding Electric Vehicles with a Focus on Charging Infrastructure and Driving Range in Germany, *WEVJ* 12 (2021) 25. <https://doi.org/10.3390/wevj12010025>.
- [8] A. Barré, B. Deguilhem, S. Grolleau, M. Gérard, F. Suard, D. Riu, A review on lithium-ion battery ageing mechanisms and estimations for automotive applications, *Journal of Power Sources* 241 (2013) 680–689. <https://doi.org/10.1016/j.jpowsour.2013.05.040>.
- [9] X. Hu, L. Xu, X. Lin, M. Pecht, Battery Lifetime Prognostics, *Joule* 4 (2020) 310–346. <https://doi.org/10.1016/j.joule.2019.11.018>.
- [10] J. Gorzelany, By The Numbers: Comparing Electric Car Warranties, *Forbes* (2022).

- <https://www.forbes.com/sites/jimgorzalany/2022/10/31/by-the-numbers-comparing-electric-car-warranties/>.
- [11] T. Waldmann, M. Wilka, M. Kasper, M. Fleischhammer, M. Wohlfahrt-Mehrens, Temperature dependent ageing mechanisms in Lithium-ion batteries – A Post-Mortem study, *Journal of Power Sources* 262 (2014) 129–135.
<https://doi.org/10.1016/j.jpowsour.2014.03.112>.
- [12] M. Bozorgchenani, G. Kucinskis, M. Wohlfahrt-Mehrens, T. Waldmann, Experimental Confirmation of C-Rate Dependent Minima Shifts in Arrhenius Plots of Li-Ion Battery Aging, *J. Electrochem. Soc.* 169 (2022) 030509. <https://doi.org/10.1149/1945-7111/ac580d>.
- [13] G. Kucinskis, M. Bozorgchenani, M. Feinauer, M. Kasper, M. Wohlfahrt-Mehrens, T. Waldmann, Arrhenius plots for Li-ion battery ageing as a function of temperature, C-rate, and ageing state – An experimental study, *Journal of Power Sources* 549 (2022) 232129.
<https://doi.org/10.1016/j.jpowsour.2022.232129>.
- [14] X.-G. Yang, C.-Y. Wang, Understanding the trilemma of fast charging, energy density and cycle life of lithium-ion batteries, *Journal of Power Sources* 402 (2018) 489–498.
<https://doi.org/10.1016/j.jpowsour.2018.09.069>.
- [15] Y. Preger, H.M. Barkholtz, A. Fresquez, D.L. Campbell, B.W. Juba, J. Romàn-Kustas, S.R. Ferreira, B. Chalamala, Degradation of Commercial Lithium-Ion Cells as a Function of Chemistry and Cycling Conditions, *J. Electrochem. Soc.* 167 (2020) 120532.
<https://doi.org/10.1149/1945-7111/abae37>.
- [16] Y. Du, S. Shironita, E. Hosono, D. Asakura, Y. Sone, M. Umeda, Differences in the deterioration behaviors of fast-charged lithium-ion batteries at high and low temperatures, *Journal of Power Sources* 556 (2023) 232513.
<https://doi.org/10.1016/j.jpowsour.2022.232513>.
- [17] D. Werner, S. Paarmann, A. Wiebelt, T. Wetzel, Inhomogeneous Temperature Distribution Affecting the Cyclic Aging of Li-Ion Cells. Part II: Analysis and Correlation, *Batteries* 6 (2020) 12.
<https://doi.org/10.3390/batteries6010012>.
- [18] T. Grandjean, A. Barai, E. Hosseinzadeh, Y. Guo, A. McGordon, J. Marco, Large format lithium ion pouch cell full thermal characterisation for improved electric vehicle thermal management,

- Journal of Power Sources 359 (2017) 215–225.
<https://doi.org/10.1016/j.jpowsour.2017.05.016>.
- [19] T. Waldmann, G. Bisle, B.-I. Hogg, S. Stumpp, M.A. Danzer, M. Kasper, P. Axmann, M. Wohlfahrt-Mehrens, Influence of Cell Design on Temperatures and Temperature Gradients in Lithium-Ion Cells: An In Operando Study, *J. Electrochem. Soc.* 162 (2015) 921–927.
<https://doi.org/10.1149/2.0561506jes>.
- [20] S. Goutam, A. Nikolian, J. Jaguemont, J. Smekens, N. Omar, P. van Dan Bossche, J. van Mierlo, Three-dimensional electro-thermal model of li-ion pouch cell: Analysis and comparison of cell design factors and model assumptions, *Applied Thermal Engineering* 126 (2017) 796–808.
<https://doi.org/10.1016/j.applthermaleng.2017.07.206>.
- [21] A. Tourani, P. White, P. Ivey, Analysis of electric and thermal behaviour of lithium-ion cells in realistic driving cycles, *Journal of Power Sources* 268 (2014) 301–314.
<https://doi.org/10.1016/j.jpowsour.2014.06.010>.
- [22] J. Lin, H.N. Chu, D.A. Howey, C.W. Monroe, Multiscale coupling of surface temperature with solid diffusion in large lithium-ion pouch cells, *Commun Eng* 1 (2022) 107. <https://doi.org/10.1038/s44172-022-00005-8>.
- [23] I.A. Hunt, Y. Zhao, Y. Patel, J. Offer, Surface Cooling Causes Accelerated Degradation Compared to Tab Cooling for Lithium-Ion Pouch Cells, *J. Electrochem. Soc.* 163 (2016) 1846–1852.
<https://doi.org/10.1149/2.0361609jes>.
- [24] S. Li, N. Kirkaldy, C. Zhang, K. Gopalakrishnan, T. Amietszajew, L.B. Diaz, J.V. Barreras, M. Shams, X. Hua, Y. Patel, G.J. Offer, M. Marinescu, Optimal cell tab design and cooling strategy for cylindrical lithium-ion batteries, *Journal of Power Sources* 492 (2021) 229594. <https://doi.org/10.1016/j.jpowsour.2021.229594>.
- [25] M. Angeles Cabañero, J. Altmann, L. Gold, N. Boaretto, J. Müller, S. Hein, J. Zausch, J. Kallo, A. Latz, Investigation of the temperature dependence of lithium plating onset conditions in commercial Li-ion batteries, *Energy* 171 (2019) 1217–1228.
<https://doi.org/10.1016/j.energy.2019.01.017>.
- [26] R. Carter, E.J. Klein, T.A. Kingston, C.T. Love, Detection of Lithium Plating During Thermally Transient Charging of Li-Ion Batteries,

- Front. Energy Res. 7 (2019) 144.
<https://doi.org/10.3389/fenrg.2019.00144>.
- [27] H. Dai, Y. Xu, J. Zhu, Z. Sun, X. Wei, X. Wang, Preliminary Study on the Influence of Internal Temperature Gradient on EIS Measurement and Characterization for Li-Ion Batteries, in: 2015 IEEE Vehicle Power and Propulsion Conference (VPPC): Proceedings : 19-22 October 2015, Montréal, Quebec, IEEE, Piscataway, NJ, 2015: pp. 1–7.
<https://doi.org/10.1109/VPPC.2015.7352999>.
- [28] M. Klein, S. Tong, J.W. Park, In-plane nonuniform temperature effects on the performance of a large-format lithium-ion pouch cell, *Applied Energy* 165 (2016) 639–647.
<https://doi.org/10.1016/j.apenergy.2015.11.090>.
- [29] Y. Troxler, B. Wu, M. Marinescu, V. Yufit, Y. Patel, A.J. Marquis, N.P. Brandon, G.J. Offer, The effect of thermal gradients on the performance of lithium-ion batteries, *Journal of Power Sources* 247 (2014) 1018–1025. <https://doi.org/10.1016/j.jpowsour.2013.06.084>.
- [30] S. Paarmann, L. Cloos, J. Technau, T. Wetzel, Measurement of the Temperature Influence on the Current Distribution in Lithium-Ion Batteries, *Energy Technol.* 9 (2021) 2000862.
<https://doi.org/10.1002/ente.202000862>.
- [31] K. Rumpf, A. Rheinfeld, M. Schindler, J. Keil, T. Schua, A. Jossen, Influence of Cell-to-Cell Variations on the Inhomogeneity of Lithium-Ion Battery Modules, *Journal of The Electrochemical Society* (2018) 2587–2607.
- [32] X. Liu, W. Ai, M. Naylor Marlow, Y. Patel, B. Wu, The effect of cell-to-cell variations and thermal gradients on the performance and degradation of lithium-ion battery packs, *Applied Energy* 248 (2019) 489–499. <https://doi.org/10.1016/j.apenergy.2019.04.108>.
- [33] A. Fill, T. Mader, T. Schmidt, A. Avdyli, M. Kopp, K.P. Birke, Experimental investigations on current and temperature imbalances among parallel-connected lithium-ion cells at different thermal conditions, *Journal of Energy Storage* 51 (2022) 104325.
<https://doi.org/10.1016/j.est.2022.104325>.
- [34] M.P. Klein, J.W. Park, Current Distribution Measurements in Parallel-Connected Lithium-Ion Cylindrical Cells under Non-Uniform Temperature Conditions, *J. Electrochem. Soc.* 164 (2017) A1893–A1906. <https://doi.org/10.1149/2.0011709jes>.

-
- [35] C. Pastor-Fernández, T. Bruen, W.D. Widanage, M.A. Gama-Valdez, J. Marco, A Study of Cell-to-Cell Interactions and Degradation in Parallel Strings: Implications for the Battery Management System, *Journal of Power Sources* 329 (2016) 574–585. <https://doi.org/10.1016/j.jpowsour.2016.07.121>.
- [36] G. Zhang, C.E. Shaffer, C.-Y. Wang, C.D. Rahn, In-Situ Measurement of Current Distribution in a Li-Ion Cell, *J. Electrochem. Soc.* 160 (2013) 610–615. <https://doi.org/10.1149/2.046304jes>.
- [37] G. Zhang, C.E. Shaffer, C.-Y. Wang, C.D. Rahn, Effects of Non-Uniform Current Distribution on Energy Density of Li-Ion Cells, *J. Electrochem. Soc.* 160 (2013) 2299–2305. <https://doi.org/10.1149/2.061311jes>.
- [38] P.J. Osswald, S.V. Erhard, J. Wilhelm, H.E. Hoster, A. Jossen, Simulation and Measurement of Local Potentials of Modified Commercial Cylindrical Cells, *J. Electrochem. Soc.* 162 (2015) 2099–2105. <https://doi.org/10.1149/2.0561510jes>.
- [39] S.V. Erhard, P.J. Osswald, P. Keil, E. Höffer, M. Haug, A. Noel, J. Wilhelm, B. Rieger, K. Schmidt, S. Kosch, F.M. Kindermann, F. Spingler, H. Kloust, T. Thoennessen, A. Rheinfeld, A. Jossen, Simulation and Measurement of the Current Density Distribution in Lithium-Ion Batteries by a Multi-Tab Cell Approach, *J. Electrochem. Soc.* 164 (2017) 6324–6333. <https://doi.org/10.1149/2.0551701jes>.
- [40] J. Fleckenstein, O. Bohlen, B. Bäker, Aging Effect of Temperature Gradients in Li-ion Cells Experimental and Simulative Investigations and the Consequences on Thermal Battery Management, *World Electric Vehicle Journal* (2012).
- [41] J.B. Gerschler, F.N. Kirchhoff, H. Witzenhausen, F.E. Hust, D.U. Sauer, Spatially resolved model for lithium-ion batteries for identifying and analyzing influences of inhomogeneous stress inside the cells, in: 2009 IEEE Vehicle Power and Propulsion Conference, IEEE, 2009: pp. 295–303. <https://doi.org/10.1109/VPPC.2009.5289836>.
- [42] S. Li, C. Zhang, Y. Zhao, G.J. Offer, M. Marinescu, Effect of thermal gradients on inhomogeneous degradation in lithium-ion batteries, *Commun Eng* 2 (2023) 74. <https://doi.org/10.1038/s44172-023-00124-w>.
- [43] M. Naylor Marlow, J. Chen, B. Wu, Degradation in parallel-connected lithium-ion battery packs under thermal gradients, *Commun Eng* 3 (2024) 2. <https://doi.org/10.1038/s44172-023-00153-5>.

- [44] D. Werner, S. Paarmann, A. Wiebelt, T. Wetzel, Inhomogeneous Temperature Distribution Affecting the Cyclic Aging of Li-Ion Cells. Part I: Experimental Investigation, *Batteries* 6 (2020) 13. <https://doi.org/10.3390/batteries6010013>.
- [45] S. Paarmann, K. Schuld, T. Wetzel, Inhomogeneous Aging in Lithium-Ion Batteries Caused by Temperature Effects, *Energy Tech* 10 (2022) 2200384. <https://doi.org/10.1002/ente.202200384>.
- [46] W. Chang, C. Bommier, T. Fair, J. Yeung, S. Patil, D. Steingart, Understanding Adverse Effects of Temperature Shifts on Li-Ion Batteries: An Operando Acoustic Study, *J. Electrochem. Soc.* 167 (2020) 090503. <https://doi.org/10.1149/1945-7111/ab6c56>.
- [47] M. Storch, J.P. Fath, J. Sieg, D. Vrankovic, C. Krupp, B. Spier, R. Riedel, Temperature and Lithium Concentration Gradient Caused Inhomogeneous Plating in Large-format Lithium-ion Cells, *Journal of Energy Storage* 41 (2021) 102887. <https://doi.org/10.1016/j.est.2021.102887>.
- [48] R. Carter, T.A. Kingston, R.W. Atkinson, M. Parmananda, M. Dubarry, C. Fear, P.P. Mukherjee, C.T. Love, Directionality of thermal gradients in lithium-ion batteries dictates diverging degradation modes, *Cell Reports Physical Science* 2 (2021) 100351. <https://doi.org/10.1016/j.xcrp.2021.100351>.
- [49] A. Tomaszewska, Z. Chu, X. Feng, S. O’Kane, X. Liu, J. Chen, C. Ji, E. Endler, R. Li, L. Liu, Y. Li, S. Zheng, S. Vetterlein, M. Gao, J. Du, M. Parkes, M. Ouyang, M. Marinescu, G. Offer, B. Wu, Lithium-ion battery fast charging: A review, *eTransportation* 1 (2019) 100011. <https://doi.org/10.1016/j.etrans.2019.100011>.
- [50] M. Broussely, Ph. Biensan, F. Bonhomme, Ph. Blanchard, S. Herreyre, K. Nechev, R.J. Staniewicz, Main aging mechanisms in Li ion batteries, *Journal of Power Sources* (2005) 90–96.
- [51] R. Korthauer, *Lithium-Ion Batteries: Basics and Applications*, Springer Berlin Heidelberg, Berlin, Heidelberg, 2018. <https://doi.org/10.1007/978-3-662-53071-9>.
- [52] C.R. Birkel, M.R. Roberts, E. McTurk, P.G. Bruce, D.A. Howey, Degradation diagnostics for lithium ion cells, *Journal of Power Sources* 341 (2017) 373–386. <https://doi.org/10.1016/j.jpowsour.2016.12.011>.
- [53] A. Börger, H. Wenzl, *Batterien: Grundlagen, Systeme, Anwendungen*, Wiley-VCH, Weinheim, 2023.

- [54] J. Vetter, P. Novák, M.R. Wagner, C. Veit, K.-C. Möller, J.O. Besenhard, M. Winter, M. Wohlfahrt-Mehrens, C. Vogler, A. Hammouche, Ageing mechanisms in lithium-ion batteries, *Journal of Power Sources* 147 (2005) 269–281. <https://doi.org/10.1016/j.jpowsour.2005.01.006>.
- [55] M. Wohlfahrt-Mehrens, C. Vogler, J. Garche, Aging mechanisms of lithium cathode materials, *Journal of Power Sources* 127 (2004) 58–64. <https://doi.org/10.1016/j.jpowsour.2003.09.034>.
- [56] A.M. Andersson, D.P. Abraham, R. Haasch, S. MacLaren, J. Liu, K. Amine, Surface Characterization of Electrodes from High Power Lithium-Ion Batteries, *J. Electrochem. Soc.* 149 (2002) A1358. <https://doi.org/10.1149/1.1505636>.
- [57] S. Venkatraman, Y. Shin, A. Manthiram, Phase Relationships and Structural and Chemical Stabilities of Charged $\text{Li}_{1-x}\text{CoO}_{2-\delta}$ and $\text{Li}_{1-x}\text{Ni}_{0.85}\text{Co}_{0.15}\text{O}_{2-\delta}$ Cathodes, *Electrochem. Solid-State Lett.* 6 (2003) A9. <https://doi.org/10.1149/1.1525430>.
- [58] D.P. Abraham, R.D. Twisten, M. Balasubramanian, I. Petrov, J. McBreen, K. Amine, Surface changes on $\text{LiNi}_{0.8}\text{Co}_{0.2}\text{O}_2$ particles during testing of high-power lithium-ion cells, *Electrochemistry Communications* 4 (2002) 620–625. [https://doi.org/10.1016/S1388-2481\(02\)00388-0](https://doi.org/10.1016/S1388-2481(02)00388-0).
- [59] S. Jung, H. Gwon, J. Hong, K. Park, D. Seo, H. Kim, J. Hyun, W. Yang, K. Kang, Understanding the Degradation Mechanisms of $\text{LiNi}_{0.5}\text{Co}_{0.2}\text{Mn}_{0.3}\text{O}_2$ Cathode Material in Lithium Ion Batteries, *Advanced Energy Materials* 4 (2014) 1300787. <https://doi.org/10.1002/aenm.201300787>.
- [60] Q. Xie, Z. Cui, A. Manthiram, Unveiling the Stabilities of Nickel-Based Layered Oxide Cathodes at an Identical Degree of Delithiation in Lithium-Based Batteries, *Adv Mater* 33 (2021) 2100804. <https://doi.org/10.1002/adma.202100804>.
- [61] F. Schipper, E.M. Erickson, C. Erk, J.-Y. Shin, F.F. Chesneau, D. Aurbach, Review—Recent Advances and Remaining Challenges for Lithium Ion Battery Cathodes: I. Nickel-Rich, $\text{LiNi}_x\text{Co}_y\text{Mn}_z\text{O}_2$, *J. Electrochem. Soc.* 164 (2017) A6220–A6228. <https://doi.org/10.1149/2.0351701jes>.
- [62] N.Y. Kim, T. Yim, J.H. Song, J.-S. Yu, Z. Lee, Microstructural study on degradation mechanism of layered $\text{LiNi}_{0.6}\text{Co}_{0.2}\text{Mn}_{0.2}\text{O}_2$ cathode

- materials by analytical transmission electron microscopy, *Journal of Power Sources* 307 (2016) 641–648.
<https://doi.org/10.1016/j.jpowsour.2016.01.023>.
- [63] J. Morales, C. Pérez-Vicente, J.L. Tirado, Cation distribution and chemical deintercalation of $\text{Li}_{1-x}\text{Ni}_1+x\text{O}_2$, *Materials Research Bulletin* 25 (1990) 623–630. [https://doi.org/10.1016/0025-5408\(90\)90028-Z](https://doi.org/10.1016/0025-5408(90)90028-Z).
- [64] K.-W. Nam, W.-S. Yoon, H. Shin, K.Y. Chung, S. Choi, X.-Q. Yang, In situ X-ray diffraction studies of mixed LiMn_2O_4 – $\text{LiNi}_{1/3}\text{Co}_{1/3}\text{Mn}_{1/3}\text{O}_2$ composite cathode in Li-ion cells during charge–discharge cycling, *Journal of Power Sources* 192 (2009) 652–659. <https://doi.org/10.1016/j.jpowsour.2009.02.088>.
- [65] R.J. Gummow, A. De Kock, M.M. Thackeray, Improved capacity retention in rechargeable 4 V lithium/lithium-manganese oxide (spinel) cells, *Solid State Ionics* 69 (1994) 59–67. [https://doi.org/10.1016/0167-2738\(94\)90450-2](https://doi.org/10.1016/0167-2738(94)90450-2).
- [66] M.M. Thackeray, Structural Fatigue in Spinel Electrodes in High Voltage (4 V) $\text{Li}/\text{Li}_{[x]}\text{Mn}_{[2]}\text{O}_{[4]}$ Cells, *Electrochem. Solid-State Lett.* 1 (1999) 7. <https://doi.org/10.1149/1.1390617>.
- [67] Y. Xia, Y. Zhou, M. Yoshio, Capacity Fading on Cycling of 4 V $\text{Li}/\text{LiMn}_2\text{O}_4$ Cells, *J. Electrochem. Soc.* 144 (1997) 2593–2600. <https://doi.org/10.1149/1.1837870>.
- [68] J.M. Tarascon, W.R. McKinnon, F. Coowar, T.N. Bowmer, G. Amatucci, D. Guyomard, Synthesis Conditions and Oxygen Stoichiometry Effects on Li Insertion into the Spinel LiMn_2O_4 , *J. Electrochem. Soc.* 141 (1994) 1421–1431. <https://doi.org/10.1149/1.2054941>.
- [69] D.H. Jang, Y.J. Shin, S.M. Oh, Dissolution of Spinel Oxides and Capacity Losses in 4 V $\text{Li}/\text{Li}_x\text{Mn}_2\text{O}_4$ Cells, *J. Electrochem. Soc.* 143 (1996) 2204–2211. <https://doi.org/10.1149/1.1836981>.
- [70] Y. Gao, J.R. Dahn, Correlation between the growth of the 3.3 V discharge plateau and capacity fading in $\text{Li}_{1-x}\text{Mn}_2-x\text{O}_4$ materials, *Solid State Ionics* 84 (1996) 33–40. [https://doi.org/10.1016/S0167-2738\(96\)83003-7](https://doi.org/10.1016/S0167-2738(96)83003-7).
- [71] D. Aurbach, K. Gamolsky, B. Markovsky, G. Salitra, Y. Gofer, U. Heider, R. Oesten, M. Schmidt, The Study of Surface Phenomena Related to Electrochemical Lithium Intercalation into Li_xMO_y Host

- Materials (M5 = Ni, Mn), *Journal of The Electrochemical Society* (2000).
- [72] K. Edström, T. Gustafsson, J.O. Thomas, The cathode–electrolyte interface in the Li-ion battery, *Electrochimica Acta* 50 (2004) 397–403. <https://doi.org/10.1016/j.electacta.2004.03.049>.
- [73] Sungjemmenla, V. S. K., C.B. Soni, V. Kumar, Z.W. Seh, Understanding the Cathode–Electrolyte Interphase in Lithium-Ion Batteries, *Energy Tech* 10 (2022) 2200421. <https://doi.org/10.1002/ente.202200421>.
- [74] J.C. Stallard, L. Wheatcroft, S.G. Booth, R. Boston, S.A. Corr, M.F.L. De Volder, B.J. Inkson, N.A. Fleck, Mechanical properties of cathode materials for lithium-ion batteries, *Joule* 6 (2022) 984–1007. <https://doi.org/10.1016/j.joule.2022.04.001>.
- [75] P. Yan, J. Zheng, M. Gu, J. Xiao, J.-G. Zhang, C.-M. Wang, Intragranular cracking as a critical barrier for high-voltage usage of layer-structured cathode for lithium-ion batteries, *Nat Commun* 8 (2017) 14101. <https://doi.org/10.1038/ncomms14101>.
- [76] S. Lee, L. Su, A. Mesnier, Z. Cui, A. Manthiram, Cracking vs. surface reactivity in high-nickel cathodes for lithium-ion batteries, *Joule* 7 (2023) 2430–2444. <https://doi.org/10.1016/j.joule.2023.09.006>.
- [77] W.J. Weydanz, M. Wohlfahrt-Mehrens, R.A. Huggins, A room temperature study of the binary lithium–silicon and the ternary lithium–chromium–silicon system for use in rechargeable lithium batteries, *Journal of Power Sources* 81–82 (1999) 237–242. [https://doi.org/10.1016/S0378-7753\(99\)00139-1](https://doi.org/10.1016/S0378-7753(99)00139-1).
- [78] B.A. Boukamp, G.C. Lesh, R.A. Huggins, All-Solid Lithium Electrodes with Mixed-Conductor Matrix, *J. Electrochem. Soc.* 128 (1981) 725–729. <https://doi.org/10.1149/1.2127495>.
- [79] Y. Wang, Y. Liu, J. Zheng, H. Zheng, Z. Mei, X. Du, H. Li, Electrochemical performances and volume variation of nano-textured silicon thin films as anodes for lithium-ion batteries, *Nanotechnology* 24 (2013) 424011. <https://doi.org/10.1088/0957-4484/24/42/424011>.
- [80] D. Goers, M.E. Spahr, A. Leone, W. Märkle, P. Novák, The influence of the local current density on the electrochemical exfoliation of graphite in lithium-ion battery negative electrodes, *Electrochimica Acta* 56 (2011) 3799–3808. <https://doi.org/10.1016/j.electacta.2011.02.046>.

- [81] T. Abe, N. Kawabata, Y. Mizutani, M. Inaba, Z. Ogumi, Correlation Between Cointercalation of Solvents and Electrochemical Intercalation of Lithium into Graphite in Propylene Carbonate Solution, *J. Electrochem. Soc.* 150 (2003) A257. <https://doi.org/10.1149/1.1541004>.
- [82] A.N. Dey, B.P. Sullivan, The Electrochemical Decomposition of Propylene Carbonate on Graphite, *J. Electrochem. Soc.* 117 (1970) 222. <https://doi.org/10.1149/1.2407470>.
- [83] R. Imhof, P. Novák, In Situ Investigation of the Electrochemical Reduction of Carbonate Electrolyte Solutions at Graphite Electrodes, *J. Electrochem. Soc.* 145 (1998) 1081–1087. <https://doi.org/10.1149/1.1838420>.
- [84] J.A. Gilbert, I.A. Shkrob, D.P. Abraham, Transition Metal Dissolution, Ion Migration, Electrocatalytic Reduction and Capacity Loss in Lithium-Ion Full Cells, *J. Electrochem. Soc.* 164 (2017) 389–399. <https://doi.org/10.1149/2.1111702jes>.
- [85] G. Amatucci, Cobalt dissolution in LiCoO₂-based non-aqueous rechargeable batteries, *Solid State Ionics* 83 (1996) 167–173. [https://doi.org/10.1016/0167-2738\(95\)00231-6](https://doi.org/10.1016/0167-2738(95)00231-6).
- [86] Y. Tesfamhret, H. Liu, Z. Chai, E. Berg, R. Younesi, On the Manganese Dissolution Process from LiMn₂O₄ Cathode Materials, *ChemElectroChem* (2021) 1516–1523.
- [87] M.S.D. Darma, M. Lang, K. Kleiner, L. Mereacre, V. Liebau, F. Fauth, T. Bergfeldt, H. Ehrenberg, The influence of cycling temperature and cycling rate on the phase specific degradation of a positive electrode in lithium ion batteries: A post mortem analysis, *Journal of Power Sources* 327 (2016) 714–725. <https://doi.org/10.1016/j.jpowsour.2016.07.115>.
- [88] M. Lang, M.S.D. Darma, K. Kleiner, L. Riekehr, L. Mereacre, M. Ávila Pérez, V. Liebau, H. Ehrenberg, Post mortem analysis of fatigue mechanisms in LiNi_{0.8}Co_{0.15}Al_{0.05}O₂ – LiNi_{0.5}Co_{0.2}Mn_{0.3}O₂ – LiMn₂O₄/graphite lithium ion batteries, *Journal of Power Sources* 326 (2016) 397–409. <https://doi.org/10.1016/j.jpowsour.2016.07.010>.
- [89] E. Björklund, C. Xu, W.M. Dose, C.G. Sole, P.K. Thakur, T.-L. Lee, M.F.L. De Volder, C.P. Grey, R.S. Weatherup, Cycle-Induced Interfacial Degradation and Transition-Metal Cross-Over in LiNi_{0.8}

- Mn_{0.1}Co_{0.1}O₂–Graphite Cells, *Chem. Mater.* 34 (2022) 2034–2048. <https://doi.org/10.1021/acs.chemmater.1c02722>.
- [90] W. Li, X. Liu, Q. Xie, Y. You, M. Chi, A. Manthiram, Long-Term Cyclability of NCM-811 at High Voltages in Lithium-Ion Batteries: an In-Depth Diagnostic Study, *Chem. Mater.* 32 (2020) 7796–7804. <https://doi.org/10.1021/acs.chemmater.0c02398>.
- [91] J. Kasnatscheew, S. Röser, M. Börner, M. Winter, Do Increased Ni Contents in LiNi_xMn_yCo_zO₂ (NMC) Electrodes Decrease Structural and Thermal Stability of Li Ion Batteries? A Thorough Look by Consideration of the Li + Extraction Ratio, *ACS Appl. Energy Mater.* 2 (2019) 7733–7737. <https://doi.org/10.1021/acsaem.9b01440>.
- [92] R. Hausbrand, G. Cherkashinin, H. Ehrenberg, M. Gröting, K. Albe, C. Hess, W. Jaegermann, Fundamental degradation mechanisms of layered oxide Li-ion battery cathode materials: Methodology, insights and novel approaches, *Materials Science and Engineering: B* 192 (2015) 3–25. <https://doi.org/10.1016/j.mseb.2014.11.014>.
- [93] H. Tsunekawa, a. S. Tanimoto, R. Marubayashi, M. Fujita, K. Kifune, M. Sano, Capacity Fading of Graphite Electrodes Due to the Deposition of Manganese Ions on Them in Li-Ion Batteries, *J. Electrochem. Soc.* 149 (2002) 1326. <https://doi.org/10.1149/1.1502686>.
- [94] G. Amatucci, A. Du Pasquier, A. Blyr, T. Zheng, J.-M. Tarascon, The elevated temperature performance of the LiMn₂O₄/C system: failure and solutions, *Electrochimica Acta* 45 (1999) 255–271. [https://doi.org/10.1016/S0013-4686\(99\)00209-1](https://doi.org/10.1016/S0013-4686(99)00209-1).
- [95] C. Zhan, J. Lu, A. Jeremy Kropf, T. Wu, A.N. Jansen, Y.-K. Sun, X. Qiu, K. Amine, Mn(II) deposition on anodes and its effects on capacity fade in spinel lithium manganate-carbon systems, *Nat Commun* 4 (2013) 2437. <https://doi.org/10.1038/ncomms3437>.
- [96] K. Amine, J. Liu, S. Kang, I. Belharouak, Y. Hyung, D. Vissers, G. Henriksen, Improved lithium manganese oxide spinel/graphite Li-ion cells for high-power applications, *Journal of Power Sources* 129 (2004) 14–19. <https://doi.org/10.1016/j.jpowsour.2003.11.007>.
- [97] E. Peled, S. Menkin, Review—SEI: Past, Present and Future, *J. Electrochem. Soc.* 164 (2017) 1703–1719. <https://doi.org/10.1149/2.1441707jes>.

- [98] P. Verma, P. Maire, P. Novák, A review of the features and analyses of the solid electrolyte interphase in Li-ion batteries, *Electrochimica Acta* 55 (2010) 6332–6341. <https://doi.org/10.1016/j.electacta.2010.05.072>.
- [99] Y. Qian, S. Hu, X. Zou, Z. Deng, Y. Xu, Z. Cao, Y. Kang, Y. Deng, Q. Shi, K. Xu, Y. Deng, How electrolyte additives work in Li-ion batteries, *Energy Storage Materials* 20 (2019) 208–215. <https://doi.org/10.1016/j.ensm.2018.11.015>.
- [100] L. Kolzenberg, A. Latz, B. Horstmann, Solid-Electrolyte Interphase During Battery Cycling: Theory of Growth Regimes, *ChemSusChem* 13 (2020) 3901–10. <https://doi.org/10.1002/cssc.202000867>.
- [101] R. Li, S. O’Kane, M. Marinescu, G.J. Offer, Modelling Solvent Consumption from SEI Layer Growth in Lithium-Ion Batteries, *J. Electrochem. Soc.* 169 (2022) 060516. <https://doi.org/10.1149/1945-7111/ac6f84>.
- [102] Yao. Wu, P. Keil, S.F. Schuster, Andreas. Jossen, Impact of Temperature and Discharge Rate on the Aging of a LiCoO₂/LiNi_{0.8}Co_{0.15}Al_{0.05}O₂ Lithium-Ion Pouch Cell, *J. Electrochem. Soc.* (2017) 1438–1445.
- [103] N. Ghanbari, T. Waldmann, M. Kasper, P. Axmann, M. Wohlfahrt-Mehrens, Inhomogeneous Degradation of Graphite Anodes in Li-Ion Cells: A Postmortem Study Using Glow Discharge Optical Emission Spectroscopy (GD-OES), *J. Phys. Chem. C* 120 (2016) 22225–22234. <https://doi.org/10.1021/acs.jpcc.6b07117>.
- [104] K. Amine, C.H. Chen, J. Liu, M. Hammond, A. Jansen, D. Dees, I. Bloom, D. Vissers, G. Henriksen, Factors responsible for impedance rise in high power lithium ion batteries, *Journal of Power Sources* (2001).
- [105] N.R. Avery, K.J. Black, Kinetic analysis of capacity fade in lithium/coke half-cells, *Journal of Power Sources* 68 (1997) 191–194. [https://doi.org/10.1016/S0378-7753\(96\)02550-5](https://doi.org/10.1016/S0378-7753(96)02550-5).
- [106] S.S. Zhang, K. Xu, T.R. Jow, Optimization of the forming conditions of the solid-state interface in the Li-ion batteries, *Journal of Power Sources* 130 (2004) 281–285. <https://doi.org/10.1016/j.jpowsour.2003.12.012>.
- [107] P. Ramadass, B. Haran, R. White, B.N. Popov, Capacity fade of Sony 18650 cells cycled at elevated temperatures, *Journal of Power*

- Sources 112 (2002) 614–620. [https://doi.org/10.1016/S0378-7753\(02\)00473-1](https://doi.org/10.1016/S0378-7753(02)00473-1).
- [108] P.M. Attia, S. Das, S.J. Harris, M.Z. Bazant, W.C. Chueh, Electrochemical Kinetics of SEI Growth on Carbon Black: Part I. Experiments, *J. Electrochem. Soc.* 166 (2019) 97–106. <https://doi.org/10.1149/2.0231904jes>.
- [109] H.-p. Lin, D. Chua, M. Salomon, H.-C. Shiao, M. Hendrickson, E. Plichta, S. Slane, Low-Temperature Behavior of Li-Ion Cells, *Electrochem. Solid-State Lett.* 4 (2001) 71. <https://doi.org/10.1149/1.1368736>.
- [110] C. Fear, M. Parmananda, V. Kabra, R. Carter, C.T. Love, P.P. Mukherjee, Mechanistic underpinnings of thermal gradient induced inhomogeneity in lithium plating, *Energy Storage Materials* 35 (2021) 500–511. <https://doi.org/10.1016/j.ensm.2020.11.029>.
- [111] T. Waldmann, B.-I. Hogg, M. Wohlfahrt-Mehrens, Li plating as unwanted side reaction in commercial Li-ion cells – A review, *Journal of Power Sources* 384 (2018) 107–124. <https://doi.org/10.1016/j.jpowsour.2018.02.063>.
- [112] P. Arora, M. Doyle, R.E. White, Mathematical Modeling of the Lithium Deposition Overcharge Reaction in Lithium-Ion Batteries Using Carbon-Based Negative Electrodes, *J. Electrochem. Soc.* 146 (1999) 3543–3553. <https://doi.org/10.1149/1.1392512>.
- [113] P. Bai, J. Li, F.R. Brushett, M.Z. Bazant, Transition of lithium growth mechanisms in liquid electrolytes, *Energy Environ. Sci.* 9 (2016) 3221–3229. <https://doi.org/10.1039/C6EE01674J>.
- [114] T. Gao, Y. Han, D. Fraggadakis, S. Das, T. Zhou, C.-N. Yeh, S. Xu, W.C. Chueh, J. Li, M.Z. Bazant, Interplay of Lithium Intercalation and Plating on a Single Graphite Particle, *Joule* 5 (2021) 393–414. <https://doi.org/10.1016/j.joule.2020.12.020>.
- [115] N. Legrand, B. Knosp, P. Desprez, F. Lapique, S. Raël, Physical characterization of the charging process of a Li-ion battery and prediction of Li plating by electrochemical modelling, *Journal of Power Sources* 245 (2014) 208–216. <https://doi.org/10.1016/j.jpowsour.2013.06.130>.
- [116] P. Bai, J. Guo, M. Wang, A. Kushima, L. Su, J. Li, F.R. Brushett, M.Z. Bazant, Interactions between Lithium Growths and Nanoporous Ceramic Separators, *Joule* 2 (2018) 2434–2449. <https://doi.org/10.1016/j.joule.2018.08.018>.

- [117] M. Petzl, M.A. Danzer, Nondestructive detection, characterization, and quantification of lithium plating in commercial lithium-ion batteries, *Journal of Power Sources* 254 (2014) 80–87. <https://doi.org/10.1016/j.jpowsour.2013.12.060>.
- [118] R.V. Bugga, M.C. Smart, Lithium Plating Behavior in Lithium-Ion Cells, *ECS Trans.* 25 (2010) 241–252. <https://doi.org/10.1149/1.3393860>.
- [119] I. Yoshimatsu, T. Hirai, J. Yamaki, Lithium Electrode Morphology during Cycling in Lithium Cells, *J. Electrochem. Soc.* 135 (1988) 2422–2427. <https://doi.org/10.1149/1.2095351>.
- [120] E. Peled, The Electrochemical Behavior of Alkali and Alkaline Earth Metals in Nonaqueous Battery Systems—The Solid Electrolyte Interphase Model, *J. Electrochem. Soc.* 126 (1979) 2047–2051. <https://doi.org/10.1149/1.2128859>.
- [121] G. Zhang, X. Wei, G. Han, H. Dai, J. Zhu, X. Wang, X. Tang, J. Ye, Lithium plating on the anode for lithium-ion batteries during long-term low temperature cycling, *Journal of Power Sources* 484 (2021) 229312. <https://doi.org/10.1016/j.jpowsour.2020.229312>.
- [122] T. Waldmann, A. Iturrondobeitia, M. Kasper, N. Ghanbari, F. Aguesse, E. Bekaert, L. Daniel, S. Genies, I.J. Gordon, M.W. Löble, E. Vito, M. Wohlfahrt-Mehrens, Review—Post-Mortem Analysis of Aged Lithium-Ion Batteries: Disassembly Methodology and Physico-Chemical Analysis Techniques, *J. Electrochem. Soc.* 163 (2016) 2149–2164. <https://doi.org/10.1149/2.1211609jes>.
- [123] M. Lewerenz, A. Warnecke, D.U. Sauer, Post-mortem analysis on LiFePO₄|Graphite cells describing the evolution & composition of covering layer on anode and their impact on cell performance, *Journal of Power Sources* 369 (2017) 122–132. <https://doi.org/10.1016/j.jpowsour.2017.10.003>.
- [124] S.J. Harris, A. Timmons, D.R. Baker, C. Monroe, Direct in situ measurements of Li transport in Li-ion battery negative electrodes, *Chemical Physics Letters* 485 (2010) 265–274. <https://doi.org/10.1016/j.cplett.2009.12.033>.
- [125] S. Wu, P.-H. Lee, Storage fading of a commercial 18650 cell comprised with NMC/LMO cathode and graphite anode, *Journal of Power Sources* 349 (2017) 27–36. <https://doi.org/10.1016/j.jpowsour.2017.03.002>.
- [126] Y. Kobayashi, T. Kobayashi, K. Shono, Y. Ohno, Y. Mita, H. Miyashiro, Decrease in Capacity in Mn-Based/Graphite Commercial Lithium-Ion

- Batteries, *J. Electrochem. Soc.* 160 (2013) 1181–1186.
<https://doi.org/10.1149/2.071308jes>.
- [127] L. Bodenes, R. Dedryvère, H. Martinez, F. Fischer, C. Tessier, J.-P. Pérès, Lithium-Ion Batteries Working at 85°C: Aging Phenomena and Electrode/Electrolyte Interfaces Studied by XPS, *J. Electrochem. Soc.* 159 (2012) A1739–A1746. <https://doi.org/10.1149/2.061210jes>.
- [128] V.A. Godbole, J.-F. Colin, P. Novák, Study of Overcharge Behavior of $\text{Li}_{1+x}(\text{Ni}_{1/3}\text{Mn}_{1/3}\text{Co}_{1/3})_{1-x}\text{O}_2$ Using In Situ and Ex Situ X-ray Synchrotron Diffraction, *J. Electrochem. Soc.* 158 (2011) 1005.
<https://doi.org/10.1149/1.3607982>.
- [129] M. Dubarry, V. Svoboda, R. Hwu, B. Yann Liaw, Incremental Capacity Analysis and Close-to-Equilibrium OCV Measurements to Quantify Capacity Fade in Commercial Rechargeable Lithium Batteries, *Electrochem. Solid-State Lett.* 9 (2006) 454.
<https://doi.org/10.1149/1.2221767>.
- [130] I. Bloom, A.N. Jansen, D.P. Abraham, J. Knuth, S.A. Jones, V.S. Battaglia, G.L. Henriksen, Differential voltage analyses of high-power lithium-ion cells 1. Technique and application, *Journal of Power Sources* 139 (2004) 295.
- [131] J. Schmitt, M. Schindler, A. Oberbauer, A. Jossen, Determination of degradation modes of lithium-ion batteries considering aging-induced changes in the half-cell open-circuit potential curve of silicon–graphite, *Journal of Power Sources* 532 (2022) 231296.
<https://doi.org/10.1016/j.jpowsour.2022.231296>.
- [132] M. Dubarry, B.Y. Liaw, Identify capacity fading mechanism in a commercial LiFePO_4 cell, *Journal of Power Sources* 194 (2009) 541–549. <https://doi.org/10.1016/j.jpowsour.2009.05.036>.
- [133] I. Bloom, J. Christophersen, K. Gering, Differential voltage analyses of high-power lithium-ion cells 2. Applications, *Journal of Power Sources* 139 (2005) 304–313.
<https://doi.org/10.1016/j.jpowsour.2004.07.022>.
- [134] M. Dubarry, D. Anseán, Best practices for incremental capacity analysis, *Front. Energy Res.* 10 (2022).
<https://doi.org/10.3389/fenrg.2022.1023555>.
- [135] W. Weppner, R.A. Huggins, Determination of the Kinetic Parameters of Mixed-Conducting Electrodes and Application to the System Li_3Sb , *J. Electrochem. Soc.* 124 (1977) 1569–1578.
<https://doi.org/10.1149/1.2133112>.

- [136] P. Kurzweil, *Angewandte Elektrochemie: Grundlagen, Messtechnik, Elektroanalytik, Energiewandlung, technische Verfahren*, Springer Fachmedien Wiesbaden, Wiesbaden, 2020.
<https://doi.org/10.1007/978-3-658-32421-6>.
- [137] J.E.B. Randles, Kinetics of rapid electrode reactions, *Discuss. Faraday Soc.* 1 (1947) 11. <https://doi.org/10.1039/df9470100011>.
- [138] P. Baudry, M. Neri, M. Gueguen, G. Lonchamp, Electro-thermal modelling of polymer lithium batteries for starting period and pulse power, *Journal of Power Sources* 54 (1995) 393–396.
[https://doi.org/10.1016/0378-7753\(94\)02109-G](https://doi.org/10.1016/0378-7753(94)02109-G).
- [139] S. Gantenbein, M. Weiss, E. Ivers-Tiffée, Impedance based time-domain modeling of lithium-ion batteries: Part I, *Journal of Power Sources* 379 (2018) 317–327.
<https://doi.org/10.1016/j.jpowsour.2018.01.043>.
- [140] D. Aurbach, B. Markovsky, M.D. Levi, E. Levi, A. Schechter, M. Moshkovich, Y. Cohen, New insights into the interactions between electrode materials and electrolyte solutions for advanced nonaqueous batteries, *Journal of Power Sources* 81–82 (1999) 95–111. [https://doi.org/10.1016/S0378-7753\(99\)00187-1](https://doi.org/10.1016/S0378-7753(99)00187-1).
- [141] M.D. Levi, K. Gamolsky, D. Aurbach, U. Heider, R. Oesten, On electrochemical impedance measurements of $\text{Li}_x\text{Co}_0.2\text{Ni}_0.8\text{O}_2$ and Li_xNiO_2 intercalation electrodes, *Electrochimica Acta* 45 (2000) 1781–1789. [https://doi.org/10.1016/S0013-4686\(99\)00402-8](https://doi.org/10.1016/S0013-4686(99)00402-8).
- [142] M.D. Levi, D. Aurbach, Diffusion Coefficients of Lithium Ions during Intercalation into Graphite Derived from the Simultaneous Measurements and Modeling of Electrochemical Impedance and Potentiostatic Intermittent Titration Characteristics of Thin Graphite Electrodes, *J. Phys. Chem. B* 101 (1997) 4641–4647.
<https://doi.org/10.1021/jp9701911>.
- [143] T. Jacobsen, K. West, Diffusion impedance in planar, cylindrical and spherical symmetry, *Electrochimica Acta* 40 (1995) 255–262.
[https://doi.org/10.1016/0013-4686\(94\)E0192-3](https://doi.org/10.1016/0013-4686(94)E0192-3).
- [144] J. Illig, M. Ender, T. Chrobak, J.P. Schmidt, D. Klotz, E. Ivers-Tiffée, Separation of Charge Transfer and Contact Resistance in LiFePO_4 Cathodes by Impedance Modeling, *J. Electrochem. Soc.* 159 (2012) 952–960.
- [145] S. Buller, *Impedance-Based Simulation Models for Energy Storage Devices in Advanced Automotive Power Systems*, 2009.

- [146] T. Handschuh, Untersuchung des Betriebs und Alterungsverhaltens von Blei-Säure-Akkumulatoren bei für Hybridantriebssysteme typischen Belastungen, 2007.
- [147] B. Stiaszny, J.C. Ziegler, E.E. Krauß, M. Zhang, J.P. Schmidt, E. Ivers-Tiffée, Electrochemical characterization and post-mortem analysis of aged LiMn2O4–NMC/graphite lithium ion batteries part II: Calendar aging, *Journal of Power Sources* 258 (2014) 61–75. <https://doi.org/10.1016/j.jpowsour.2014.02.019>.
- [148] P. Shafiei Sabet, D.U. Sauer, Separation of predominant processes in electrochemical impedance spectra of lithium-ion batteries with nickel-manganese-cobalt cathodes, *Journal of Power Sources* 425 (2019) 121–129. <https://doi.org/10.1016/j.jpowsour.2019.03.068>.
- [149] B. Stiaszny, J.C. Ziegler, E.E. Krauß, J.P. Schmidt, E. Ivers-Tiffée, Electrochemical characterization and post-mortem analysis of aged LiMn2O4–Li(Ni0.5Mn0.3Co0.2)O2/graphite lithium ion batteries. Part I: Cycle aging, *Journal of Power Sources* 251 (2014) 439–450. <https://doi.org/10.1016/j.jpowsour.2013.11.080>.
- [150] E. Teliz, C.F. Zinola, V. Díaz, Identification and quantification of ageing mechanisms in Li-ion batteries by Electrochemical impedance spectroscopy, *Electrochimica Acta* 426 (2022) 140801. <https://doi.org/10.1016/j.electacta.2022.140801>.
- [151] D. Wasylowski, N. Kisseler, H. Ditler, M. Sonnet, G. Fuchs, F. Ringbeck, D.U. Sauer, Spatially resolving lithium-ion battery aging by open-hardware scanning acoustic imaging, *Journal of Power Sources* 521 (2022) 230825. <https://doi.org/10.1016/j.jpowsour.2021.230825>.
- [152] S. Gantenbein, M. Schönleber, M. Weiss, E. Ivers-Tiffée, Capacity Fade in Lithium-Ion Batteries and Cyclic Aging over Various State-of-Charge Ranges, *Sustainability* 11 (2019) 6697. <https://doi.org/10.3390/su11236697>.
- [153] J. Jiang, Y. Gao, C. Zhang, W. Zhang, Y. Jiang, Lifetime Rapid Evaluation Method for Lithium-Ion Battery with Li(NiMnCo)O₂ Cathode, *J. Electrochem. Soc.* 166 (2019) 1070–1081. <https://doi.org/10.1149/2.1051904jes>.
- [154] S. Watanabe, M. Kinoshita, T. Hosokawa, K. Morigaki, K. Nakura, Capacity fading of LiAl_yNi_{1–x–y}CoxO₂ cathode for lithium-ion batteries during accelerated calendar and cycle life tests (effect of depth of discharge in charge–discharge cycling on the suppression of

- the micro-crack generation of $\text{LiAl}_y\text{Ni}_{1-x-y}\text{Co}_x\text{O}_2$ particle), *Journal of Power Sources* 260 (2014) 50–56.
<https://doi.org/10.1016/j.jpowsour.2014.02.103>.
- [155] E. Wikner, E. Björklund, J. Fridner, D. Brandell, T. Thiringer, How the utilised SOC window in commercial Li-ion pouch cells influence battery ageing, *Journal of Power Sources Advances* 8 (2021) 100054.
<https://doi.org/10.1016/j.powera.2021.100054>.
- [156] W. Diao, S. Saxena, M. Pecht, Accelerated cycle life testing and capacity degradation modeling of LiCoO_2 -graphite cells, *Journal of Power Sources* 435 (2019) 226830.
<https://doi.org/10.1016/j.jpowsour.2019.226830>.
- [157] K. Takei, K. Kumai, Y. Kobayashi, H. Miyashiro, N. Terada, T. Iwahori, T. Tanaka, Cycle life estimation of lithium secondary battery by extrapolation method and accelerated aging test, *Journal of Power Sources* 97–98 (2001) 697–701. [https://doi.org/10.1016/S0378-7753\(01\)00646-2](https://doi.org/10.1016/S0378-7753(01)00646-2).
- [158] S. Barcellona, L. Piegari, Effect of current on cycle aging of lithium ion batteries, *Journal of Energy Storage* 29 (2020) 101310.
<https://doi.org/10.1016/j.est.2020.101310>.
- [159] L. Su, J. Zhang, C. Wang, Y. Zhang, Z. Li, Y. Song, T. Jin, Z. Ma, Identifying main factors of capacity fading in lithium ion cells using orthogonal design of experiments, *Applied Energy* 163 (2016) 201–210. <https://doi.org/10.1016/j.apenergy.2015.11.014>.
- [160] T. Gewald, A. Candussio, L. Wildfeuer, D. Lehmkuhl, A. Hahn, M. Lienkamp, Accelerated Aging Characterization of Lithium-ion Cells: Using Sensitivity Analysis to Identify the Stress Factors Relevant to Cyclic Aging, *Batteries* 6 (2020) 6.
<https://doi.org/10.3390/batteries6010006>.
- [161] M. Ecker, P. Shafiei Sabet, D.U. Sauer, Influence of operational condition on lithium plating for commercial lithium-ion batteries – Electrochemical experiments and post-mortem-analysis, *Applied Energy* 206 (2017) 934–946.
<https://doi.org/10.1016/j.apenergy.2017.08.034>.
- [162] D. Juarez-Robles, A.A. Vyas, C. Fear, J.A. Jeevarajan, P.P. Mukherjee, Overcharge and Aging Analytics of Li-Ion Cells, *J. Electrochem. Soc.* 167 (2020) 090547. <https://doi.org/10.1149/1945-7111/ab9569>.
- [163] S. Krueger, R. Kloepsch, J. Li, S. Nowak, S. Passerini, M. Winter, How Do Reactions at the Anode/Electrolyte Interface Determine the

- Cathode Performance in Lithium-Ion Batteries?, *J. Electrochem. Soc.* 160 (2013) A542–A548. <https://doi.org/10.1149/2.022304jes>.
- [164] P. Meister, H. Jia, J. Li, R. Kloepsch, M. Winter, T. Placke, Best Practice: Performance and Cost Evaluation of Lithium Ion Battery Active Materials with Special Emphasis on Energy Efficiency, *Chem. Mater.* 28 (2016) 7203–7217. <https://doi.org/10.1021/acs.chemmater.6b02895>.
- [165] A. Devie, M. Dubarry, Durability and Reliability of Electric Vehicle Batteries under Electric Utility Grid Operations. Part 1: Cell-to-Cell Variations and Preliminary Testing, *Batteries* 2 (2016) 28. <https://doi.org/10.3390/batteries2030028>.
- [166] J. Kasnatscheew, T. Placke, B. Streipert, S. Rothermel, R. Wagner, P. Meister, I.C. Laskovic, M. Winter, A Tutorial into Practical Capacity and Mass Balancing of Lithium Ion Batteries, *J. Electrochem. Soc.* 164 (2017) A2479–A2486. <https://doi.org/10.1149/2.0961712jes>.
- [167] W.M. Dose, C. Xu, C.P. Grey, M.F.L. Volder, Effect of Anode Slippage on Cathode Cutoff Potential and Degradation Mechanisms in Ni-Rich Li-Ion Batteries, *Cell Reports Physical Science* 1 (2020) 100253. <https://doi.org/10.1016/j.xcrp.2020.100253>.
- [168] M. Tang, P. Albertus, J. Newman, Two-Dimensional Modeling of Lithium Deposition during Cell Charging, *J. Electrochem. Soc.* 156 (2009) 390. <https://doi.org/10.1149/1.3095513>.
- [169] F. Grismann, T. Gerbert, F. Brauchle, A. Gruhle, J. Parisi, M. Knipper, Hysteresis and current dependence of the graphite anode color in a lithium-ion cell and analysis of lithium plating at the cell edge, *Journal of Energy Storage* 15 (2018) 17–22. <https://doi.org/10.1016/j.est.2017.10.015>.
- [170] S. Kim, D. Lee, Y. Han, H.W. Kim, D.-J. Yoo, Abnormal lithium plating in the electrode edges at low N/P ratios in lithium-ion batteries, *Journal of Power Sources* 601 (2024) 234301. <https://doi.org/10.1016/j.jpowsour.2024.234301>.
- [171] B. Gyenes, D.A. Stevens, V.L. Chevrier, J.R. Dahn, Understanding Anomalous Behavior in Coulombic Efficiency Measurements on Li-Ion Batteries, *J. Electrochem. Soc.* 162 (2015) A278–A283. <https://doi.org/10.1149/2.0191503jes>.
- [172] M. Lewerenz, J. Münnix, J. Schmalstieg, S. Käbitz, M. Knips, D.U. Sauer, Systematic aging of commercial LiFePO₄ | Graphite cylindrical cells including a theory explaining rise of capacity during aging,

- Journal of Power Sources 345 (2017) 254–263.
<https://doi.org/10.1016/j.jpowsour.2017.01.133>.
- [173] M. Lewerenz, G. Fuchs, L. Becker, D.U. Sauer, Irreversible calendar aging and quantification of the reversible capacity loss caused by anode overhang, *Journal of Energy Storage* 18 (2018) 149–159.
<https://doi.org/10.1016/j.est.2018.04.029>.
- [174] R. Burrell, A. Zulke, P. Keil, H. Hoster, Communication—Identifying and Managing Reversible Capacity Losses that Falsify Cycle Ageing Tests of Lithium-Ion Cells, *J. Electrochem. Soc.* 167 (2020) 130544.
<https://doi.org/10.1149/1945-7111/abbce1>.
- [175] F. Hildenbrand, D. Ditscheid, E. Barbers, D.U. Sauer, Influence of the anode overhang on the open-circuit voltage and the ageing of lithium-ion batteries—A model based study, *Applied Energy* 332 (2023) 120395. <https://doi.org/10.1016/j.apenergy.2022.120395>.
- [176] V. Zinth, C. Von Lüders, J. Wilhelm, S.V. Erhard, M. Hofmann, S. Seidlmayer, J. Rebelo-Kornmeier, W. Gan, A. Jossen, R. Gilles, Inhomogeneity and relaxation phenomena in the graphite anode of a lithium-ion battery probed by in situ neutron diffraction, *Journal of Power Sources* 361 (2017) 54–60.
<https://doi.org/10.1016/j.jpowsour.2017.06.060>.
- [177] L. Willenberg, P. Dechent, G. Fuchs, M. Teuber, M. Eckert, M. Graff, N. Kürten, D.U. Sauer, E. Figgemeier, The Development of Jelly Roll Deformation in 18650 Lithium-Ion Batteries at Low State of Charge, *J. Electrochem. Soc.* 167 (2020) 120502.
<https://doi.org/10.1149/1945-7111/aba96d>.
- [178] F.B. Spingler, S. Friedrich, S. Kücher, S. Schmid, D. López-Cruz, A. Jossen, The Effects of Non-Uniform Mechanical Compression of Lithium-Ion Cells on Local Current Densities and Lithium Plating, *J. Electrochem. Soc.* 168 (2021) 110515. <https://doi.org/10.1149/1945-7111/ac33e1>.
- [179] T.C. Bach, S.F. Schuster, E. Fleder, J. Müller, M.J. Brand, H. Lorrmann, A. Jossen, G. Sextl, Nonlinear aging of cylindrical lithium-ion cells linked to heterogeneous compression, *Journal of Energy Storage* 5 (2016) 212–223. <https://doi.org/10.1016/j.est.2016.01.003>.
- [180] P. Morales Torricos, C. Endisch, M. Lewerenz, Apparent Aging during Accelerated Cycling Aging Test of Cylindrical Silicon Containing Li-Ion Cells, *Batteries* 9 (2023) 230.
<https://doi.org/10.3390/batteries9040230>.

-
- [181] M. Lewerenz, D.U. Sauer, Evaluation of cyclic aging tests of prismatic automotive LiNiMnCoO₂-Graphite cells considering influence of homogeneity and anode overhang, *Journal of Energy Storage* 18 (2018) 421–434. <https://doi.org/10.1016/j.est.2018.06.003>.
- [182] Y. Kobayashi, H. Miyashiro, Y. Mita, Capacity fading of a LiFePO₄/graphite cell during shallow cycling due to planar inhomogeneity in LiFePO₄, *Journal of Power Sources* 451 (2020) 227782. <https://doi.org/10.1016/j.jpowsour.2020.227782>.
- [183] M. Lewerenz, A. Marongiu, A. Warnecke, D.U. Sauer, Differential voltage analysis as a tool for analyzing inhomogeneous aging: A case study for LiFePO₄|Graphite cylindrical cells, *Journal of Power Sources* 368 (2017) 57–67. <https://doi.org/10.1016/j.jpowsour.2017.09.059>.
- [184] M. Lewerenz, A. Warnecke, D.U. Sauer, Introduction of capacity difference analysis (CDA) for analyzing lateral lithium-ion flow to determine the state of covering layer evolution, *Journal of Power Sources* 354 (2017) 157–166. <https://doi.org/10.1016/j.jpowsour.2017.04.043>.
- [185] A. Senyshyn, M.J. Mühlbauer, O. Dolotko, M. Hofmann, H. Ehrenberg, Homogeneity of lithium distribution in cylinder-type Li-ion batteries, *Sci Rep* 5 (2015) 18380. <https://doi.org/10.1038/srep18380>.
- [186] X. Gao, Y. Li, H. Wang, X. Liu, Y. Wu, S. Yang, Z. Zhao, M. Ouyang, Probing inhomogeneity of electrical-thermal distribution on electrode during fast charging for lithium-ion batteries, *Applied Energy* 336 (2023) 120868. <https://doi.org/10.1016/j.apenergy.2023.120868>.
- [187] Y. Xie, S. Wang, R. Li, D. Ren, M. Yi, C. Xu, X. Han, L. Lu, B. Friess, G. Offer, M. Ouyang, Inhomogeneous degradation induced by lithium plating in a large-format lithium-ion battery, *Journal of Power Sources* 542 (2022) 231753. <https://doi.org/10.1016/j.jpowsour.2022.231753>.
- [188] J. Sturm, A. Rheinfeld, I. Zilberman, F.B. Spingler, S. Kosch, F. Frie, A. Jossen, Modeling and simulation of inhomogeneities in a 18650 nickel-rich, silicon-graphite lithium-ion cell during fast charging, *Journal of Power Sources* 412 (2019) 204–223. <https://doi.org/10.1016/j.jpowsour.2018.11.043>.

- [189] M. Keyser, A. Pesaran, Q. Li, S. Santhanagopalan, K. Smith, E. Wood, S. Ahmed, I. Bloom, E. Dufek, M. Shirk, A. Meintz, C. Kreuzer, C. Michelbacher, A. Burnham, T. Stephens, J. Francfort, B. Carlson, J. Zhang, R. Vijayagopal, K. Hardy, F. Dias, M. Mohanpurkar, D. Scofield, A.N. Jansen, T. Tanim, A. Markel, Enabling fast charging – Battery thermal considerations, *Journal of Power Sources* 367 (2017) 228–236. <https://doi.org/10.1016/j.jpowsour.2017.07.009>.
- [190] Y. Xie, A. Hales, R. Li, X. Feng, Y. Patel, G. Offer, Thermal Management Optimization for Large-Format Lithium-Ion Battery Using Cell Cooling Coefficient, *J. Electrochem. Soc.* 169 (2022) 110511. <https://doi.org/10.1149/1945-7111/ac9d08>.
- [191] S. Klink, W. Schuhmann, F. La Mantia, Vertical distribution of overpotentials and irreversible charge losses in lithium ion battery electrodes, *ChemSusChem* 7 (2014) 2159–66. <https://doi.org/10.1002/cssc.201400056>.
- [192] D. Burow, K. Sergeeva, S. Calles, K. Schorb, A. Börger, C. Roth, P. Heitjans, Inhomogeneous degradation of graphite anodes in automotive lithium ion batteries under low-temperature pulse cycling conditions, *Journal of Power Sources* 307 (2016) 806–814. <https://doi.org/10.1016/j.jpowsour.2016.01.033>.
- [193] Lain, Brandon, Kendrick, Design Strategies for High Power vs. High Energy Lithium Ion Cells, *Batteries* 5 (2019) 64. <https://doi.org/10.3390/batteries5040064>.
- [194] N. Ogihara, S. Kawauchi, C. Okuda, Y. Itou, Y. Takeuchi, Y. Ukyo, Theoretical and Experimental Analysis of Porous Electrodes for Lithium-Ion Batteries by Electrochemical Impedance Spectroscopy Using a Symmetric Cell, *J. Electrochem. Soc.* 159 (2012) A1034–A1039. <https://doi.org/10.1149/2.057207jes>.
- [195] X. Zhang, Z. Ju, Y. Zhu, K.J. Takeuchi, E.S. Takeuchi, A.C. Marschilok, G. Yu, Multiscale Understanding and Architecture Design of High Energy/Power Lithium-Ion Battery Electrodes, *Advanced Energy Materials* 11 (2021) 2000808. <https://doi.org/10.1002/aenm.202000808>.
- [196] K.A. Akanni, J.W. Evans, I.S. Abramson, Effective transport coefficients in heterogeneous media, *Chemical Engineering Science* 42 (1987) 1945–1954. [https://doi.org/10.1016/0009-2509\(87\)80141-0](https://doi.org/10.1016/0009-2509(87)80141-0).

- [197] M. Dubarry, C. Truchot, B.Y. Liaw, Cell degradation in commercial LiFePO₄ cells with high-power and high-energy designs, *Journal of Power Sources* 258 (2014) 408–419. <https://doi.org/10.1016/j.jpowsour.2014.02.052>.
- [198] P. Kuntz, O. Raccurt, P. Azaïs, K. Richter, T. Waldmann, M. Wohlfahrt-Mehrens, M. Bardet, A. Buzlukov, S. Genies, Identification of Degradation Mechanisms by Post-Mortem Analysis for High Power and High Energy Commercial Li-Ion Cells after Electric Vehicle Aging, *Batteries* 7 (2021) 48. <https://doi.org/10.3390/batteries7030048>.
- [199] P.M. Attia, A. Bills, F. Brosa Planella, P. Dechent, G. dos Reis, M. Dubarry, P. Gasper, R. Gilchrist, S. Greenbank, D. Howey, O. Liu, E. Khoo, Y. Preger, A. Soni, S. Sripad, A.G. Stefanopoulou, V. Sulzer, Review—“Knees” in Lithium-Ion Battery Aging Trajectories, *J. Electrochem. Soc.* 169 (2022) 060517. <https://doi.org/10.1149/1945-7111/ac6d13>.
- [200] B.E. Deal, A.S. Grove, General Relationship for the Thermal Oxidation of Silicon, *J. Appl. Phys.* 36 (1965) 3770–3778. <https://doi.org/10.1063/1.1713945>.
- [201] R.B. Wright, C.G. Motloch, J.R. Belt, J.P. Christophersen, Calendar- and cycle-life studies of advanced technology development program generation 1 lithium-ion batteries, *Journal of Power Sources* (2002) 445–470.
- [202] M. Ecker, J.B. Gerschler, J. Vogel, S. Käbitz, F. Hust, P. Dechent, D.U. Sauer, Development of a lifetime prediction model for lithium-ion batteries based on extended accelerated aging test data, *Journal of Power Sources* 215 (2012) 248–257. <https://doi.org/10.1016/j.jpowsour.2012.05.012>.
- [203] J. Wang, J. Purewal, P. Liu, J. Hicks-Garner, S. Soukazian, E. Sherman, A. Sorenson, L. Vu, H. Tataria, M.W. Verbrugge, Degradation of lithium ion batteries employing graphite negatives and nickel–cobalt–manganese oxide + spinel manganese oxide positives: Part 1, aging mechanisms and life estimation, *Journal of Power Sources* 269 (2014) 937–948. <https://doi.org/10.1016/j.jpowsour.2014.07.030>.
- [204] P.M. Attia, W.C. Chueh, S.J. Harris, Revisiting the $t^{0.5}$ Dependence of SEI Growth, *J. Electrochem. Soc.* 167 (2020) 090535. <https://doi.org/10.1149/1945-7111/ab8ce4>.

- [205] I. Bloom, B.W. Cole, J.J. Sohn, S.A. Jones, E.G. Polzin, V.S. Battaglia, G.L. Henriksen, C. Motloch, R. Richardson, T. Unkelhaeuser, D. Ingersoll, H.L. Case, An accelerated calendar and cycle life study of Li-ion cells, *Journal of Power Sources* 101 (2001) 238–247. [https://doi.org/10.1016/S0378-7753\(01\)00783-2](https://doi.org/10.1016/S0378-7753(01)00783-2).
- [206] M. Ecker, N. Nieto, S. Käbitz, J. Schmalstieg, H. Blanke, A. Warnecke, D.U. Sauer, Calendar and cycle life study of Li(NiMnCo)O₂-based 18650 lithium-ion batteries, *Journal of Power Sources* 248 (2014) 839–851. <https://doi.org/10.1016/j.jpowsour.2013.09.143>.
- [207] L. Lam, P. Bauer, Practical Capacity Fading Model for Li-Ion Battery Cells in Electric Vehicles, *IEEE Trans. Power Electron.* 28 (2013) 5910–5918. <https://doi.org/10.1109/TPEL.2012.2235083>.
- [208] L. Von Kolzenberg, A. Latz, B. Horstmann, Chemo-Mechanical Model of SEI Growth on Silicon Electrode Particles**, *Batteries & Supercaps* 5 (2022) e202100216. <https://doi.org/10.1002/batt.202100216>.
- [209] S.F. Schuster, T. Bach, E. Fleder, J. Müller, M. Brand, G. Sextl, A. Jossen, Nonlinear aging characteristics of lithium-ion cells under different operational conditions, *Journal of Energy Storage* 1 (2015) 44–53. <https://doi.org/10.1016/j.est.2015.05.003>.
- [210] M. Dubarry, C. Truchot, B.Y. Liaw, K. Gering, S. Sazhin, D. Jamison, C. Michelbacher, Evaluation of commercial lithium-ion cells based on composite positive electrode for plug-in hybrid electric vehicle applications. Part II. Degradation mechanism under 2C cycle aging, *Journal of Power Sources* 196 (2011) 10336–10343. <https://doi.org/10.1016/j.jpowsour.2011.08.078>.
- [211] E. Redondo-Iglesias, P. Venet, S. Pelissier, Calendar and cycling ageing combination of batteries in electric vehicles, *Microelectronics Reliability* 88–90 (2018) 1212–1215. <https://doi.org/10.1016/j.microrel.2018.06.113>.
- [212] T. Raj, A.A. Wang, C.W. Monroe, D.A. Howey, Investigation of Path-Dependent Degradation in Lithium-Ion Batteries**, *Batteries & Supercaps* 3 (2020) 1377–1385. <https://doi.org/10.1002/batt.202000160>.
- [213] M. Rogge, A. Jossen, Path-Dependent Ageing of Lithium-ion Batteries and Implications on the Ageing Assessment of Accelerated Ageing Tests, *Batteries & Supercaps* 7 (2024) e202300313. <https://doi.org/10.1002/batt.202300313>.

- [214] A. Karger, L. Wildfeuer, D. Aygöl, A. Maheshwari, J.P. Singer, A. Jossen, Modeling capacity fade of lithium-ion batteries during dynamic cycling considering path dependence, *Journal of Energy Storage* 52 (2022) 104718.
<https://doi.org/10.1016/j.est.2022.104718>.
- [215] S. Arrhenius, Über die Reaktionsgeschwindigkeit bei der Inversion von Rohrzucker durch Säuren, *Z. Physik. Chem.* 4 (1889) 226–248.
- [216] M. Broussely, S. Herreyre, P. Biensan, P. Kasztejna, K. Nechev, R.J. Staniewicz, Aging mechanism in Li ion cells and calendar life predictions, *Journal of Power Sources* 97–98 (2001) 13–21.
[https://doi.org/10.1016/S0378-7753\(01\)00722-4](https://doi.org/10.1016/S0378-7753(01)00722-4).
- [217] B.Y. Liaw, E.P. Roth, R.G. Jungst, G. Nagasubramanian, H.L. Case, D.H. Doughty, Correlation of Arrhenius behaviors in power and capacity fades with cell impedance and heat generation in cylindrical lithium-ion cells, *Journal of Power Sources* (2003) 874–886.
- [218] A. Friesen, X. Mönnighoff, M. Börner, J. Haetge, F.M. Schappacher, M. Winter, Influence of temperature on the aging behavior of 18650-type lithium ion cells: A comprehensive approach combining electrochemical characterization and post-mortem analysis, *Journal of Power Sources* 342 (2017) 88–97.
<https://doi.org/10.1016/j.jpowsour.2016.12.040>.
- [219] A. Maheshwari, M. Heck, M. Santarelli, Cycle aging studies of lithium nickel manganese cobalt oxide-based batteries using electrochemical impedance spectroscopy, *Electrochimica Acta* 273 (2018) 335–348. <https://doi.org/10.1016/j.electacta.2018.04.045>.
- [220] D.A. Stevens, R.Y. Ying, R. Fathi, J.N. Reimers, J.E. Harlow, J.R. Dahn, Using High Precision Coulometry Measurements to Compare the Degradation Mechanisms of NMC/LMO and NMC-Only Automotive Scale Pouch Cells, *J. Electrochem. Soc.* 161 (2014) 1364–1370.
<https://doi.org/10.1149/2.0971409jes>.
- [221] V. Ruiz, A. Kriston, I. Adanouj, M. Destro, D. Fontana, A. Pfrang, Degradation Studies on Lithium Iron Phosphate - Graphite Cells. The Effect of Dissimilar Charging – Discharging Temperatures, *Electrochimica Acta* 240 (2017) 495–505.
<https://doi.org/10.1016/j.electacta.2017.03.126>.
- [222] X.-G. Yang, T. Liu, Y. Gao, S. Ge, Y. Leng, D. Wang, C.-Y. Wang, Asymmetric Temperature Modulation for Extreme Fast Charging of

- Lithium-Ion Batteries, *Joule* 3 (2019) 3002–3019.
<https://doi.org/10.1016/j.joule.2019.09.021>.
- [223] M. Feinauer, M. Wohlfahrt-Mehrens, M. Hölzle, T. Waldmann, Temperature-driven path dependence in Li-ion battery cyclic aging, *Journal of Power Sources* 594 (2024) 233948.
<https://doi.org/10.1016/j.jpowsour.2023.233948>.
- [224] S. Kosch, A. Rheinfeld, S.V. Erhard, A. Jossen, An extended polarization model to study the influence of current collector geometry of large-format lithium-ion pouch cells, *Journal of Power Sources* 342 (2017) 666–676.
<https://doi.org/10.1016/j.jpowsour.2016.12.110>.
- [225] M. Klett, R. Eriksson, J. Groot, P. Svens, K. Ciosek Högström, R.W. Lindström, H. Berg, T. Gustafson, G. Lindbergh, K. Edström, Non-uniform aging of cycled commercial LiFePO₄/graphite cylindrical cells revealed by post-mortem analysis, *Journal of Power Sources* 257 (2014) 126–137.
<https://doi.org/10.1016/j.jpowsour.2014.01.105>.
- [226] I.D. Campbell, M. Marzook, M. Marinescu, G.J. Offer, How Observable Is Lithium Plating? Differential Voltage Analysis to Identify and Quantify Lithium Plating Following Fast Charging of Cold Lithium-Ion Batteries, *J. Electrochem. Soc.* 166 (2019) 725–739.
<https://doi.org/10.1149/2.0821904jes>.
- [227] T. Sun, T. Shen, Y. Zheng, D. Ren, W. Zhu, J. Li, Y. Wang, K. Kuang, X. Rui, S. Wang, L. Wang, X. Han, L. Lu, M. Ouyang, Modeling the inhomogeneous lithium plating in lithium-ion batteries induced by non-uniform temperature distribution, *Electrochimica Acta* 425 (2022) 140701. <https://doi.org/10.1016/j.electacta.2022.140701>.
- [228] Y. Zhu, J. Xie, A. Pei, B. Liu, Y. Wu, D. Lin, J. Li, H. Wang, H. Chen, J. Xu, A. Yang, C.-L. Wu, H. Wang, W. Chen, Y. Cui, Fast lithium growth and short circuit induced by localized-temperature hotspots in lithium batteries, *Nat Commun* 10 (2019) 2067.
<https://doi.org/10.1038/s41467-019-09924-1>.
- [229] K. Xu, Y. Lam, S.S. Zhang, T.R. Jow, T.B. Curtis, Solvation Sheath of Li⁺ in Nonaqueous Electrolytes and Its Implication of Graphite/Electrolyte Interface Chemistry, *J. Phys. Chem. C* 111 (2007) 7411–7421. <https://doi.org/10.1021/jp068691u>.
- [230] O. Dondelewski, T. Szemberg O'Connor, Y. Zhao, I.A. Hunt, A. Holland, A. Hales, G.J. Offer, Y. Patel, The role of cell geometry when

- selecting tab or surface cooling to minimise cell degradation, *eTransportation* 5 (2020) 100073.
<https://doi.org/10.1016/j.etrans.2020.100073>.
- [231] M. Fleckenstein, O. Bohlen, M.A. Roscher, B. Bäker, Current density and state of charge inhomogeneities in Li-ion battery cells with LiFePO₄ as cathode material due to temperature gradients, *Journal of Power Sources* 196 (2011) 4769–4778.
<https://doi.org/10.1016/j.jpowsour.2011.01.043>.
- [232] M. Al-Amin, A. Barai, T.R. Ashwin, J. Marco, An Insight to the Degradation Behaviour of the Parallel Connected Lithium-Ion Battery Cells, *Energies* 14 (2021) 4716.
<https://doi.org/10.3390/en14164716>.
- [233] W. Shi, X. Hu, C. Jin, J. Jiang, Y. Zhang, T. Yip, Effects of imbalanced currents on large-format LiFePO₄ /graphite batteries systems connected in parallel, *Journal of Power Sources* 313 (2016) 198–204.
<https://doi.org/10.1016/j.jpowsour.2016.02.087>.
- [234] H.-H. Huang, H.-Y. Chen, K.-C. Liao, H.-T. Young, C.-F. Lee, J.-Y. Tien, Thermal-electrochemical coupled simulations for cell-to-cell imbalances in lithium-iron-phosphate based battery packs, *Applied Thermal Engineering* 123 (2017) 584–591.
<https://doi.org/10.1016/j.applthermaleng.2017.05.105>.
- [235] S. Paul, C. Diegelmann, H. Kabza, W. Tillmetz, Analysis of ageing inhomogeneities in lithium-ion battery systems, *Journal of Power Sources* 239 (2013) 642–650.
<https://doi.org/10.1016/j.jpowsour.2013.01.068>.
- [236] G.M. Cavaleiro, T. Iriyama, G.J. Nelson, S. Huang, G. Zhang, Effects of Nonuniform Temperature Distribution on Degradation of Lithium-Ion Batteries, *Journal of Electrochemical Energy Conversion and Storage* 17 (2020) 378. <https://doi.org/10.1115/1.4045205>.
- [237] N. Yang, X. Zhang, B. Shang, G. Li, Unbalanced discharging and aging due to temperature differences among the cells in a lithium-ion battery pack with parallel combination, *Journal of Power Sources* 306 (2016) 733–741.
<https://doi.org/10.1016/j.jpowsour.2015.12.079>.
- [238] Q.Q. Liu, D.J. Xiong, R. Petibon, C.Y. Du, J.R. Dahn, Gas Evolution during Unwanted Lithium Plating in Li-Ion Cells with EC-Based or EC-Free Electrolytes, *J. Electrochem. Soc.* 163 (2016) 3010–3015.
<https://doi.org/10.1149/2.0711614jes>.

- [239] S. Paarmann, How Non-Uniform Temperatures Influence the Performance and Ageing of Lithium-Ion Batteries, (2021). <https://doi.org/10.5445/IR/1000139983>.
- [240] P. Michalowski, A. Gräfenstein, M. Knipper, T. Plaggenborg, J. Schwenzel, J. Parisi, Examining Inhomogeneous Degradation of Graphite/Carbon Black Composite Electrodes in Li-Ion Batteries by Lock-In Thermography, *J. Electrochem. Soc.* 164 (2017) A2251–A2255. <https://doi.org/10.1149/2.0281712jes>.
- [241] D. Werner, S. Paarmann, T. Wetzel, Calendar Aging of Li-Ion Cells—Experimental Investigation and Empirical Correlation, *Batteries* 7 (2021) 28. <https://doi.org/10.3390/batteries7020028>.
- [242] R. Schmich, R. Wagner, G. Hörpel, T. Placke, M. Winter, Performance and cost of materials for lithium-based rechargeable automotive batteries, *Nat Energy* 3 (2018) 267–278. <https://doi.org/10.1038/s41560-018-0107-2>.
- [243] L. Cloos, S. Herberger, P. Seegert, T. Wetzel, Thermal Material Properties of Commercial NMC111-LMO / Graphite Lithium-Ion Battery Cell, (2024) 10,4 kB. <https://doi.org/10.35097/KALRZQZUAHBXWKIJ>.
- [244] L. Cloos, S. Herberger, O. Queisser, P. Seegert, T. Wetzel, Thermal Material Properties of Commercial NMC532 / Graphite Lithium-Ion Battery Cell, (2024) 8,2 kB. <https://doi.org/10.35097/PBJZPQLKKWZAOJKN>.
- [245] J. Cannarella, C.B. Arnold, Stress evolution and capacity fade in constrained lithium-ion pouch cells, *Journal of Power Sources* 245 (2014) 745–751. <https://doi.org/10.1016/j.jpowsour.2013.06.165>.
- [246] V. Müller, R.-G. Scurtu, K. Richter, T. Waldmann, M. Memm, M.A. Danzer, M. Wohlfahrt-Mehrens, Effects of Mechanical Compression on the Aging and the Expansion Behavior of Si/C-Composite|NMC811 in Different Lithium-Ion Battery Cell Formats, *J. Electrochem. Soc.* 166 (2019) 3796–3805. <https://doi.org/10.1149/2.1121915jes>.
- [247] J.P. Christophersen, C.D. Ho, C.G. Motloch, D. Howell, H.L. Hess, Effects of Reference Performance Testing during Aging Using Commercial Lithium-Ion Cells, *J. Electrochem. Soc.* 153 (2006) A1406. <https://doi.org/10.1149/1.2201473>.

-
- [248] S. Barcellona, S. Colnago, L. Piegari, Aging Effect on Lithium-Ion Battery Resistance Hysteresis, *IEEE Trans. on Ind. Applicat.* 59 (2023) 4516–4527. <https://doi.org/10.1109/TIA.2023.3266307>.
- [249] W.D. Widanage, O. Queisser, S. Paarmann, L. Cloos, T. Wetzel, A System Identification Approach to Estimate Lithium-Ion Battery Entropy Coefficients, *J. Electrochem. Soc.* 172 (2025) 090514. <https://doi.org/10.1149/1945-7111/adfe1f>.
- [250] A. Eddahech, O. Briat, J.-M. Vinassa, Thermal characterization of a high-power lithium-ion battery: Potentiometric and calorimetric measurement of entropy changes, *Energy* 61 (2013) 432–439. <https://doi.org/10.1016/j.energy.2013.09.028>.
- [251] S.A. Hallaj, J. Prakash, J.R. Selman, Characterization of commercial Li-ion batteries using electrochemical–calorimetric measurements, (2000).
- [252] X.-F. Zhang, Y. Zhao, Y. Patel, T. Zhang, W.-M. Liu, M. Chen, G.J. Offer, Y. Yan, Potentiometric measurement of entropy change for lithium batteries, *Phys Chem Chem Phys* 19 (2017) 9833–9842. <https://doi.org/10.1039/c6cp08505a>.
- [253] J.-S. Hong, H. Maleki, S. Al Hallaj, L. Redey, J.R. Selman, Electrochemical-Calorimetric Studies of Lithium-Ion Cells, *J. Electrochem. Soc.* 145 (1998) 1489–1501.
- [254] J.M. Sherfey, A. Brenner, Electrochemical Calorimetry, *J. Electrochem. Soc.* 105 (1958) 665. <https://doi.org/10.1149/1.2428687>.
- [255] J. Zhang, J. Huang, Z. Li, B. Wu, Z. Nie, Y. Sun, F. An, N. Wu, Comparison and validation of methods for estimating heat generation rate of large-format lithium-ion batteries, *J Therm Anal Calorim* 117 (2014) 447–461. <https://doi.org/10.1007/s10973-014-3672-z>.
- [256] H. Jouhara, N. Serey, N. Khordehghah, R. Bennett, S. Almahmoud, S.P. Lester, Investigation, development and experimental analyses of a heat pipe based battery thermal management system, *International Journal of Thermofluids* 1–2 (2020) 100004. <https://doi.org/10.1016/j.ijft.2019.100004>.
- [257] M.A. Samieian, A. Hales, Y. Patel, A Novel Experimental Technique for Use in Fast Parameterisation of Equivalent Circuit Models for Lithium-Ion Batteries, *Batteries* 8 (2022) 125. <https://doi.org/10.3390/batteries8090125>.

- [258] P. Dechent, S. Greenbank, F. Hildenbrand, S. Jbabdi, D.U. Sauer, D.A. Howey, Estimation of Li-ion degradation test sample sizes required to understand cell-to-cell variability, *Batteries & Supercaps* 4 (2021) 1821–1829. <https://doi.org/10.1002/batt.202100148>.
- [259] Y. Zhao, L.B. Diaz, Y. Patel, T. Zhang, G.J. Offer, How to Cool Lithium Ion Batteries: Optimising Cell Design using a Thermally Coupled Model, *J. Electrochem. Soc.* 166 (2019) A2849–A2859. <https://doi.org/10.1149/2.0501913jes>.
- [260] O. Queisser, L. Cloos, F. Boehm, D. Oehler, T. Wetzel, Impact of the Level of Homogenization in 3D Thermal Simulation on the Internal Temperature Distribution of Li-Ion Battery Cells, *Energy Tech* 9 (2021) 2000915. <https://doi.org/10.1002/ente.202000915>.
- [261] D. Andre, M. Meiler, K. Steiner, H. Walz, T. Soczka-Guth, D.U. Sauer, Characterization of high-power lithium-ion batteries by electrochemical impedance spectroscopy. II: Modelling, *Journal of Power Sources* 196 (2011) 5349–5356. <https://doi.org/10.1016/j.jpowsour.2010.07.071>.
- [262] V.W. Hu, D.T. Schwartz, Low Error Estimation of Half-Cell Thermodynamic Parameters from Whole-Cell Li-Ion Battery Experiments: Physics-Based Model Formulation, Experimental Demonstration, and an Open Software Tool, *J. Electrochem. Soc.* 169 (2022) 030539. <https://doi.org/10.1149/1945-7111/ac5a1a>.
- [263] D.W. Bacon, D.G. Watts, Estimating the transition between two intersecting straight lines, *Biometrika* 58 (1971) 525–534. <https://doi.org/10.1093/biomet/58.3.525>.
- [264] P. Fermín-Cueto, E. McTurk, M. Allerhand, E. Medina-Lopez, M.F. Anjos, J. Sylvester, G. Dos Reis, Identification and machine learning prediction of knee-point and knee-onset in capacity degradation curves of lithium-ion cells, *Energy and AI* 1 (2020) 100006. <https://doi.org/10.1016/j.egyai.2020.100006>.
- [265] W. Guo, Z. Sun, S.B. Vilsen, J. Meng, D.I. Stroe, Review of “grey box” lifetime modeling for lithium-ion battery: Combining physics and data-driven methods, *Journal of Energy Storage* 56 (2022) 105992. <https://doi.org/10.1016/j.est.2022.105992>.
- [266] S. Li, A.N. Patel, C. Zhang, T. Amietszajew, N. Kirkaldy, G.J. Offer, M. Marinescu, Internal temperature estimation for lithium-ion batteries through distributed equivalent circuit network model, *Journal of*

- Power Sources 611 (2024) 234701.
<https://doi.org/10.1016/j.jpowsour.2024.234701>.
- [267] M.S. Hosen, J. Jaguemont, J. van Mierlo, M. Bercebar, Battery lifetime prediction and performance assessment of different modeling approaches, *iScience* 24 (2021) 102060.
<https://doi.org/10.1016/j.isci.2021.102060>.
- [268] U.S. Kim, C.B. Shin, C.-S. Kim, Effect of electrode configuration on the thermal behavior of a lithium-polymer battery, *Journal of Power Sources* 180 (2008) 909–916.
<https://doi.org/10.1016/j.jpowsour.2007.09.054>.
- [269] J. Newman, W. Tiedemann, Temperature Rise in a Battery Module with Constant Heat Generation, *J. Electrochem. Soc.* 142 (1995) 1054–1057. <https://doi.org/10.1149/1.2044130>.
- [270] H. Gu, Mathematical Analysis of a Zn / NiOOH Cell, *J. Electrochem. Soc.* 130 (1983) 1459–1464. <https://doi.org/10.1149/1.2120009>.
- [271] U.S. Kim, C.B. Shin, C.-S. Kim, Modeling for the scale-up of a lithium-ion polymer battery, *Journal of Power Sources* 189 (2009) 841–846.
<https://doi.org/10.1016/j.jpowsour.2008.10.019>.
- [272] H. Pegel, D. Wycisk, A. Scheible, L. Tendera, A. Latz, D.U. Sauer, Fast-charging performance and optimal thermal management of large-format full-tab cylindrical lithium-ion cells under varying environmental conditions, *Journal of Power Sources* 556 (2023) 232408. <https://doi.org/10.1016/j.jpowsour.2022.232408>.
- [273] M. Marinescu, N. Marinescu, *Elektrotechnik für Studium und Praxis: Gleich-, Wechsel- und Drehstrom, Schalt- und nichtsinusförmige Vorgänge*, Springer Fachmedien Wiesbaden, Wiesbaden, 2020.
<https://doi.org/10.1007/978-3-658-28884-6>.
- [274] X. Hu, S. Li, P. Huei, A comparative study of equivalent circuit models for Li-ion batteries, *Journal of Power Sources* 198 (2012) 359–367.
- [275] V. Pop, H.J. Bergveld, J.H.G. Op Het Veld, P.P.L. Regtien, D. Danilov, P.H.L. Notten, Modeling Battery Behavior for Accurate State-of-Charge Indication, *J. Electrochem. Soc.* 153 (2006) A2013.
<https://doi.org/10.1149/1.2335951>.
- [276] R. Drees, F. Lienesch, M. Kurrat, Fast charging lithium-ion battery formation based on simulations with an electrode equivalent circuit model, *Journal of Energy Storage* 36 (2021) 102345.
<https://doi.org/10.1016/j.est.2021.102345>.

- [277] C. Zhang, T. Amietszajew, S. Li, M. Marinescu, G. Offer, C. Wang, Y. Guo, R. Bhagat, Real-time estimation of negative electrode potential and state of charge of lithium-ion battery based on a half-cell-level equivalent circuit model, *Journal of Energy Storage* 51 (2022) 104362. <https://doi.org/10.1016/j.est.2022.104362>.
- [278] Y. Merla, B. Wu, V. Yufit, R.F. Martinez-Botas, G.J. Offer, An easy-to-parameterise physics-informed battery model and its application towards lithium-ion battery cell design, diagnosis, and degradation, *Journal of Power Sources* 384 (2018) 66–79. <https://doi.org/10.1016/j.jpowsour.2018.02.065>.
- [279] D. Andre, M. Meiler, K. Steiner, Ch. Wimmer, T. Soczka-Guth, D.U. Sauer, Characterization of high-power lithium-ion batteries by electrochemical impedance spectroscopy. I. Experimental investigation, *Journal of Power Sources* 196 (2011) 5334–5341. <https://doi.org/10.1016/j.jpowsour.2010.12.102>.
- [280] M. Dubarry, B.Y. Liaw, Development of a universal modeling tool for rechargeable lithium batteries, *Journal of Power Sources* 174 (2007) 856–860. <https://doi.org/10.1016/j.jpowsour.2007.06.157>.
- [281] P. Böckh, T. Wetzel, *Wärmeübertragung: Grundlagen und Praxis*, Springer Berlin Heidelberg, Berlin, Heidelberg, 2015. <https://doi.org/10.1007/978-3-662-44477-1>.
- [282] Chen, Y. and Evans, J., *Heat Transfer Phenomena in Lithium/Polymer-Electrolyte Batteries for Electric Vehicle Application*, J. Electrochem. Soc. (1993).
- [283] D. Bernardi, E. Pawlikowski, J. Newman, A General Energy Balance for Battery Systems, *J. Electrochem. Soc.* 132 (1985) 5–12.
- [284] W.B. Gu, C.Y. Wang, Thermal-Electrochemical Modeling of Battery Systems, *J. Electrochem. Soc.* (2000) 2910–2922.
- [285] A. Farmann, D.U. Sauer, A study on the dependency of the open-circuit voltage on temperature and actual aging state of lithium-ion batteries, *Journal of Power Sources* 347 (2017) 1–13. <https://doi.org/10.1016/j.jpowsour.2017.01.098>.
- [286] D. Oehler, Bestimmung der thermischen Transporteigenschaften poröser Elektroden von Lithium-Ionen Batterien, 2021. <https://doi.org/10.5445/KSP/1000136047>.
- [287] A. Loges, S. Herberger, D. Werner, T. Wetzel, Thermal characterization of Li-ion cell electrodes by photothermal deflection

- spectroscopy, *Journal of Power Sources* 325 (2016) 104–115.
<https://doi.org/10.1016/j.jpowsour.2016.05.082>.
- [288] C. Pastor-Fernandez, W. Dhammika Widanage, J. Marco, M.-A. Gama-Valdez, Gael.H. Chouchelamane, Identification and quantification of ageing mechanisms in Lithium-ion batteries using the EIS technique, in: 2016 IEEE Transportation Electrification Conference and Expo (ITEC), IEEE, 2016: pp. 1–6.
<https://doi.org/10.1109/ITEC.2016.7520198>.
- [289] W. Shi, X. Hu, J. Wang, J. Jiang, Y. Zhang, T. Yip, Analysis of Thermal Aging Paths for Large-Format LiFePO₄/Graphite Battery, *Electrochimica Acta* 196 (2016) 13–23.
<https://doi.org/10.1016/j.electacta.2016.02.161>.
- [290] F. Yun, W. Jin, L. Tang, W. Li, J. Pang, S. Lu, Analysis of Capacity Fade from Entropic Heat Coefficient of Li[Ni_xCo_yMn_z]O₂/Graphite Lithium Ion Battery, *J. Electrochem. Soc.* 163 (2016) 639–643.
<https://doi.org/10.1149/2.0311605jes>.
- [291] Y. Hu, S.-Y. Choe, T.R. Garrick, Hybridized time-frequency method for the measurement of entropy coefficient of lithium-ion battery, *Electrochimica Acta* 362 (2020) 137124.
<https://doi.org/10.1016/j.electacta.2020.137124>.
- [292] T.M. Stanciu, D.-I. Stroe, M. Swierczynski, R. Teodorescu, N. Nieto, J. Gastelurrutia, J.-M. Timmermans, Performance degradation of thermal parameters during cycle ageing of high energy density Ni-Mn-Co based Lithium-Ion battery cells, in: 2016 IEEE Energy Conversion Congress and Exposition (ECCE), IEEE, 2016: pp. 1–7.
<https://doi.org/10.1109/ECCE.2016.7855341>.
- [293] Georgi Kovachev, Andrea Astner, Gregor Gstrein, Luigi Aiello, Johann Hemmer, Wolfgang Sinz and Christian Ellersdorfer, Thermal Conductivity in Aged Li-Ion Cells under Various Compression Conditions and State-of-Charge, (n.d.).
- [294] L. Tendra, D. Wycisk, C. Gonzalez, J. Stadler, K.P. Birke, Influence of state of health and individual aging mechanisms on the thermal conductivity of lithium-ion cells, *Journal of Energy Storage* 62 (2023) 106940. <https://doi.org/10.1016/j.est.2023.106940>.
- [295] A. Marconnet, S. Herberger, S. Paarmann, P. Seegert, T. Wetzel, Impact of aging on the thermophysical properties of lithium-ion battery electrodes, *Journal of Power Sources* 603 (2024) 234367.
<https://doi.org/10.1016/j.jpowsour.2024.234367>.

- [296] J. Schmalstieg, S. Käbitz, M. Ecker, D.U. Sauer, A holistic aging model for Li(NiMnCo)O₂ based 18650 lithium-ion batteries, *Journal of Power Sources* 257 (2014) 325–334. <https://doi.org/10.1016/j.jpowsour.2014.02.012>.
- [297] A.J. Smith, P. Svens, M. Varini, G. Lindbergh, R.W. Lindström, Expanded In Situ Aging Indicators for Lithium-Ion Batteries with a Blended NMC-LMO Electrode Cycled at Sub-Ambient Temperature, *J. Electrochem. Soc.* 168 (2021) 110530. <https://doi.org/10.1149/1945-7111/ac2d17>.
- [298] L. Cloos, J. Langer, M. Schiffler, A. Weber, Th. Wetzel, Erratum: Challenges of Predicting Temperature Dependent Capacity Loss Using the Example of NMC-LMO Lithium-Ion Battery Cells [J. Electrochem. Soc., 171, 040538 (2024)], *J. Electrochem. Soc.* 171 (2024) 129001. <https://doi.org/10.1149/1945-7111/ad9218>.
- [299] C.-J. Ko, C.-H. Chen, K.-C. Chen, Influence of inhomogeneity of lithium-ion transport within the anode/electrolyte interface on mossy lithium formation, *Journal of Power Sources* 563 (2023) 232779. <https://doi.org/10.1016/j.jpowsour.2023.232779>.
- [300] F.M. Kindermann, J. Keil, A. Frank, A. Jossen, A SEI Modeling Approach Distinguishing between Capacity and Power Fade, *J. Electrochem. Soc.* 164 (2017) 287–294. <https://doi.org/10.1149/2.0321712jes>.
- [301] M. Zhuo, G. Offer, M. Marinescu, Degradation model of high-nickel positive electrodes: Effects of loss of active material and cyclable lithium on capacity fade, *Journal of Power Sources* 556 (2023) 232461. <https://doi.org/10.1016/j.jpowsour.2022.232461>.
- [302] V.R. Subramanian, V. Boovaragavan, V. Ramadesigan, M. Arabandi, Mathematical Model Reformulation for Lithium-Ion Battery Simulations: Galvanostatic Boundary Conditions, *J. Electrochem. Soc.* 156 (2009) A260. <https://doi.org/10.1149/1.3065083>.
- [303] S.E.J. O’Kane, W. Ai, G. Madabattula, D. Alonso-Alvarez, R. Timms, V. Sulzer, J.S. Edge, B. Wu, G.J. Offer, M. Marinescu, Lithium-ion battery degradation: how to model it, *Phys Chem Chem Phys* 24 (2022) 7909–7922. <https://doi.org/10.1039/d2cp00417h>.
- [304] BIPM, IEC, IFCC, ILAC, ISO, IUPAC, IUPAP, and OIML, Evaluation of measurement data — Guide to the expression of uncertainty in measurement. Joint Committee for Guides in Metrology, JCGM 100:2008, (-).

- https://www.bipm.org/documents/20126/2071204/JCGM_100_2008_E.pdf/cb0ef43f-baa5-11cf-3f85-4dcd86f77bd6.
- [305] K. Jalkanen, J. Karppinen, L. Skogström, T. Laurila, M. Nisula, K. Vuorilehto, Cycle aging of commercial NMC/graphite pouch cells at different temperatures, *Applied Energy* 154 (2015) 160–172. <https://doi.org/10.1016/j.apenergy.2015.04.110>.
- [306] C. Rahe, S.T. Kelly, M.N. Rad, D.U. Sauer, J. Mayer, E. Figgemeier, Nanoscale X-ray imaging of ageing in automotive lithium ion battery cells, *Journal of Power Sources* 433 (2019) 126631. <https://doi.org/10.1016/j.jpowsour.2019.05.039>.
- [307] M. Varini, J.Y. Ko, P. Svens, U. Mattinen, M. Klett, H. Ekström, G. Lindbergh, On resistance and capacity of LiNi_{1/3}Mn_{1/3}Co_{1/3}O₂ under high voltage operation, *Journal of Energy Storage* 31 (2020) 101616. <https://doi.org/10.1016/j.est.2020.101616>.
- [308] R. Jung, P. Strobl, F. Maglia, C. Stinner, H.A. Gasteiger, Temperature Dependence of Oxygen Release from LiNi_{0.6}Mn_{0.2}Co_{0.2}O₂ (NMC622) Cathode Materials for Li-Ion Batteries, *J. Electrochem. Soc.* 165 (2018) 2869–2879. <https://doi.org/10.1149/2.1261811jes>.
- [309] M. Storch, J.P. Fath, J. Sieg, D. Vrankovic, A. Mullaliu, C. Krupp, B. Spier, S. Passerini, R. Riedel, Cycle parameter dependent degradation analysis in automotive lithium-ion cells, *Journal of Power Sources* 506 (2021) 230227. <https://doi.org/10.1016/j.jpowsour.2021.230227>.
- [310] M.J. Mühlbauer, D. Petz, V. Baran, O. Dolotko, M. Hofmann, R. Kostecki, A. Senyshyn, Inhomogeneous distribution of lithium and electrolyte in aged Li-ion cylindrical cells, *Journal of Power Sources* 475 (2020) 228690. <https://doi.org/10.1016/j.jpowsour.2020.228690>.
- [311] S. Solchenbach, C. Tacconis, A. Gomez Martin, V. Peters, L. Wallisch, A. Stanke, J. Hofer, D. Renz, B. Lewerich, G. Bauer, M. Wichmann, D. Goldbach, A. Adam, M. Spielbauer, P. Lamp, J. Wandt, Electrolyte motion induced salt inhomogeneity – a novel aging mechanism in large-format lithium-ion cells, *Energy Environ. Sci.* 17 (2024) 7294–7317. <https://doi.org/10.1039/D4EE03211J>.
- [312] T. Bond, R. Gauthier, G. King, R. Dressler, J.J. Abraham, J.R. Dahn, The Complex and Spatially Heterogeneous Nature of Degradation in Heavily Cycled Li-ion Cells, *J. Electrochem. Soc.* 171 (2024) 110514. <https://doi.org/10.1149/1945-7111/ad88a8>.

- [313] J. Sieg, A.U. Schmid, L. Rau, A. Gesterkamp, M. Storch, B. Spier, K.P. Birke, D.U. Sauer, Fast-charging capability of lithium-ion cells: Influence of electrode aging and electrolyte consumption, *Applied Energy* 305 (2022) 117747. <https://doi.org/10.1016/j.apenergy.2021.117747>.
- [314] J. Becherer, D. Kramer, R. Mönig, The growth mechanism of lithium dendrites and its coupling to mechanical stress, *J. Mater. Chem. A* 10 (2022) 5530–5539. <https://doi.org/10.1039/D1TA10920K>.
- [315] B.P. Matadi, S. Geniès, A. Delaille, T. Waldmann, M. Kasper, M. Wohlfahrt-Mehrens, F. Aguesse, E. Bekaert, I. Jiménez-Gordon, L. Daniel, X. Fleury, M. Bardet, J.-F. Martin, Y. Bultel, Effects of Biphenyl Polymerization on Lithium Deposition in Commercial Graphite/NMC Lithium-Ion Pouch-Cells during Calendar Aging at High Temperature, *J. Electrochem. Soc.* 164 (2017) 1089–1097. <https://doi.org/10.1149/2.0631706jes>.
- [316] S. Paarmann, M. Schreiber, A. Chahbaz, F. Hildenbrand, G. Stahl, M. Rogge, P. Dechent, O. Queisser, S.D. Frankl, P. Morales Torricos, Y. Lu, N.I. Nikolov, M. Kateri, D.U. Sauer, M.A. Danzer, T. Wetzel, C. Endisch, M. Lienkamp, A. Jossen, M. Lewerenz, Short-Term Tests, Long-Term Predictions – Accelerating Ageing Characterisation of Lithium-Ion Batteries, *Batteries & Supercaps* 7 (2024) e202300594. <https://doi.org/10.1002/batt.202300594>.
- [317] M. Steinhauer, S. Risse, N. Wagner, K.A. Friedrich, Investigation of the Solid Electrolyte Interphase Formation at Graphite Anodes in Lithium-Ion Batteries with Electrochemical Impedance Spectroscopy, *Electrochimica Acta* 228 (2017) 652–658. <https://doi.org/10.1016/j.electacta.2017.01.128>.
- [318] K. Xu, A. Cresce, U. Lee, Differentiating contributions to “ion transfer” barrier from interphasial resistance and Li⁺ desolvation at electrolyte/graphite interface, *Langmuir* 26 (2010) 11538–43. <https://doi.org/10.1021/la1009994>.
- [319] D. Zhang, B.S. Haran, A. Durairajan, R.E. White, Y. Podrazhansky, B.N. Popov, Studies on capacity fade of lithium-ion batteries, *Journal of Power Sources* 91 (2000) 122–129. [https://doi.org/10.1016/S0378-7753\(00\)00469-9](https://doi.org/10.1016/S0378-7753(00)00469-9).
- [320] M. Lewerenz, C. Rahe, G. Fuchs, C. Endisch, D.U. Sauer, Evaluation of shallow cycling on two types of uncompressed automotive Li(Ni_{1/3}Mn_{1/3}Co_{1/3})O₂-Graphite pouch cells, *Journal of Energy*

- Storage 30 (2020) 101529.
<https://doi.org/10.1016/j.est.2020.101529>.
- [321] J.C. Burns, D.A. Stevens, J.R. Dahn, In-Situ Detection of Lithium Plating Using High Precision Coulometry, *J. Electrochem. Soc.* 162 (2015) 959–964. <https://doi.org/10.1149/2.0621506jes>.
- [322] M. Schreiber, K. Abo Gamra, P. Bilfinger, O. Teichert, J. Schneider, T. Kröger, N. Wassiliadis, M. Ank, M. Rogge, J. Schöberl, P. Rosner, C. Grosu, A. Jossen, M. Lienkamp, Understanding lithium-ion battery degradation in vehicle applications: Insights from realistic and accelerated aging tests using Volkswagen ID.3 pouch cells, *Journal of Energy Storage* 112 (2025) 115357.
<https://doi.org/10.1016/j.est.2025.115357>.
- [323] E. Laakso, S. Efimova, M. Colalongo, P. Kauranen, K. Lahtinen, E. Napolitano, V. Ruiz, J. Moškon, M. Gaberšček, J. Park, S. Seitz, T. Kallio, Aging mechanisms of NMC811/Si-Graphite Li-ion batteries, *Journal of Power Sources* 599 (2024) 234159.
<https://doi.org/10.1016/j.jpowsour.2024.234159>.
- [324] M. Flügel, M. Bolsinger, M. Marinaro, V. Knoblauch, M. Hölzle, M. Wohlfahrt-Mehrens, T. Waldmann, Onset Shift of Li Plating on Si/Graphite Anodes with Increasing Si Content, *J. Electrochem. Soc.* 170 (2023) 060536. <https://doi.org/10.1149/1945-7111/acdda3>.
- [325] N. Kirkaldy, M.A. Samieian, G.J. Offer, M. Marinescu, Y. Patel, Lithium-ion battery degradation: Comprehensive cycle ageing data and analysis for commercial 21700 cells, *Journal of Power Sources* 603 (2024) 234185.
<https://doi.org/10.1016/j.jpowsour.2024.234185>.
- [326] M.P. Bonkile, Y. Jiang, N. Kirkaldy, V. Sulzer, R. Timms, H. Wang, G. Offer, B. Wu, Coupled electrochemical-thermal-mechanical stress modelling in composite silicon/graphite lithium-ion battery electrodes, *Journal of Energy Storage* 73 (2023) 108609.
<https://doi.org/10.1016/j.est.2023.108609>.
- [327] P. Jocher, M. Steinhardt, S. Ludwig, M. Schindler, J. Martin, A. Jossen, A novel measurement technique for parallel-connected lithium-ion cells with controllable interconnection resistance, *Journal of Power Sources* 503 (2021) 230030.
<https://doi.org/10.1016/j.jpowsour.2021.230030>.

Appendix

Cyclic Aging Studies

Table 1.A: Temperature boundary conditions of cyclic aging tests homogeneously aged “Enertech”. [2]

Cell name	$\vartheta / ^\circ\text{C}$
$4\text{ }^\circ\text{C } a$	3.6
$4\text{ }^\circ\text{C } b$	4.5
$19\text{ }^\circ\text{C } a$	19.0
$25\text{ }^\circ\text{C } a$	25.5
$25\text{ }^\circ\text{C } b$	25.6
$40\text{ }^\circ\text{C } a$	40.5
$45\text{ }^\circ\text{C } a$	45.2
$48\text{ }^\circ\text{C } a$	48.1

Table 2.A: Temperature boundary conditions of cyclic aging tests of inhomogeneously aged “Enertech” with standard deviation over cyclic aging time.[1]

Cell name	$\vartheta_{\min} / ^\circ\text{C}$	$\vartheta_{\max} / ^\circ\text{C}$	$T_{\text{EAT}} / ^\circ\text{C}$
$I_y 10^\circ\text{C } 25^\circ\text{C } a$	9.6 ± 1.0	25.1 ± 1.0	17.3
$I_z 10^\circ\text{C } 25^\circ\text{C } a$	10.4 ± 0.6	25.9 ± 0.6	18.2
$I_y 10^\circ\text{C } 40^\circ\text{C } a$	11.2 ± 0.3	40.8 ± 1.2	26.0
$I_y 10^\circ\text{C } 40^\circ\text{C } b$	10.6 ± 0.3	40.5 ± 0.7	25.6
$I_z 10^\circ\text{C } 40^\circ\text{C } a$	11.4 ± 0.3	39.1 ± 0.9	25.3
$I_z 10^\circ\text{C } 40^\circ\text{C } b$	10.5 ± 0.3	40.5 ± 1.2	25.5
$I_y 30^\circ\text{C } 50^\circ\text{C } a$	31.0 ± 0.5	50.0 ± 0.3	40.4
$I_y 30^\circ\text{C } 50^\circ\text{C } b$	30.5 ± 0.3	51.4 ± 0.3	41.0
$I_z 30^\circ\text{C } 50^\circ\text{C } a$	32.2 ± 1.1	50.8 ± 0.4	41.5
$I_z 30^\circ\text{C } 50^\circ\text{C } b$	31.6 ± 1.3	50.0 ± 1.7	40.8

Table 3.A: Temperature boundary conditions with standard deviation over cycling time of aging tests of homogeneous, inhomogeneously steady-state I_y and I_z aged “Enertech” for reduced DoD of 70 % for Figure 4.9.

Cell name	$\vartheta_{\min} / ^\circ\text{C}$	$\vartheta_{\max} / ^\circ\text{C}$	$T_{\text{EAT}} / ^\circ\text{C}$
25 °C a (DoD)	25.2 ± 0.2		25.2
$I_y 10^\circ\text{C } 40^\circ\text{C } a$ (DoD)	11.0 ± 1.3	36.5 ± 4.6	23.8

Table 4.A: Temperature boundary conditions of cyclic aging tests of “L 3.4”. [3]

Cell name	$T_{\text{EAT}} / ^\circ\text{C}$
5 °C c	6.2
25 °C b	25.2
45 °C b	45.1

Table 5.A: Temperature boundary conditions with standard deviation over cycling time of aging tests of homogeneous, inhomogeneously steady-state I_y aged “L 3.4” with C/2 charging C-Rate for Figure 4.18.

Cell name	$\vartheta_{\text{min}} / ^\circ\text{C}$	$\vartheta_{\text{max}} / ^\circ\text{C}$	$T_{\text{EAT}} / ^\circ\text{C}$
25 °C a (C/2_{ch})	25.2 ± 0.1		25.2
25 °C b (C/2_{ch})	25.2 ± 0.1		25.2
I_z 10 °C 40 °C a (C/2_{ch})	11.3 ± 1.7	40.7 ± 0.6	11.3 ± 1.7
I_z 10 °C 40 °C b (C/2_{ch})	11.6 ± 1.6	40.4 ± 0.6	11.6 ± 1.6

Table 6.A: Temperature boundary conditions with standard deviation over cycling time of aging tests of homogeneous, inhomogeneously steady-state I_y aged “L 3.4” with C/5 charging C-Rate for Figure 4.20.

Cell name	$\vartheta_{\min} / ^\circ\text{C}$	$\vartheta_{\max} / ^\circ\text{C}$	$T_{\text{EAT}} / ^\circ\text{C}$
25 °C a (C/5_{ch})	25.4 ± 0.8		25.4
25 °C b (C/5_{ch})	25.0 ± 0.1		25.0
I_z 15 °C 35 °C a (C/5_{ch})	14.5 ± 0.1	36.7 ± 0.1	26.6
I_z 15 °C 35 °C b (C/5_{ch})	14.5 ± 0.1	36.7 ± 0.1	25.6

Table 7.A: Temperature boundary conditions with standard deviation over cycling time of aging tests of homogeneous, inhomogeneously steady-state I_y aged “L 1” for Figure 4.22.

Cell name	$\vartheta_{\min} / ^\circ\text{C}$	$\vartheta_{\max} / ^\circ\text{C}$	$T_{\text{EAT}} / ^\circ\text{C}$
15 °C a	15.5 ± 0.1		15.5
15 °C b	15.4 ± 0.1		15.4
25 °C a	25.1 ± 0.8		25.1
25 °C b	25.0 ± 0.1		25.0
45 °C a	45.0 ± 0.1		45.0
45 °C b	45.0 ± 0.1		45.0
45 °C c	44.9 ± 0.1		44.9
I_z 20 °C 40 °C a	unkown	39.1 ± 0.1	unkown
I_z 20 °C 40 °C b	21.5 ± 0.1	39.0 ± 0.1	25.6

Semi-Empirical Aging Model Parameters

Table 8.A: Fit Parameters with 95 % confidence bounds for Function (3.11) of α_{PE} α_{PE}^{-1} over T_{EAT} and EFC of "Eneritech".

<i>A</i>	-0.006832 (-0.01122, -0.00244)
<i>B</i>	0.2522 (0.2043, 0.3001)
<i>C</i>	$-3.863 \cdot 10^{-8}$ ($-1.435 \cdot 10^{-7}$, $6.624 \cdot 10^{-8}$)
<i>D</i>	0.0426 (-0.03206, 0.1173)
<i>E</i>	0.02934 (0.02317, 0.03552)
<i>F</i>	0.2349 (0.2369, 0.4122)

Table 9.A: Fit Parameters with 95 % confidence bounds for Function (3.13) of R_{RC1} R_{RC1}^{-1} over T_{EAT} and EFC of "Eneritech".

<i>A</i>	$-6.908 \cdot 10^{-12}$ ($-1.262 \cdot 10^{-11}$, $-1.2 \cdot 10^{-12}$)
<i>B</i>	-0.22 (-0.231, -0.2901)
<i>C</i>	$-0.737 \cdot 10^{-8}$ ($-2.906 \cdot 10^{-8}$, $-5.674 \cdot 10^{-9}$)
<i>D</i>	-0.009309 (-0.0141, -0.004513)
<i>E</i>	2.142 (2.053, 2.231)

Table 10.A: Fit Parameters with 95 % confidence bounds for Function (3.13) of C_{RC1} C_{RC1}^{-1} over T_{EAT} and EFC of “Enertech”.

A	$-1.456 \cdot 10^{-11}$ ($-1.226 \cdot 10^{-11}$, $4.138 \cdot 10^{-11}$)
B	-0.2315 (-0.2687 , -0.1943)
C	$2.199 \cdot 10^{-7}$ ($-1.662 \cdot 10^{-9}$, $4.414 \cdot 10^{-7}$)
D	-0.01325 (-0.01867 , -0.007826)
E	1.81 (1.676 , 1.943)

Preliminary Validation of Thermal-Electrical Model

In this chapter, the thermal-electrical model with its modeling assumptions for the aging simulations is validated. A more detailed validation and description of the thermal-electrical model will be published in the work of the developer Oliver Queisser at TVT (KIT).

The aging simulations were performed with first order thermal boundary conditions with an in-plane thermal gradient of 30 K which is much higher than the expected through-plane thermal gradient due to the heat release inside the cell. Still, this was considered in the simulation. All things considered; the most important aspect is to check the local electrical currents of the segments of the ECN with such temperature gradients for plausibility. This can be done on an experimental setup of three parallelly connected “Kokam” at different temperatures. The experimental normalized and corrected current distribution over SoC which is shown in Figure 1.A for temperatures of 10 °C, 25 °C and 40 °C of two measurements and a discharging current of C/2. The two experimental measurements were performed on different sets of cells and represent the spread of the experimental setup. Differences in the experimental setup arise from manufacturing uncertainties of the cells and slightly different connection

resistances. This original measurement data was obtained from the methodology presented by Paarmann et al.[45].

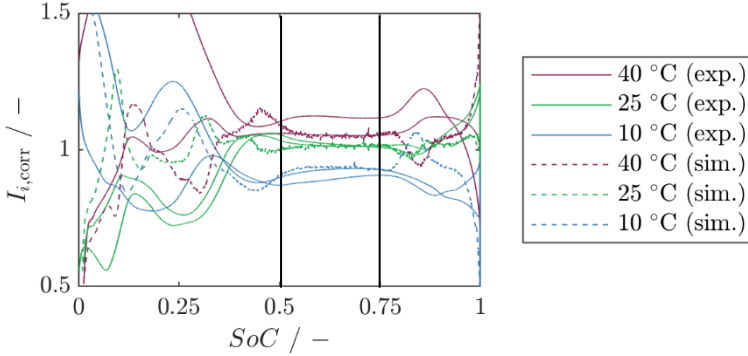


Figure 1.A: Corrected current distribution of three parallel connected “Kokam” cells (Experimental data from Paarmann et al.[30]) in comparison to model prediction for C/2 CC discharge.

A correction of a measurement according to formula (1.A) was necessary due to slight resistance differences in the parallel connection in the experimental setup. Due to this correction, a comparison can only be made in the constant region of SoC = 65 %. [45]

$$I_{i,corr} = \frac{I_i}{I_i(SoC=65\%, T_i=25\text{ }^{\circ}\text{C})} \quad (1.A)$$

The model predicts this SoC region with a high accuracy (Figure 1.A). As expected, the segment with the highest temperature is simulated to discharge with the highest electrical current for a wider SoC range in the beginning of discharging. The model also qualitatively reproduced the current swapping at lower SoCs. Especially the SoC position of current swapping onset are met. The model also predicts the current divergence close to an SoC of 0 %. There, the segment with the lowest temperature is discharged with the highest current. The current swapping is influenced by the open circuit voltage (OCV) and the internal resistance[31,32,34,35]. This

dependency can be clearly seen for the differences in current swapping of the two experimental sets. Since they were performed on two completely different sets of cells, the current swapping differs affected by the different resistances in the setup. All in all, the simulative results lie within the spread of the experiments. Better results could be obtained by increasing the quality of the experiment as suggested by Jocher et al.[327].

List of Figures

Figure 2.1: Impact of cyclic aging on different levels – Capacity loss and resistance increase, degradation modes and aging mechanisms. (Adapted with permission under the terms of Creative Commons Attribution 4.0 License CC BY.[2] Copyright 2024, The Authors. Published on behalf of The Electrochemical Society by IOP Publishing Limited.) 7

Figure 2.2: Aging mechanisms of positive and negative electrode as well as inactive materials in LIB (Reproduced with permission under the terms of Creative Commons Attribution 4.0 License CC BY.[52] Copyright 2016, The Authors. Published by Elsevier B.V.)..... 8

Figure 2.3: Exemplary ICA (left) and DVA (right) of a LIB aged at 45 °C for decreasing SoH (dark to light). (DVA adapted with permission under the terms of Creative Commons Attribution 4.0 License CC BY.[2] Copyright 2024, The Authors. Published on behalf of The Electrochemical Society by IOP Publishing Limited. 13

Figure 2.4: DVA of positive (PE) and negative (NE) electrodes matched to pouch cell and full-cell DVA at (a) BoL and (b) EoL (Adapted with permission under the terms of Creative Commons Attribution 4.0 License CC BY.[2] Copyright 2024, The Authors. Published on behalf of The Electrochemical Society by IOP Publishing Limited.) 13

Figure 2.5:	Exemplary Nyquist plot of EIS during checkup of aged cell at an aging temperature of 45 °C from “Enertech” aging study by Cloos et al.[2].....	15
Figure 2.6:	Summary of stress-factors and aging mechanisms from literature (part of figures reproduced with permission under the terms of Creative Commons Attribution 4.0 License CC BY.[2] Copyright 2024, The Authors. Published on behalf of The Electrochemical Society by IOP Publishing Limited and with permission under the terms of Creative Commons Attribution 4.0 License CC BY.[1] Copyright 2025, The Authors. Energy Technology published by Wiley-VCH GmbH.).....	28
Figure 3.1:	Overview over the methods to analyze the effect of complex thermal boundary conditions on the cyclic aging behavior of lithium-ion batteries.	31
Figure 3.2:	Schematic of (a) in-plane and (b) through-plane thermal gradient with thermal plates and thermocouples and (c) picture for an in-plane thermal gradient (Reproduced with permission under the terms of Creative Commons Attribution 4.0 License CC BY.[1] Copyright 2025, The Authors. Energy Technology published by Wiley-VCH GmbH.).	40
Figure 3.3:	Example of voltage and temperature over cycling time in minutes at the beginning of charging with superimposed temperature change from 5 °C to 45 °C (top) and 45 °C to 5 °C (bottom) (Reproduced with permission under the terms of Creative Commons Attribution 4.0 License CC BY.[3] Copyright 2023, The Authors. Batteries & Supercaps published by Wiley-VCH GmbH.).	42

Figure 3.4:	Schematic depiction of a network in y-z-plane for counter-tab pouch cells.....	47
Figure 3.5:	Schematic illustration of the interrelations of thermal (blue) and electrical (orange) model.	48
Figure 3.6:	DRT of “Enertech” from BoL (black) to aged (copper) during checkups at SoC of 50 % and 25 °C obtained from “LinKK” by IAM-ET (KIT).	50
Figure 3.7:	Development of an ECM for the electrical model as a combination of parameterization on impedance and pulse relaxation data.	51
Figure 3.8:	ECM parameters as a function of SoC and temperature with spline fits of the “Enertech”.	54
Figure 3.9:	Temperature dependency of the 18 s pulse resistance of the “Kokam” at SoC 50 % in an Arrhenius plot with linear fit.	55
Figure 3.10:	Temperature dependency of the 18 s pulse resistance of the “Enertech” at SoCs from 10 % to 100 % in an Arrhenius plot.	56
Figure 3.11:	Comparison of non-calorimetric measurement methods for the Kokam cell. Reproduction cells are indicated with dashed lines or unfilled markers. Data points for the frequency controlled and standard potentiometric method are obtained from Widanage et al.[249] (Adapted with permission under the terms of Creative Commons Attribution 4.0 License CC BY. [249] Copyright 2025, The Authors. Published on behalf of The Electrochemical Society by IOP Publishing Limited.).	57

Figure 3.12:	Evolution of SoC dependency of pulse ECM over aging of “Enertechn” aged at 19 °C (left) and 45 °C (right).	60
Figure 3.13:	Entropy coefficient of the OCV (circle) measurements during electrochemical characterization for both charging (red) and discharging direction (blue) for the “Enertech” cell. A cell at BoL (lighter color) is compared to a cell at EoL (darker color) aged at 25 °C (25 °C <i>b</i>) including a spline fit.	61
Figure 3.14:	Degradation mode analysis and capacity loss over time in days with fitted aging function for homogeneous aging temperatures from 4 °C (blue) to 48 °C (dark violett) for the cells of the “Enertech” study (Adapted with permission under the terms of Creative Commons Attribution 4.0 License CC BY.[2] Copyright 2024, The Authors. Published on behalf of The Electrochemical Society by IOP Publishing Limited.).	65
Figure 3.15:	SEM pictures of aged positive (b, c, g, h) and negative (d, e, f) electrodes of the “Enertech” in comparison to BoL (a, c) (Reproduced with permission under the terms of Creative Commons Attribution 4.0 License CC BY.[2] Copyright 2024, The Authors. Published on behalf of The Electrochemical Society by IOP Publishing Limited.).	66
Figure 3.16:	(a) Picture of the negative electrode sheets of a “Enertech” aged at 45°C and (b) light microscopy and (c, d) SEM pictures of depositions (Reproduced with permission under the terms of Creative Commons Attribution 4.0 License CC	

	BY.[298] Copyright 2024, The Authors. Published on behalf of The Electrochemical Society by IOP Publishing Limited.).....	67
Figure 3.17:	Aging modeling approach with focus on LLI and SEI growth.	69
Figure 3.18:	Evaluation of the exponent α_{pow} of a power function over a sliding window of the relative nominal capacity over time in days (Reproduced with permission under the terms of Creative Commons Attribution 4.0 License CC BY.[298] Copyright 2024, The Authors. Published on behalf of The Electrochemical Society by IOP Publishing Limited.).....	71
Figure 3.19:	Arrhenius plot of the parameters of the capacity loss aging function derived from the “Enertech” aging study[2].	73
Figure 3.20:	Empirical fit of equivalent aging temperature and EFC dependency of relative alignment parameter α_{PE} on “Enertech” aging study[2].	74
Figure 3.21:	Dependency of relative capacity and relative ohmic resistance from combined ECM on the example of high aging temperature of 45 °C and 48 °C with linear fit on “Enertech” aging study[2].	75
Figure 3.22:	Arrhenius fit of slope G representing the relation of relative capacity loss and ohmic resistance from combined ECM increase on “Enertech” aging study[2].	76
Figure 3.23:	Empirical fit of relative resistor RRQ (top) and capacitor CRQ (bottom) ($n=1$) of positive electrode charge transfer RQ element as a function of EFC on “Enertech” aging study[2].	77

Figure 3.24:	Empirical fit of relative resistance and capacitor of diffusive RC element as a function of the equivalent aging temperature and EFC on “Enertech” aging study[2].	78
Figure 3.25:	Voltage U during 2C-CC discharging (left) and charging (right) of I_y 10 °C 40 °C “Enertech” at different EFCs, experiment (exp.) from “Enertech” aging study[1] and simulation (sim.) as well as error ΔU of simulation (bottom).	80
Figure 4.1:	(a) Relative capacity loss over EFC; Quantitative change of degradation modes over EFC (b) <i>LLI</i> , (c) <i>LAMPE</i> , (d) <i>LAMNE</i> , (e) Squared norm of residuals. (Adapted with permission under the terms of Creative Commons Attribution 4.0 License CC BY.[1] Copyright 2025, The Authors. Energy Technology published by Wiley-VCH GmbH and with permission under the terms of Creative Commons Attribution 4.0 License CC BY.[2] Copyright 2024, The Authors. Published on behalf of The Electrochemical Society by IOP Publishing Limited.)	84
Figure 4.2:	Arrhenius plots of linear region of quantitative degradation modes (a) <i>LLI</i> and (b) <i>LAMPE</i> (Evaluation is based on “Enertech” aging studies[1,2]). Error bars represent 95 % CI of fitting parameter.	87
Figure 4.3:	Pictures of SEM on aged “Enertech” positive electrodes aged at lower (left) and higher (right) local aging temperatures than 25 °C; Comparison of homogeneous steady-state thermal boundary conditions (bottom) to inhomogeneous steady-state thermal boundary conditions (top) ((c, f)	

	Reproduced with permission under the terms of Creative Commons Attribution 4.0 License CC BY.[1] Copyright 2025, The Authors. Energy Technology published by Wiley-VCH GmbH.).	89
Figure 4.4:	Pictures of SEM analysis on aged “Enertech” negative electrodes aged at lower (left) and higher (right) local aging temperatures than 25 °C ((a, c) Reproduced with permission under the terms of Creative Commons Attribution 4.0 License CC BY.[1] Copyright 2025, The Authors. Energy Technology published by Wiley-VCH GmbH.).	91
Figure 4.5:	Pouch cell thickness of cell <i>Iy</i> 10 °C 40 °C <i>a</i> at the top of the “Enertech” pouch cell and close to the tabs (Reproduced with permission under the terms of Creative Commons Attribution 4.0 License CC BY.[1] Copyright 2025, The Authors. Energy Technology published by Wiley-VCH GmbH.).	92
Figure 4.6:	Pictures of negative electrode sheets of cell (a,b) <i>Iy</i> 10 °C 40 °C <i>a</i> and (c-e) <i>Iz</i> 10 °C 40 °C <i>b</i> with light microscopy pictures (b,e) (Adapted with permission under the terms of Creative Commons Attribution 4.0 License CC BY.[1] Copyright 2025, The Authors. Energy Technology published by Wiley-VCH GmbH.).	93
Figure 4.7:	Picture of negative electrode sheet of aged “Enertech” <i>Iy</i> 30 °C 50 °C <i>a</i> (Reproduced with permission under the terms of Creative Commons Attribution 4.0 License CC BY.[1] Copyright 2025, The Authors. Energy Technology published by Wiley-VCH GmbH.).	96

- Figure 4.8: Pictures of negative electrode sheets (a, c) and separators (b, f) of cell I_z 30 °C 50 °C a with light microscopy pictures (d, e) Reproduced with permission under the terms of Creative Commons Attribution 4.0 License CC BY.[1] Copyright 2025, The Authors. Energy Technology published by Wiley-VCH GmbH.) 97
- Figure 4.9: Relative capacity decrease over equivalent full cycles (EFC) for “Enertech” with a depth of discharge (DoD) of 100 % (green) (Adapted with permission under the terms of Creative Commons Attribution 4.0 License CC BY.[2] Copyright 2024, The Authors. Published on behalf of The Electrochemical Society by IOP Publishing Limited and with permission under the terms of Creative Commons Attribution 4.0 License CC BY.[1] Copyright 2025, The Authors. Energy Technology published by Wiley-VCH GmbH.) and a DoD of 70 % (black) for an equivalent aging temperature of 25 °C and homogeneous steady-state (circles) versus inhomogeneous steady-state (triangle and diamond) thermal boundary condition..... 99
- Figure 4.10: Relative nominal capacity over equivalent full cycles (EFC) comparison of experimental and simulative results (“Enertech”). Experimental data for aging at homogeneous aging temperature of 25 °C and inhomogeneous aging for I_y 10 °C 40 °C illustrated with markers (Adapted with permission under the terms of Creative Commons Attribution 4.0 License CC BY.[2] Copyright 2024, The Authors. Published on behalf of The Electrochemical Society by IOP Publishing

	Limited and with permission under the terms of Creative Commons Attribution 4.0 License CC BY.[1] Copyright 2025, The Authors. Energy Technology published by Wiley-VCH GmbH.)	
	Simulative data for inhomogeneous aging for I_y 10 °C 40 °C for all segments indicated with lines and stars in the color of the local aging temperature. Black line represents simulated cell behavior of cell I_y 10 °C 40 °C.	100
Figure 4.11:	Simulated normed current distribution I_{norm} (left) and negative electrode potential UNE (right) for three elements of an inhomogeneous temperature field I_y 10 °C 40 °C at high (red-yellow), medium (black-grey) and low (blue-green) segment temperature over aging in charging direction (simulated SoH_{min} of 79.6 %).	102
Figure 4.12:	Simulated normed current distribution I_{norm} for three elements of an inhomogeneous temperature field I_y 10 °C 40 °C at high (red-yellow), medium (black-grey) and low (blue-green) segment temperature over aging in discharging direction (simulated SoH_{min} of 79.6 %).	104
Figure 4.13:	Preliminary trends for cycling at a reduced DoD of 70 % of the “Enertech” – Simulated normed current distribution I_{norm} (left) and negative electrode potential UNE (right) for three elements of an inhomogeneous temperature field I_y 10 °C 40 °C at high (red-yellow), medium (black-grey) and low (blue-green) segment temperature over aging in charging direction. (simulated SoH_{min} of 84.4 %).	106

Figure 4.14:	(a) Relative nominal capacity loss and (b) relative 18 s pulse resistance increase at 50 % SoC over equivalent full cycles (EFC) for “L 3.4” and homogeneous steady-state as well as homogeneous transient (T) thermal boundary conditions with spotlight figures of groups A and B (Adapted with permission under the terms of Creative Commons Attribution 4.0 License CC BY.[3] Copyright 2023, The Authors. Batteries & Supercaps published by Wiley-VCH GmbH.).....	108
Figure 4.15:	Capacity difference analysis (CDA) over equivalent full cycles (EFC) for “L 3.4” and homogeneous steady-state as well as homogeneous transient (T) thermal boundary conditions with spotlight figures of groups A and B (Adapted with permission under the terms of Creative Commons Attribution 4.0 License CC BY.[3] Copyright 2023, The Authors. Batteries & Supercaps published by Wiley-VCH GmbH.).....	110
Figure 4.16:	Pictures of selected negative electrodes of homogeneous steady-state aging temperatures (top) and homogeneous transient temperatures (bottom) of “L 3.4” (Reproduced with permission under the terms of Creative Commons Attribution 4.0 License CC BY.[3] Copyright 2023, The Authors. Batteries & Supercaps published by Wiley-VCH GmbH.).....	111
Figure 4.17:	Schematic to illustrate temperature field during thermal transients (Reproduced with permission under the terms of Creative Commons Attribution 4.0 License CC BY.[3] Copyright 2023, The	

	Authors. Batteries & Supercaps published by Wiley-VCH GmbH.) 112
Figure 4.18:	Relative nominal capacity loss over EFC for homogeneous steady-state, homogeneous transient T (Reproduced with permission under the terms of Creative Commons Attribution 4.0 License CC BY.[3] Copyright 2023, The Authors. Batteries & Supercaps published by Wiley-VCH GmbH.) and inhomogeneous steady-state I_z temperature boundary conditions on “L 3.4” 114
Figure 4.19:	Picture of negative electrode sheets of “L 3.4” with the aging condition I_z 10 °C 40 °C b 116
Figure 4.20:	Relative qOCV capacity loss over EFC with reduced charging C-Rate and temperature differences for homogeneous steady-state, homogeneous transient T and inhomogeneous steady-state I_z temperature boundary conditions on “L 3.4” 118
Figure 4.21:	Relative nominal capacity loss over EFC for homogeneous steady-state, homogeneous transient T and inhomogeneous steady-state I_z temperature boundary conditions on “L 1” 119
Figure 4.22:	Pictures of negative electrode sheets of “L 1” after cycling at a homogeneous steady-state aging temperature of 15 °C (left) and homogeneous transient aging temperatures between 15 °C and 45 °C (middle and right). 121
Figure 1.A:	Corrected current distribution of three parallel connected “Kokam” cells (Experimental data from Paarmann et al.[30]) in comparison to model prediction for C/2 CC discharge. clxxiii

List of Tables

Table 3.1:	Investigated cells with nominal capacity CN, cell chemistry and investigated thermal boundary condition.	33
Table 3.2:	Electrical boundary conditions during cyclic aging (“Cycling”), checkup (“Aging”) and electrochemical characterization (“Char”) for the investigated cells.	35
Table 3.3:	Used equipment for electrochemical characterization and cyclic aging tests.	37
Table 4.1:	Linear capacity loss acceleration analysis of inhomogeneous steady-state thermal boundary conditions. [1]	86

Appendix

Table 1.A:	Temperature boundary conditions of cyclic aging tests homogeneously aged “Enertech”. [2]	clxvii
Table 2.A:	Temperature boundary conditions of cyclic aging tests of inhomogeneously aged “Enertech” with standard deviation over cyclic aging time. [1]	clxviii
Table 3.A:	Temperature boundary conditions with standard deviation over cycling time of aging tests of homogeneous, inhomogeneously steady-state I_y and I_z aged “Enertech” for reduced DoD of 70 % for Figure 4.9.	clxviii
Table 4.A:	Temperature boundary conditions of cyclic aging tests of “L 3.4”. [3]	clxix
Table 5.A:	Temperature boundary conditions with standard deviation over cycling time of aging tests of	

	homogeneous, inhomogeneously steady-state I_y aged “L 3.4” with C/2 charging C-Rate for Figure 4.18.	clxix
Table 6.A:	Temperature boundary conditions with standard deviation over cycling time of aging tests of homogeneous, inhomogeneously steady-state I_y aged “L 3.4” with C/5 charging C-Rate for Figure 4.20.	clxx
Table 7.A:	Temperature boundary conditions with standard deviation over cycling time of aging tests of homogeneous, inhomogeneously steady-state I_y aged “L 1” for Figure 4.22.	clxx
Table 8.A:	Fit Parameters with 95 % confidence bounds for Function (3.11) of α_{PE} $\alpha_{PE} - 1$ over $TEAT$ and EFC of “Enertech”	clxxi
Table 9.A:	Fit Parameters with 95 % confidence bounds for Function (3.13) of $RRC1$ $RRC1 - 1$ over $TEAT$ and EFC of “Enertech”	clxxi
Table 10.A:	Fit Parameters with 95 % confidence bounds for Function (3.13) of $CRC1$ $CRC1 - 1$ over $TEAT$ and EFC of “Enertech”	clxxii